AD-A078 441 HARVARD UNIV CAMBRIDGE MA DIV OF APPLIED SCIENCES F/G 20/3
NONEQUILIBRIUM PHENOMENA IN SUPERCONDUCTING PHASE-SLIP CENTERS.(U)
OCT 79 A M KADIN N00014-77-C-0085
UNCLASSIFIED TR-15 NL

1 OF 3
AD A078441

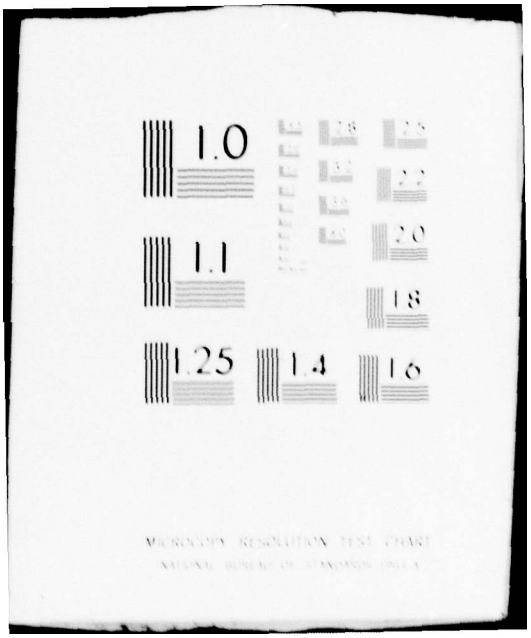
1.0
1.1
1.25
1.4
1.6
2.8
2.5
2.2
2.0
1.8
MICROCOPY RESOLUTION TEST CHART
NATIONAL BUREAU OF STANDARDS 1963-A

LEVEL II (12) 14

AD A078441

Office of Naval Research
Contract N00014 77-C-0085 NR-318-003
Contract N00014-75-C-0648
National Science Foundation Grant DMR79-04155

NONEQUILIBRIUM PHENOMENA IN SUPERCONDUCTING PHASE-SLIP CENTERS

By
Alan M. Kadin

DDC
RECEIVED
DEC 13 1979
A

October 1979

Technical Report No. 15

DDC FILE COPY

This document has been approved for public release and sale; its distribution is unlimited. Reproduction in whole or in part is permitted by the U. S. Government.

Division of Applied Sciences
Harvard University Cambridge, Massachusetts

79 12 11 002

Unclassified

SECURITY CLASSIFICATION OF THIS PAGE (When Data Entered)

REPORT DOCUMENTATION PAGE

1. REPORT NUMBER: Technical Report No. 15	2. GOVT ACCESSION NO.
4. TITLE (and Subtitle): NONEQUILIBRIUM PHENOMENA IN SUPERCONDUCTING PHASE-SLIP CENTERS	5. TYPE OF REPORT & PERIOD COVERED: Interim Report
7. AUTHOR(s): ALAN M. KADIN	8. CONTRACT OR GRANT NUMBER(s): N00014-77-C-0085, N00014-75-C-0648, NSF DMR79-04155
9. PERFORMING ORGANIZATION NAME AND ADDRESS: Division of Applied Sciences, Harvard University, Cambridge, Mass. 02138	10. PROGRAM ELEMENT, PROJECT, TASK AREA & WORK UNIT NUMBERS
11. CONTROLLING OFFICE NAME AND ADDRESS: TR-15	12. REPORT DATE: October 1979; NUMBER OF PAGES: 223
14. MONITORING AGENCY NAME & ADDRESS (if different from Controlling Office): 1226	15. SECURITY CLASS. (of this report): Unclassified; 15a. DECLASSIFICATION/DOWNGRADING SCHEDULE

16. DISTRIBUTION STATEMENT (of this Report)

Reproduction in whole or in part is permitted for any purpose of the United States Government. Approved for public release; distribution unlimited.

17. DISTRIBUTION STATEMENT (of the abstract entered in Block 20, if different from Report)

18. SUPPLEMENTARY NOTES

19. KEY WORDS (Continue on reverse side if necessary and identify by block number)

Nonequilibrium Superconductivity
Thin-Film Microbridges
Magnetic-Field Effects
Charge-Imbalance Waves
Phase-Slip Centers

20. ABSTRACT (Continue on reverse side if necessary and identify by block number)

We present the results of a study on the current-induced breakdown of superconductivity in a quasi-one-dimensional filament. We interpret this breakdown in terms of the phase-slip centers (PSC's) introduced by Skocpol, Beasley, and Tinkham (SBT), and emphasize throughout the central role played by the nonequilibrium quasiparticles. Our study consists of two parts, one largely experimental the other largely theoretical.

In our experimental work, we have invstigated the effects of a magnetic field H on nonequilibrium quasiparticle relaxation processes in superconductors by

DD FORM 1 JAN 73 1473 EDITION OF 1 NOV 65 IS OBSOLETE
S/N 0102-014-6601

Unclassified 410 457
SECURITY CLASSIFICATION OF THIS PAGE (When Data Entered)

SECURITY CLASSIFICATION OF THIS PAGE(When Data Entered)

20. Abstract continued

analyzing the I-V characteristics of long tin microbridges in a parallel field near $T_c(H)$. Following SBT, we take the differential resistance of a given PSC to be approximately equal to the normal resistance R_n of a nonequilibrium region of the bridge with length $2\sqrt{Dt_R}$, where D is the quasiparticle diffusion constant and t_R is the transverse mode (branch imbalance) relaxation time. The magnitude and the temperature and field dependence of t_R as inferred from our data agree well with those of the transverse mode relaxation time in the presence of pair-breaking, derived by Schmid and Schön. The longitudinal mode disequilibrium is interpreted in terms of local heating proportional to IV, and the resulting distortions in the I-V characteristics are corrected for moderate amounts of heating. Most of our samples contain a deliberate weak spot with a depressed critical current I_c, which isolates a single PSC and lowers the heat dissipation ($\sim I_c^2 R_n$). The depression of I_c of the weak spot relative to that of the uniform filament is incompletely understood, but is strongly dependent on the direction and magnitude of the magnetic field.

In theoretical studies, using a generalized two-fluids picture to describe a quasi-one-dimensional superconductor near T_c (for $H=0$), we provide a heuristic derivation for a set of equations governing the temporal and spatial evolution of the charge imbalance (or branch imbalance) in the quasiparticles. We show that these equations are isomorphic to those which describe a simple electrical transmission line, so that charge imbalance waves may propagate in the superconductor in analogy with electrical signals which propagate down the transmission line. We propose as a model for a PSC in a superconducting filament a localized Josephson oscillator coupled to the transmission line. Applying standard transmission-line theory to solve the problem, we show that the Josephson oscillations in the center generate charge imbalance waves which propagate out to a frequency-dependent distance of order of the quasiparticle diffusion length $\Lambda_{Q^*} = \sqrt{Dt_{Q^*}}$ before they damp out. The time-averaged behavior of the model reduces to the earlier SBT model. A novel consequence of the model is a prediction of intrinsic hysteresis in the dc current-voltage relation. The model also provides a convenient framework for dealing with ac effects in PSC's, including resonance and synchronization in systems of closely-spaced PSC's and microbridges.

Accession For	
NTIS GRA&I	☒
DDC TAB	☐
Unannounced	☐
Justification	
By	
Distribution/	
Availability Codes	
Dist	Avail and/or special

SECURITY CLASSIFICATION OF THIS PAGE(When Data Entered)

Office of Naval Research

Contract N00014-77-C-0085 NR-318-003
Contract N00014-75-C-0648
National Science Foundation Grant DMR79-04155

NONEQUILIBRIUM PHENOMENA IN SUPERCONDUCTING PHASE-SLIP CENTERS

IS PROVIDED.

By

Alan M. Kadin

Technical Report No. 14

Reproduction in whole or in part is permitted for any purpose of the United States Government. Approved for public release; distribution unlimited.

October 1979

The research reported in this document was made possible through support extended the Division of Applied Sciences, Harvard University, by the Office of Naval Research, under Contract N00014-77-C-0085, Contract N00014-75-C-0648 and by the National Science Foundation under Grant DMR79-04155.

Division of Applied Sciences

Harvard University · Cambridge, Massachusetts

79 12 11 002

ABSTRACT

We present the results of a study on the current-induced breakdown of superconductivity in a quasi-one-dimensional filament. We interpret this breakdown in terms of the phase-slip centers (PSC's) introduced by Skocpol, Beasley, and Tinkham (SBT), and emphasize throughout the central role played by the nonequilibrium quasiparticles. Our study consists of two parts, one largely experimental, the other largely theoretical.

In our experimental work, we have investigated the effects of a magnetic field H on nonequilibrium quasiparticle relaxation processes in superconductors by analyzing the I-V characteristics of long tin microbridges in a parallel field near $T_c(H)$. Following SBT, we take the differential resistance of a given PSC to be approximately equal to the normal resistance R_n of a nonequilibrium region of the bridge with length $2\sqrt{D\tau_R}$, where D is the quasiparticle diffusion constant and τ_R is the transverse mode (branch imbalance) relaxation time. The magnitude and the temperature and field dependence of τ_R as inferred from our data agree well with those of the transverse mode relaxation time in the presence of pair-breaking, derived by Schmid and Schön. The longitudinal mode disequilibrium is inter-

preted in terms of local heating proportional to IV, and the resulting distortions in the I-V characteristics are corrected for moderate amounts of heating. Most of our samples contain a deliberate weak spot with a depressed critical current I_c, which isolates a single PSC and lowers the heat dissipation ($\sim I_c^2 R_n$). The depression of I_c of the weak spot relative to that of the uniform filament is incompletely understood, but is strongly dependent on the direction and magnitude of the magnetic field.

In our theoretical studies, using a generalized two-fluid picture to describe a quasi-one-dimensional superconductor near T_c (for H=0), we provide a heuristic derivation for a set of equations governing the temporal and spatial evolution of the charge imbalance (or branch imbalance) in the quasiparticles. We show that these equations are isomorphic to those which describe a simple electrical transmission line, so that charge imbalance waves may propagate in the superconductor in analogy with electrical signals which propagate down the transmission line. We propose as a model for a PSC in a superconducting filament a localized Josephson oscillator coupled to the transmission line. Applying standard transmission-line theory to solve the problem, we show that the Josephson oscillations in the center generate charge imbalance waves which propagate out to a frequency-dependent distance of order of the quasiparticle diffusion length $\Lambda_{Q^*} = \sqrt{D\tau_{Q^*}}$ before they

damp out. The time-averaged behavior of the model reduces to the earlier SBT model. A novel consequence of the model is a prediction of intrinsic hysteresis in the dc current-voltage relation. The model also provides a convenient framework for dealing with ac effects in PSC's, including resonance and synchronization in systems of closely-spaced PSC's and microbridges.

TABLE OF CONTENTS

ABSTRACT		i
TABLE OF CONTENTS		iv
LIST OF FIGURES AND TABLE		vi
I.	INTRODUCTION AND PRELIMINARY DISCUSSION	1
II.	PHASE-SLIP CENTERS IN MAGNETIC FIELDS	21
	2.1 Introduction	21
	2.2 Samples and Experimental Procedures	25
	2.3 Behavior of the Transverse Relaxation Time τ_R	36
	2.4 Heating Effects	49
	2.5 Localized Weak Spots	72
	2.6 Conclusions	77
III.	CHARGE IMBALANCE DYNAMICS IN NONEQUILIBRIUM SUPERCONDUCTORS	79
	3.1 Introduction	79
	3.2 Derivation of Charge Imbalance Waves	80
	3.3 A Transmission-Line Equivalent for Charge Imbalance Dynamics	95
	3.4 Discussion	103

IV. A NEW MODEL FOR THE PHASE-SLIP CENTER 109

4.1 Elements of the Model 109

4.2 Waves in the Vicinity of the PSC 121

4.3 I-$\bar{V}$ Characteristics for the PSC 132

V. OTHER TOPICS 144

5.1 Detection of Charge Imbalance Waves and Interactions Between PSC's 144

5.2 Unexplained Features of Microbridges in Magnetic Fields 161

VI. SUMMARY AND CONCLUSIONS 172

APPENDIX I: ELECTRONIC TEMPERATURE REGULATION SYSTEM 181

APPENDIX II: GENERALIZED RESISTIVELY SHUNTED JUNCTION MODEL 185

APPENDIX III: FINITE LENGTH AND ARTIFICIAL TRANSMISSION LINES 193

REFERENCES 202

ACKNOWLEDGEMENTS 210

LIST OF FIGURES AND TABLE

Fig.	Title	Page
1.1	Current-voltage curve for a Sn microstrip.	3
1.2	Time-averaged potentials and currents in the SBT model of the phase-slip center.	6
1.3	Experimental configurations which yield a nonequilibrium quasiparticle potential difference.	11
1.4	Potentials near a PSC: The experiment of Dolan and Jackel.	14
1.5	I-V curves for a Sn microstrip with and without a parallel magnetic field.	17
2.1	V(I) for Sn microbridge #15A with H=1200 Oe, for a range of temperatures near $T_c(H)$.	23
2.2	Typical geometries for bridges with weak spots.	30
2.3	Schematic of electrical measuring system.	35
2.4	Relaxation time τ_R vs. reduced magnetic field.	38
2.5	Differential resistance R_n of the first PSC in Sn bridge #15A, for various constant values of $H \parallel J$, as a function of T_{bath}.	44
2.6	Same as Fig. 2.5, but for Sn bridge #29B.	45

Fig.	Title	Page
2.7	Simulated I-V curves with and without heating effects included.	57
2.8	Experimental I-V curves for Sn bridge #15A for H=0, for a range of temperatures near T_c.	60
2.9	I-V curves for bridge #15A for H=2000 Oe before and after processing to remove heating-induced distortion.	65
2.10	Heating coefficient C vs. T_{bath} for bridge #15A.	68
2.11	Experimental data for R_n^{-4} vs. T for two samples.	75
3.1	The effects of a shift in the condensate chemical potential ε_s on the condensate and on the quasiparticles.	84
3.2	Transmission-line equivalent of the charge imbalance wave equation.	97
3.3	The dispersion relation $k(\omega) = k_R + ik_I$ for the charge imbalance waves [Eq. (3.37)].	101
3.4	Use of the transmission-line equivalent to model uniform quasiparticle injection and current flow through a normal-superconducting boundary.	104
4.1	Equivalent circuits for a phase-slip center.	113
4.2	Characteristic times τ_E, τ_o, and ω_c^{-1} vs. T_c-T for Al, Sn, and Pb in the dirty limit.	117

79 12 11 002

Fig.	Title	Page
4.3	Spatial dependence of the time-averaged potentials and currents near a PSC.	120
4.4	Time dependence of the oscillations in I_n and Φ at the center of the PSC.	125
4.5	Spatial dependence of I_n and Φ .	126
4.6	Spatial dependence of the potentials μ_n and μ_s.	128
4.7	Spatial dependence of Φ using a sinusoidal supercurrent-phase relation.	129
4.8	Spatial dependence of I_n for parameters appropriate to Al at $T/T_c = 0.99$.	131
4.9	I-$\bar{V}$ curves for the PSC using τ_E/τ_o=11 and the linear current-phase relation.	133
4.10	I-$\bar{V}$ curves in the high-frequency limit, for the linear $f(\Delta\theta)$ and various values of τ_E/τ_o.	136
4.11	Same as Fig. 4.10, but with the temperature dependence reintroduced in accordance with Eq. (4.39), showing the development of hysteresis.	140
5.1	Detection of charge imbalance waves from a PSC: Proposed experimental configuration and schematic.	146
5.2	Two interacting PSC's on a uniform strip,and transmission-line equivalents.	150

Fig.	Title	Page
5.3	Lumped element equivalents for a) a long series of PSC's, and b) and c) a single PSC in a short filament.	152
5.4	$\bar{V}(I)$ and $dI/d\bar{V}(\bar{V})$ for a single PSC in a filament of length Λ.	155
5.5	Lumped-element equivalent for two interacting PSC's, using the tee section.	157
5.6	Voltage-locking function $F(\bar{V},\ell)$ vs. $\bar{V}$ for two interacting PSC's separated by a length $2\ell = \Lambda/2$.	160
5.7	Effect of magnetic field on I_c for Sn bridge #29B with weak spot.	164
5.8	I-V curves for Sn bridge #29B for H=190 Oe, showing the development of a low voltage foot.	167
5.9	I-V characteristics of short Sn bridge #35S, showing the development of possible gap structure with magnetic field.	170
A1.1	Schematic of temperature control system.	182
A2.1	Generalized resistively-shunted junction model.	186
A2.2	$\bar{V}(I)$ and $I_s(t)$ for sinusoidal $f(\Delta\theta)$.	189
A2.3	$\bar{V}(I)$ and $I_s(t)$ for linear-periodic $f(\Delta\theta)$.	190

Fig.	Title	Page
A3.1	Equivalents for finite length transmission line.	194
A3.2	Reconstruction of transmission line from pi section equivalents.	199

Table 2.1	Experimental parameters of tin microbridges.	27

CHAPTER ONE: INTRODUCTION AND PRELIMINARY DISCUSSION

The phenomenon of superconductivity was named for the remarkable ability of a metal in this state to carry a steady current with no disssipation, i.e. with no voltage to drive the current. It was recognized early on, however, that this ability will break down for some sufficiently large current. A given sample need not necessarily go directly into the classically normal-metallic state upon exceeding the critical current, however. The case of vortex flow in a type-II superconductor is one well-known example. The true hallmark of superconductivity is actually the existence of an order parameter with long-range phase coherence, rather than the infinite conductivity which gave it its name. A superconductor can go into a nonequilibrium state which retains this character while also exhibiting dissipative effects.

It is often the case that a simple geometry greatly facilitates the study of physical phenomena. A superconducting filament is one such system, which is geometrically simple, but makes for a surprisingly rich and complex problem. If the cross-sectional dimensions are small compared with the Ginzburg-Landau coherence length (which in practice may be about a micron), the filament can be treated as effectively

one-dimensional. A real version of such an idealized sample can be a thin-film microstrip or whisker crystal, with length of order 100 microns. The current-induced breakdown of superconductivity in such a sample is still not understood in its full complexity. We will deal with the problem in terms of approximations which are amenable to physical interpretation.

The resistive transition of such samples near the critical temperature T_c, as seen in the dc I-V curves, is characterized by the appearance of a series of voltage steps, each followed by a plateau of approximately constant differential resistance[1-5], as in Fig. 1.1. Each increment of differential resistance is about the same from one plateau to the next, at least for the first few steps. This basic picture has been observed in microstrips of Sn[1] (as in Fig. 1.1), Al[2], In[3], and other metals[4], and in whisker crystals of Sn and Sn alloy[5]. This constant increment of diffferential resistance suggests that what is happening is the successive onset of basically similar dissipative units as the current is increased, and that the total voltage drop along the filament is simply the sum of the voltage drops of the individual units. This was shown directly by Skocpol[1], who fabricated a microstrip with a series of side-tabs located at intervals along the length of the strip, which acted as voltage probes. The dissipative

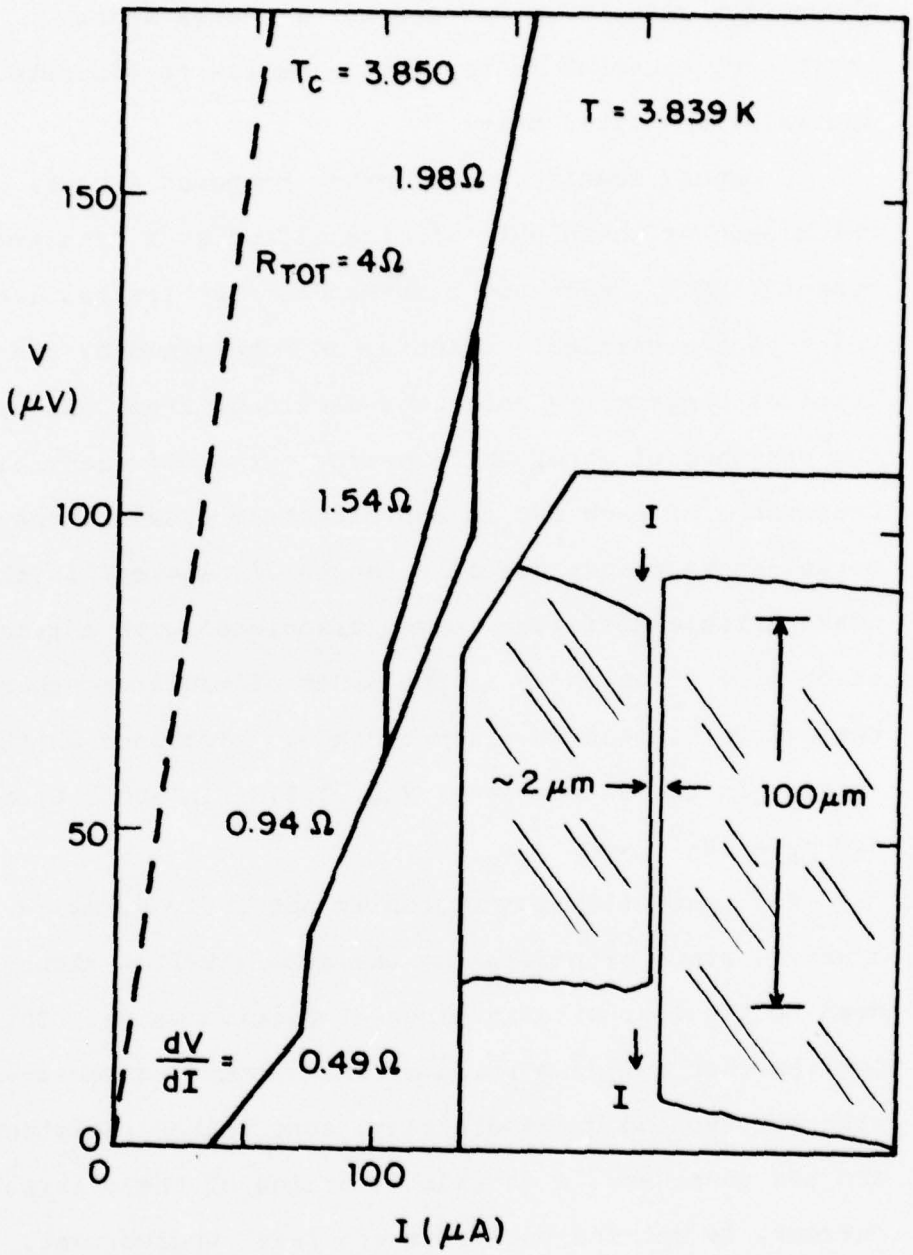

Fig 1.1 Current-voltage curve for a Sn microstrip. Note the step structure with the incremental increase in differential resistance. The inset shows the corresponding sample (tin bridge #25A in Table 2.1).

units were found to enter singly, and tended to space themselves relatively far apart. It makes sense, therefore, to speak in terms of a series of discrete spatially-localized units.

Skocpol, Beasley, and Tinkham proposed a model in which each of these units is identified as a "phase-slip center" (PSC).[1] Each PSC first appears at its own local value of the critical current, as determined by the local critical temperature and cross-sectional area, and by the presence of other PSC's nearby. The differential resistance of each PSC is approximately equal to the normal-state resistance of a length 2Λ, where Λ is the quasiparticle diffusion length associated with a relaxation time τ_R which is of the order of magnitude characteristic of inelastic electron-phonon processes in the metal. In the Sn sample of Fig. 1.1, Λ is about 6 μm and $\tau_R \approx 10^{-9}$ sec.

The nonequilibrium region is not fully normal, however, since extrapolating the straight-line slope down to the current axis gives a positive value. This implies that only a portion of the current, associated with the excited quasiparticles, contributes resistance, and the remainder, a constant fraction of the critical current, is carried as dissipationless supercurrent. In effect, we are dealing here with a generalized two-fluid picture.

These two "fluids" respond to two different electrochemical potentials, μ_n for the effectively "normal" quasiparticles and μ_s for the superconducting pairs. These two are equal in equilibrium far from the center of the dissipative region, but show fundamentally different behavior in the nonequilibrium region near a PSC. As indicated in Fig. 1.2a, a voltage drop across the PSC must appear as a change in both of these potentials, but the change occurs over two different length scales. A gradient in μ_s produces an acceleration of the supercurrent I_s and leads to a relaxation oscillation (or phase-slip cycle) of the order parameter within a region about the size of the Ginzburg-Landau coherence length $\xi(T)$. The time-averaged potential $\bar{\mu}_s$ changes abruptly within this region and is constant outside. The phase-slip process causes the time-averaged supercurrent $\bar{I}_s$ at the core region to be depressed below the value far away (see Fig. 1.2b), so that if the total current is to remain constant, the dissipative normal current $\bar{I}_n$, which is driven by gradients in the "normal" electrochemical potential $\bar{\mu}_n$, must make up the difference. This interconversion between normal current and supercurrent must occur over a scale of the quasiparticle diffusion length Λ (which is typically larger than ξ), the length required for the nonequilibrium quasiparticles carrying the normal current to come back into equilibrium with the pair condensate.

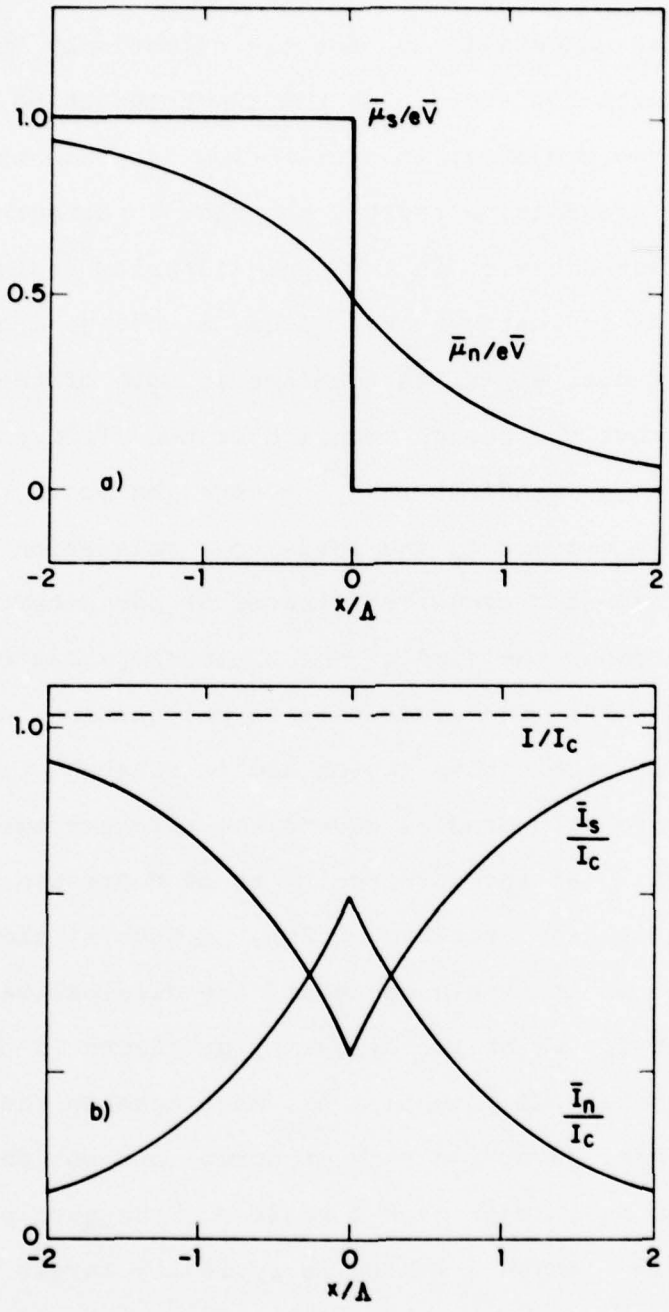

Fig. 1.2 Time-averaged potentials (a) and currents (b) in the SBT model of the phase-slip center.

In the limit where $\Lambda >> \xi$, which is what we are considering in Fig. 1.2, the details of the superconducting dynamics in the core region, which produce the actual phase-slip process itself, are not crucial to the model, and we will for the most part ignore them. However, the fact that there <u>are</u> high-frequency Josephson oscillations in the core <u>is</u> important in determining the time-dependent behavior of the currents and potentials in the larger region outside the core, and in later chapters a more detailed model will be developed which brings this time-dependent behavior into account.

In order to place the SBT picture of the PSC in perspective, we will briefly survey the field of non-equilibrium superconductivity.[6] A superconductor may be described as consisting of three interacting systems: the superconducting condensate, the quasiparticle excitations, and the phonons. The condensate, which can carry a dissipationless supercurrent, can be characterized by a complex order parameter, whose magnitude in a BCS superconductor is proportional to the gap Δ in the excitation spectrum. Quasiparticles with high energy compared to the energy gap Δ can be regarded as either electrons or holes, but low energy quasiparticles have a mixed character, although the excitation spectrum is customarily divided into an electron-like and a hole-like branch according to the predominant character of the

excitations. In thermal equilibrium, brought about by inelastic collisions between the quasiparticles and the phonons, the energy distribution of the quasiparticles is given equally on both branches by the usual Fermi function, so that there is no net charge in the quasiparticles. An external perturbation which drives the system away from equilibrium may alter the distributions of both the quasiparticles and the phonons. As far as the quasiparticles are concerned, there are two general types of perturbations, as discussed below.

An "uncharged" perturbation such as the absorption of photons or phonons may alter the number and energy distribution of the quasiparticles, producing similar effects on the distributions of both electron-like and hole-like excitations. This will alter the magnitude of the energy gap Δ in the excitation spectrum in accordance with the BCS self-consistent gap equation, and relaxation will occur by electron-phonon processes involving scattering and recombination of the quasiparticles. Such a perturbation may, of course, depress the gap, producing an effective rise in the electronic temperature. If the perturbation acts to redistribute quasiparticles away from the gap edge, however, the opposite effect, namely gap enhancement, can occur.[7] Furthermore, certain strongly nonequilibrium distributions of quasiparticles can correspond to multiple solutions of the

gap equation, permitting the possibility of an inhomogeneous state consisting of regions with differing energy gaps.[8]

In contrast, a "charged" perturbation, such as the tunneling injection of quasiparticles or the interconversion of normal and supercurrent, may involve the preferential buildup of quasiparticles on either the electron-like or the hole-like branch of the excitation spectrum[9]. Since this "branch imbalance" also corresponds to a net excess charge in the quasiparticles, the term "charge imbalance" has also been used. The pair condensate will respond to maintain electrical neutrality, causing a shift in the chemical potential of the condensate.[10] A region with nonzero charge imbalance in the quasiparticles will therefore have a difference of electrochemical potentials between the condensate and the quasiparticles, which is observable using superconducting and normal voltage probes in such a nonequilibrium region.[11]

These same two classes of perturbations have been treated from an alternative theoretical viewpoint by Schmid and Schön.[12] They showed that any small deviation from equilibrium can be resolved into two characteristic modes, which under certain circumstances can be dealt with essentially independently. Considering the complex superconducting order parameter as a vector in the

complex plane, the "longitudinal" and "transverse" modes correspond respectively to changes along the direction of this vector and perpendicular to it. The former is associated with uncharged perturbations which change the magnitude of the gap, while the latter is associated with nonequilibrium values of the order parameter phase, and hence with nonequilibrium potentials and currents involved with charged perturbations.

We will be discussing mostly problems involving transverse disequilibria, although with the understanding that in practice a certain amount of associated longitudinal mode disequilibrium (which can often be approximated as simple heating) is unavoidable because of dissipative effects. The conceptually most direct experiment in this area is the double tunnel junction injection experiment (see Fig. 1.3a) originally performed by Clarke,[13] in which a quasiparticle current is injected into the middle (superconducting) film of the sandwich through one junction, and the electrochemical potential of the quasiparticles in the middle film is probed by the normal-metal electrode of the other junction. A potential difference can be observed between the superconducting lead to the middle film and the normal-metal electrode. The injection is spatially uniform within the nonequilibrium region, and the steady-state

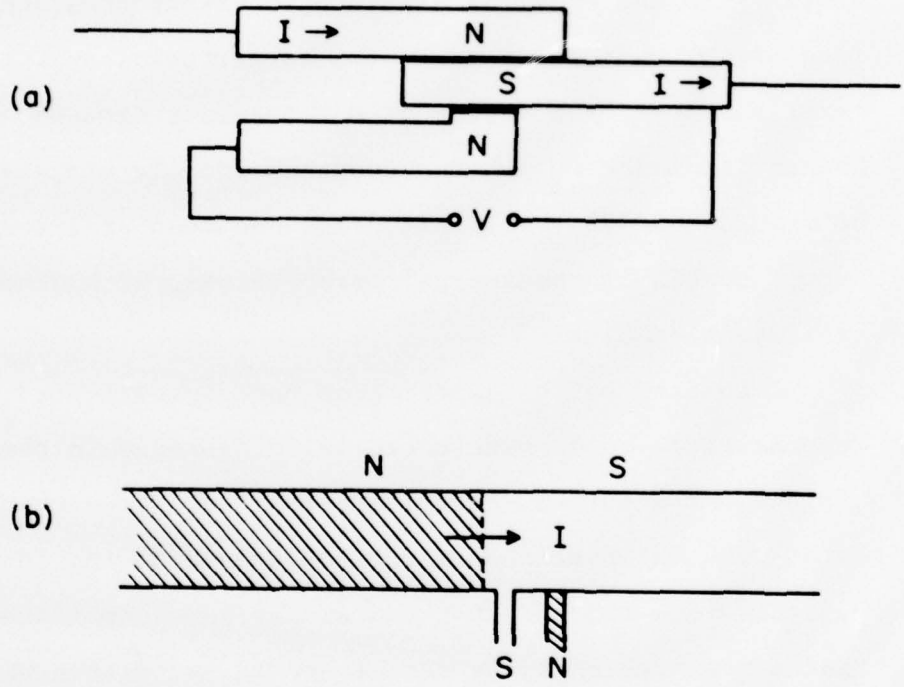

Fig. 1.3 Experimental configurations which yield a nonequilibrium quasiparticle potential difference. a) Double tunnel-junction experiment of Clarke. b) Normal and superconducting microprobes near a current-carrying N/S boundary, as by Yu and Mercereau.

potential difference is proportional to the injection current and the charge imbalance relaxation time.[9] The measured relaxation time is consistent near T_c with the expression[12]

$$\tau_{Q^*} = \frac{4k_B T}{\pi \Delta} \tau_E \qquad (1.1)$$

where τ_E is the equilibrium-averaged electron-phonon (inelastic) scattering time of quasiparticles near the Fermi surface. The factor of $k_B T/\Delta$ arises because branch imbalance relaxation occurs primarily via states between Δ and $\approx 2\Delta$. This situation has been analyzed from a number of theoretical perspectives, with generally consistent results.[14]

A related set of experiments have investigated the quasiparticle-condensate potential difference in the vicinity of a current-carrying normal-superconducting boundary. Observations of the resistance of the intermediate state and of S/N/S sandwiches have demonstrated that a measurable excess resistance is associated with the superconducting side of such a boundary.[15] Observations by Yu and Mercereau[16] with superconducting and normal probes placed within a few microns of such a boundary in a thin-film configuration (see Fig. 1.3b) confirmed the existence of a potential difference between the quasiparticles and the condensate. The results were consistent with a spatially uniform condensate

electrochemical potential μ_s (measured by the superconducting probe) and an exponential relaxation of the quasiparticle electrochemical potential μ_n (measured by the normal probe) to the condensate value with a characteristic length scale much longer than the GL coherence length. Subsequent theoretical analyses[10,17] have concluded that this exponential spatial variation of the quasiparticle-condensate potential difference should be governed by the quasiparticle diffusion length $\Lambda_{Q^*}=\sqrt{D\tau_{Q^*}}$, where $D=v_F\ell/3$ is the normal-state diffusion constant. The additional resistance contribution from the superconducting side of the S/N boundary is thus essentially the normal resistance of a length Λ_{Q^*} of the material on that side, although the situation is complicated somewhat by the spatial dependence of Λ on the scale of the coherence length near the S/N interface.[17,18]

A similar situation should prevail in the phase-slip center, and recent experiments by Dolan and Jackel[19] have provided rather direct evidence for the SBT model. Samples were fabricated which included arrays of very small voltage probes, closely spaced along the length of a thin-film microstrip (see Fig. 1.4a). Both superconducting and normal probes were used, which made it possible to make independent measurements of μ_s and μ_n as a function of position along the strip. As shown in

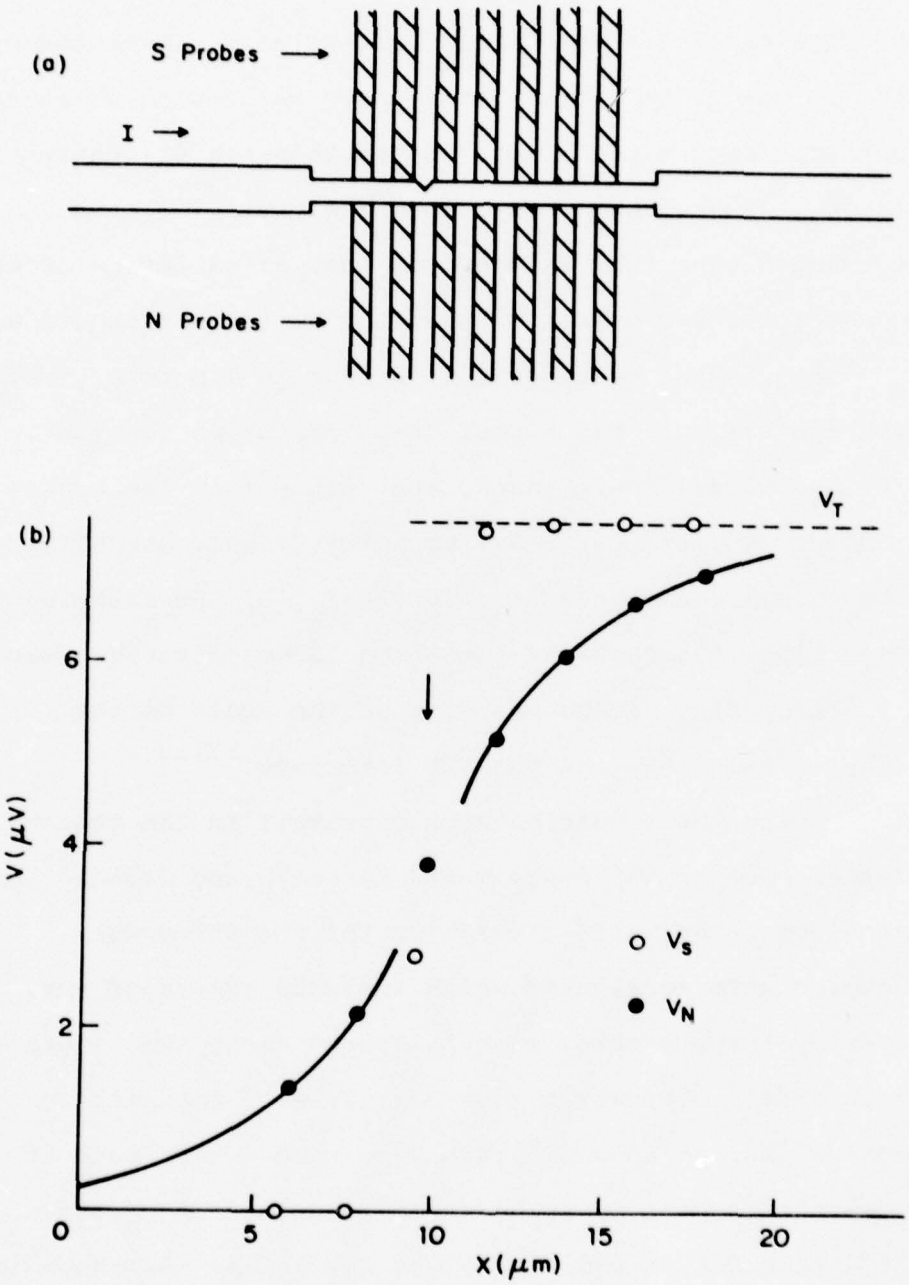

Fig. 1.4 Potentials near a PSC: The experiment of Dolan and Jackel. a) Experimental configuration, with arrays of superconducting and normal tunnel-junction microprobes. b) Spatial dependence of the measured potentials (cf. Fig. 1.2a).

Fig. 1.4b, the spatial behavior of these time-averaged potentials was found to go exactly as expected. The value of $\bar{\mu}_s$ jumped abruptly at the center of the dissipative region, while $\bar{\mu}_n$ relaxed exponentially back to the equilibrium value on each side of the center with a decay length Λ which fit the form $\Lambda=\sqrt{D\tau_{Q^*}}$.

This identifies the diffusion length Λ in the SBT model with the length Λ_{Q^*}. The weak divergence in $\Lambda_{Q^*} \propto (T_c-T)^{-\frac{1}{4}}$ as $T \to T_c$ was not apparent in many of the earlier measurements on I-V curves of PSC's, so that SBT made the initial identification of Λ with the non-divergent distance $\sqrt{D\tau_E}$. Some reasons for the non-observance of this divergence include the nonuniformity of the critical temperature, and the fact that near T_c the onset of a given PSC becomes rounded, and becomes less clearly separated from the onset of the next PSC. Furthermore, farther from T_c the power dissipated IV becomes significantly larger, producing "local heating" at the PSC, and this distorts the I-V curve by adding upward curvature to the plateau region and creating hysteresis between the zero-voltage and the dissipative branches of the curve.[1] Nevertheless, within the limited temperature range over which changes in the differential resistance of a PSC accurately reflected changes in the decay length, Dolan and Jackel did find

that this resistance corresponded to the normal resistance of the length equal to twice this quasiparticle diffusion length Λ_{Q*}.

The earlier experiments on PSC's were done in zero applied magnetic field. Like other pair-breaking interactions such as magnetic impurities and large current densities, a magnetic field parallel to a thin-film sample not only reduces the critical temperature, but also induces characteristic changes in the density of states and the excitation spectrum.[20] For large pair-breaking this leads to "gapless superconductivity", characterized by the absence of a gap in the excitation spectrum while maintaining superconducting order.

The experimental research to be discussed in Chapter Two was undertaken to determine to what extent the SBT model of the PSC remains valid in the presence of a parallel magnetic field, and what effect the field, as an example of a pair-breaking perturbation, has on the nonequilibrium processes in the superconductor.[21] As illustrated in Fig. 1.5, we find that PSC's are indeed observed for T near $T_c(H)$ (the reduced critical temperature), and that the relaxation time $\tau_R(T,H)$ inferred from the increments R_n of plateau differential resistance depends strongly on the intensity of the field. By paying special attention to the important role played by heating in producing characteristic distortions of the

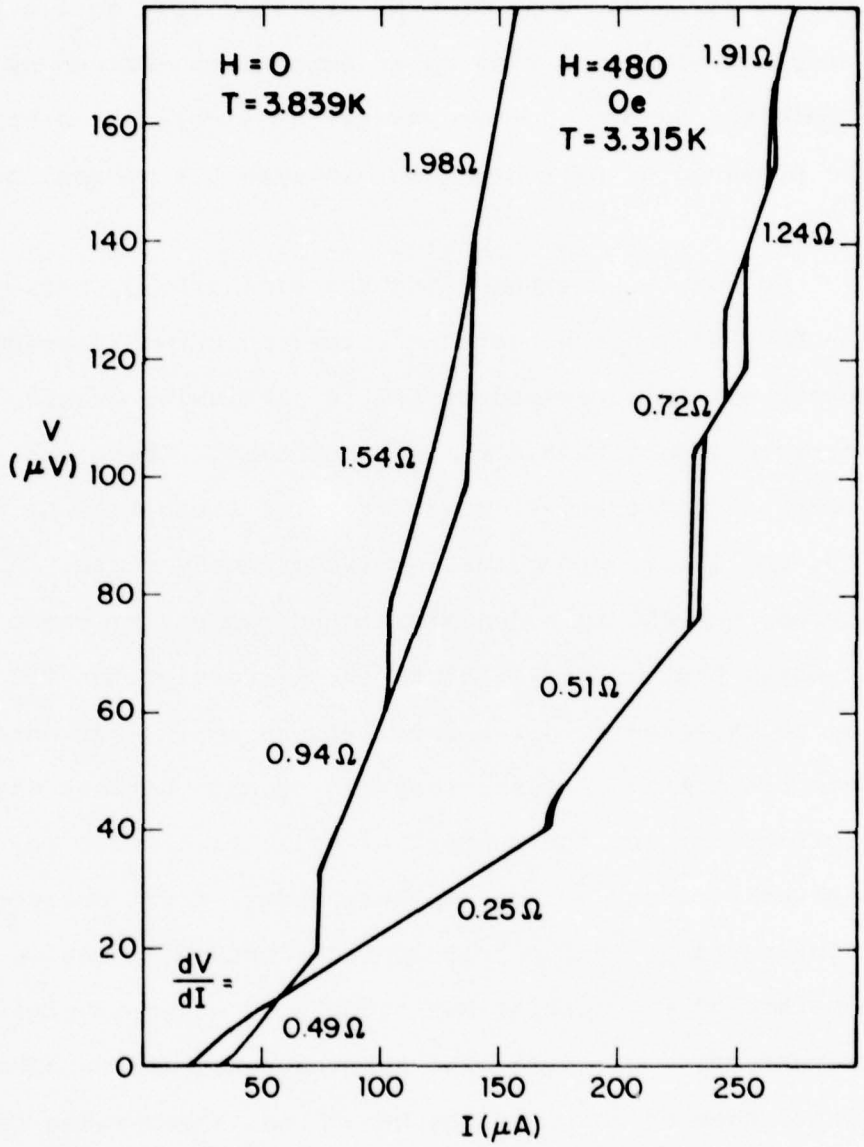

Fig. 1.5 I-V curves for a Sn microstrip (#25A in Table 2.1) with and without a parallel magnetic field.

I-V curves, we are able to minimize and partially correct for these effects. We are then able to fit the inferred relaxation time to an expression derived by Schmid and Schön[12] for transverse mode relaxation in the presence of pair-breaking, in effect a generalized τ_{Q^*}.

We have been emphasizing the similarities between the PSC and other situations involving nonequilibrium potentials in superconductors, in particular quasiparticle injection and the N/S boundary. There are important differences, however, chief among them being that the latter processes involve a steady state, whereas the PSC is a dynamic time-dependent process, in which the gap oscillations in the core of the PSC may be expected to drive oscillations in the currents and potentials. A connection can be made between these oscillations and the subject of collective modes in superconductors.[22] One of these modes, first detected experimentally in superconducting fluctuations below T_c,[23] consists of propagating but attenuated waves involving a counterflow of normal and supercurrent. As we demonstrate theoretically in Chapter Three, these waves can be derived from a generalized two-fluid picture[24] as an ac generalization of the steady-state charge imbalance effects discussed earlier. We show further that these

charge imbalance waves are analogous, for a one-dimensional superconductor near T_c, to electrical signals propagating down a simple transmission line.[25] This transmission line provides a convenient picture in which to view the whole range of experiments involving charge imbalance effects in superconductors, and we make some predictions of additional effects which have not yet been observed experimentally.

We proceed with our theoretical study in Chapter Four, with a model for the PSC in which the essential features of the SBT model are generalized to account for ac effects, and the temporal and spatial evolution of the currents and potentials can be understood in terms of charge imbalance waves driven by Josephson oscillations in the core of the PSC.[25] This can be represented as an ideal Josephson element of negligible extent (corresponding to the core) coupled to the transmission-line equivalent circuit mentioned above. We then take advantage of standard transmission-line theory to calculate a straightfoward solution to the problem. In addition to providing a consistent picture of the ac properties of PSC's, this solution also predicts the existence of intrinsic hysteresis in the dc I-V curves, quite apart from hysteresis due to heating, which we have not included in this model.

As in any active field of research, the present work does not answer all the questions or follow up on all possible leads. In Chapter Five we discuss some additional topics, which, although incomplete, may be a guide for future research. These include, on the experimental side, a more detailed discussion of some effects related to localized weak spots in magnetic fields, in particular critical currents and low-voltage behavior. On the theoretical side, we discuss some preliminary calculations concerning the application of our PSC model to the phenomena of synchronization and resonance in series of two or more PSC's.

To summarize the structure of the present report, we continue in Chapter Two with a presentation and discussion of our experimental measurements on PSC's in parallel magnetic fields. Chapter Three contains a general theoretical analysis of charge imbalance dynamics, which is used in Chapter Four to develop our model for the PSC. Some additional topics, both experimental and theoretical, are discussed in Chapter Five, and in Chapter Six we summarize our current understanding of nonequilibrium phenomena in superconducting phase-slip centers.

CHAPTER TWO: PHASE-SLIP CENTERS IN MAGNETIC FIELDS

2.1 Introduction

We present in this chapter a review of our experimental studies on long tin superconducting microbridges in the presence of parallel magnetic fields, following up on the work of Skocpol *et al.*[1,26] on such samples in zero field. Much of this work has been reported in previous works of the author.[21,11]

We show in Fig. 2.1 a set of I-V curves of a tin microstrip in a parallel magnetic field, for a set of temperatures near the reduced critical temperature $T_c(H)$. As we noted in Chapter I, the general appearance of these curves is similar to that in zero field. The voltage "step" may be somewhat rounded, but it is followed in the usual way by a region of approximately constant differential resistance. In this sample we have used a weak spot in the center of the bridge to effectively isolate the curve for a single PSC, from which we extract our data. The differential resistance of the PSC increases at high voltages, which as we will show later is due to heating. It is also larger at low voltages because of the rounded onset of the plateau region. We therefore choose the minimum value of dV/dI (the slope of the dashed lines tangent to the curves of

Fig. 2.1 V(I) for Tin microbridge #15A in a parallel field of 1200 Oe, for a range of temperatures near $T_c(H)$. Curve A - T=3.709 K; B 3.684; C 3.649; D 3.628; E 3.595; F 3.568; G 3.535; H 3.505; I 3.472; J 3.434. The slopes of the dashed lines tangent to the curves are taken as the characteristic resistance R_n of the PSC. Curve C - R_n= 0.83 Ω; D .793; E .727; F .678; G .648; H .677; I .685; J .683.

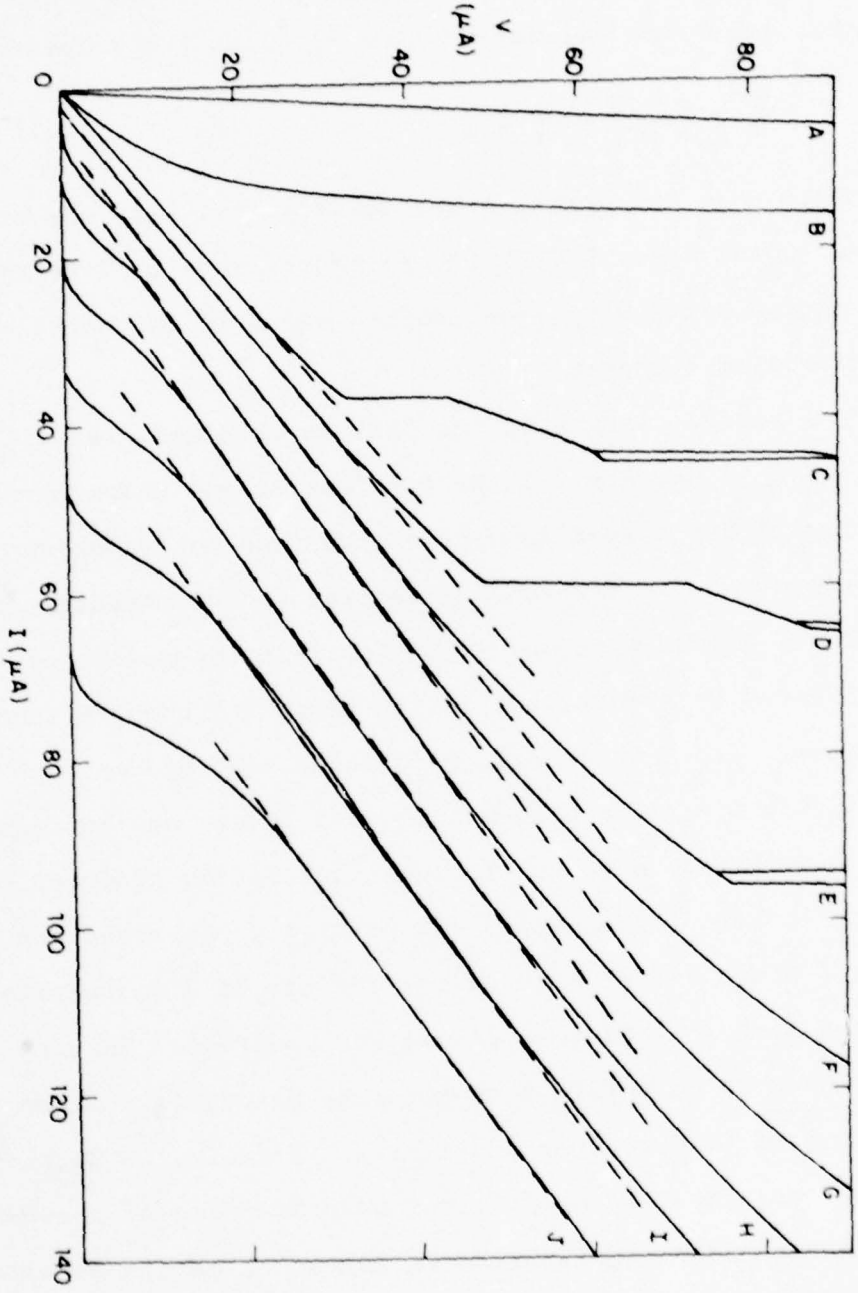

Fig. 2.1

Fig. 2.1) as the characteristic resistance R_n of the nonequilibrium region of the bridge. Following SBT, we then infer the relaxation time τ_R using the relation

$$R_n = \frac{\rho}{A}(2\Lambda) = \frac{2\rho}{A}\sqrt{D\tau_R} \qquad (2.1)$$

where ρ is the normal-state resistivity, A is the cross-sectional area, $\Lambda(T,H)$ is the experimentally inferred quasiparticle diffusion length, and D is the normal-state diffusion constant.

Before discussing the data we obtained, we will review in Section 2.2 the fabrication and characterization of our thin-film microbridges and our experimental procedure. In Section 2.3 we present our measurements of the temperature and magnetic field dependence of the inferred transverse relaxation time, and compare them to theory. In Section 2.4, we discuss heating, on both a microscopic and a phenomenological level, and explain how distortions in the I-V characteristics produced by heating can be minimized and partially corrected for. In Section 2.5 we discuss how the use of a deliberate weak spot to isolate a single PSC and reduce heating allowed us to obtain more accurate data over a wider range of temperatures and fields. Finally, in Section 2.6, we summarize our current understanding of phase-slip centers and nonequilibrium relaxation times in parallel magnetic fields.

2.2 Samples and Experimental Procedures

The procedures for sample preparation were, except where otherwise noted, very similar to those used by Skocpol[26] for his measurements on Sn microbridges in zero magnetic field, and we will only review them here. The samples were prepared on glass or crystal sapphire substrates, typically 1 × ½ in. in size, to which leads were first attatched with small patches of In or In-Sn alloy. A film of Sn was then vapor-deposited on a cold (77K) substrate in a vacuum of better than 10^{-6} torr, and the thickness (of order 1000 Å) was measured with a calibrated quartz crystal monitor to an accuracy of better than 10%. By varying the deposition rate, the purity of the tin film and hence the residual resistivity could be varied substantially. A typical rate for a reasonably clean film was 100 Å/sec. In some samples, the Sn film was applied on top of a thin undercoat of Sn which had been oxidized by a glow discharge in O_2, in order to achieve better adhesion of the film to the substrate.[27]

The critical temperature of pure bulk Sn is 3.72 K, but that of thin films is generally found to be higher. This enhanced T_c has been shown to be associated with increased electron-phonon coupling at thin-film surfaces and crystallite boundaries.[28] The values of T_c for our

samples (see Table 2.1) were typically in the range from 3.8 to 3.9 K, with those for some extremely thin samples up to 4.0 K.

With the substrate mounted on an adjustable microscope stage and a diamond knife held above, a small region of the film together with the edge of the knife were brought into focus under a microscope. The knife was carefully lowered onto the surface, and adjacent regions of the film were scraped away, leaving the long, thin rectangular microbridge connecting the two halves of the film. Dimensions ranged from 1 to 5 μm in width and from 15 to 150 μm in length. The parameters for a number of bridges are listed in Table 2.1.

In general, our samples were not quite the ideal quasi-one-dimensional filaments that our discussion might indicate. In the absence of a magnetic field, the GL coherence length takes the form[29]

$$\xi(T) = 0.85\ (\xi_o \ell)^{\frac{1}{2}}(1-T/T_c)^{-\frac{1}{2}} \qquad (2.2)$$

for a dirty superconductor near T_c, where ℓ is the mean free path and $\xi_o = \hbar v_F/\pi\Delta(0)$ is the BCS coherence length. A similar formula using the renormalized $T_c(H)$ will apply in the presence of a parallel magnetic field. (This is only valid if the transition to the normal state is second order in the presence of the field.) Choosing typical parameters ℓ = 700 Å and $T_c - T$ = 40 mK, one obtains

Table 2.1: Experimental Parameters of Tin Microbridges

Sample	L (μm)	w (μm)	d (Å)	R_T/L (Ω/μm)	ℓ (Å)	T_c (K)	$H_{c\parallel}(0)$ (Oe)	$\Lambda(0)$[a] (μm)	$\Lambda(H)$[a] (μm)	Weak Spot
3	71	1.2	1000	0.12	700	3.75[b]	820	6	0.6	none
4	48	1.0	1040	0.2	500	3.72[b]	880	5	0.5	none
10	25	2.5	1070	0.16	300	3.865	1480	2	0.45	nick
15A	50	2	500	0.5	200	3.905	4350	2	0.5	nick
25A	100	3	850	0.04	900	3.85	1150	6	3.0	nick
29B	65	5	1080	0.025	800	3.82	700	5	0.6	groove
34A	60	3	200	0.5	300	4.00	≈8000	2	-	none

a) $\Lambda(0)$ and $\Lambda(H)$ are approximate values of the quasiparticle diffusion length in zero magnetic field and in large magnetic fields respectively.

b) Measured with carbon resistance thermometer and somewhat irreproducible.

$\xi(T) \simeq 1$ μm. Although the thickness d of our samples was always much less than this, the width was often somewhat greater. This was in part because submicron-width bridges are more difficult both to fabricate and to maintain (because of burnout problems) than the wider ones. In the limit of very large width ($w>>\xi(T)$), the current-induced breakdown of superconductivity has been shown to occur via the nucleation of vortices at the edges of the film, which then move across the film.[30] It seems that the transition between narrow and wide strips is sufficiently broad that the SBT picture of a PSC still holds approximately in the range $w \sim \xi(T)$.[31]

A further assumption is that the applied field penetrates the film uniformly. This is valid if the thickness d is much smaller than the magnetic penetration depth in zero field[32]

$$\lambda(T) \simeq \lambda_L(0)\ (\xi_o/\ell)^{\frac{1}{2}}\ [1-(T/T_c)^4]^{-\frac{1}{2}} \qquad (2.3)$$

where $\lambda_L(0)$ (= 340 Å for Sn) is the London penetration depth at T=0. In the opposite limit, if $d>\sqrt{5}\ \lambda$, the film undergoes a first order phase transition at the critical field $H_{c\|}(T)$, i.e. the gap goes discontinuously to zero at the transition. All our samples are thin enough to have a second order transition, so that the parallel critical field is given by[33]

$$H_{c\|}(T) = 2\sqrt{6}\, H_{cb}(T)\, \lambda(T)/d \qquad (2.4)$$

which is always larger than the bulk critical field $H_{cb}(T)$. For tin, $H_{cb}(0) = 308$ gauss, and we have studied samples with the extrapolated $H_{c\|}(0)$ from about 700 gauss to over 4 kilogauss. In those samples where $d \ll \lambda$, the gap in the presence of the field satisfies the relation[33]

$$\frac{\Delta^2(T,H)}{\Delta^2(T)} = 1 - \frac{H^2}{H_{c\|}^2(T)} \qquad (2.5)$$

In the regime where $d \simeq \lambda$, the external magnetic field does not fully penetrate the film, and so is less effective in depressing the gap Δ. The corrections should be fairly small, however, and we will disregard them.

Some of the samples contained a single, deliberately inserted weak spot along an otherwise nominally uniform bridge. This was made in most cases by bringing down the diamond knife transverse to the bridge and cutting part-way through the thickness of the film ("nick", Fig. 2.2b). This was a rather touchy procedure, and required considerable trial and error as well as frequent trips between the low-powered microscope used for fabrication and the high-powered one (600×) used for careful sample examination. The width of one such cut was determined from a scanning electron micrograph to be about 1000 Å, far less than λ under any conditions.

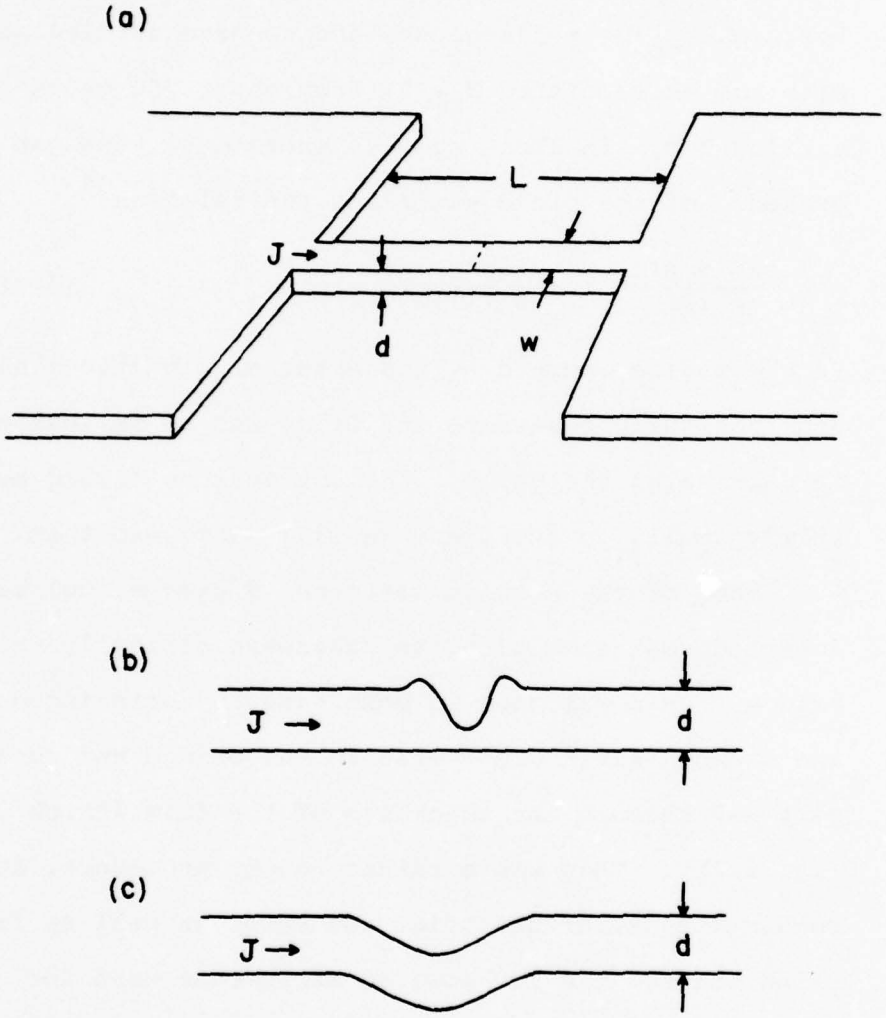

Fig. 2.2 Typical geometries for bridges with weak spots. a) Overall view. b) and c) are magnified side views of the "nick" and "groove" types of weak spots, respectively.

This type of weak spot tended to heal itself in a period of order a few weeks at room temperature. We conjecture that the mechanism for this may be thermally activated surface-self diffusion, in part because the healing of small scratches on a metal surface has actually been used to study surface self-diffusion in metals.[34] In other cases, the "weak" spot was produced by depositing the film over a groove in the substrate (width $\lesssim$ 5000 Å), and then fabricating the bridge transverse to this groove ("groove", Fig. 2.2c). The local reduction of the critical current at the groove was a product of its interaction with the external magnetic field, as will be discussed in Section 2.5, rather than a simple decrease in geometrical cross-section. The fabrication of this groove was made with the sharp pointed tip of a diamond knife, in a similar way to analogous grooves made by M. Octavio for his variable-thickness bridges.[27] This form of weak spot seemed to remain relatively stable, presumably because of the adhesion to the substrate at the lower surface.

In mounting the sample onto the cryostat, care had to be taken to prevent burnout by electrical transients, although the problem was generally not as severe as that experienced by Octavio with very small microbridges.[27]

Burnout involved melting and drawing back of the tin in the weakest region of the bridge, and was normally clearly visible under the microscope. To assist in preventing it, a conducting path parallel to the bridge was left connected until after the sample leads were soldered to the voltage and current leads on the cryostat. The soldering iron was unplugged for this operation, since otherwise inductive coupling to the heating element produced ac voltages of order 10 mV in the hot tip. After scratching away the conducting shunt, the continuity of the bridge was checked using a 1 μA source and a microammeter, rather than an ohmmeter which might cause burnout. Most burnouts tended to occur at room temperature, but transients in the electrical measuring system (e.g. due to turning equipment on or off) have also caused problems on occasion.

The sample was mounted vertically in a horizontal magnetic field, and was either directly immersed in the liquid helium bath, with pressure regulation to fix the temperature, or inside a vacuum can, with a heater and electronic temperature regulation (see Appendix 1 for the details of the temperature regulation circuit). Bath temperatures could be maintained in the range from 4.2 K down to about 1.3 K. The temperature was measured with a calibrated doped-Ge resistance thermometer to a

relative accuracy of about 1 mK. Earlier measurements taken with a carbon resistance thermometer were found to be insufficiently reproducible. The magnet, with conventional pole-pieces located outside the dewar, was feedback-stabilized with relative accuracy of about 1 gauss. Fields of up to several kilogauss were used. At this level magnetoresistance in the Ge thermometer (which goes as H^2) produced errors of at most several mK, which could be ignored. The magnet could be rotated around the dewar on a track, so that one could align the field parallel to the plane of the thin-film sample. This was accomplished to within a quarter of a degree by maximizing I_c at fixed T and large, fixed H. This maximum reflects the fact that the critical field of a film is a sharply-peaked function of angle, with a maximum for the parallel orientation and a minimum for perpendicular orientation.[35] It is only for the parallel orientation that the applied field causes the gap to be depressed continuously and uniformly to zero; a perpendicular component will cause the entry of vortices or flux bundles.

In taking the I-V curves, the sample was current-biased with a battery-powered source, and the voltage was measured with a Keithley nanovoltmeter (or at times, a PAR-113). In some cases, a PAR HR-8 lock-in amplifier

was used to measure dV/dI directly as a function of current. The curves were plotted on an X-Y recorder as the bias current was swept by hand. The schematic circuits for these situations are shown in Fig. 2.3.

In order to reduce rf interference, the leads consisted of twisted wire pairs, and a set of Erie rf filters were also used. The measurements were not, however, taken in an rf-shielded room. Mechanical stability of the magnet dewar was also important, since one source of low-frequency interference was inductive pick-up due to vibrations of the cryostat in large magnetic fields.

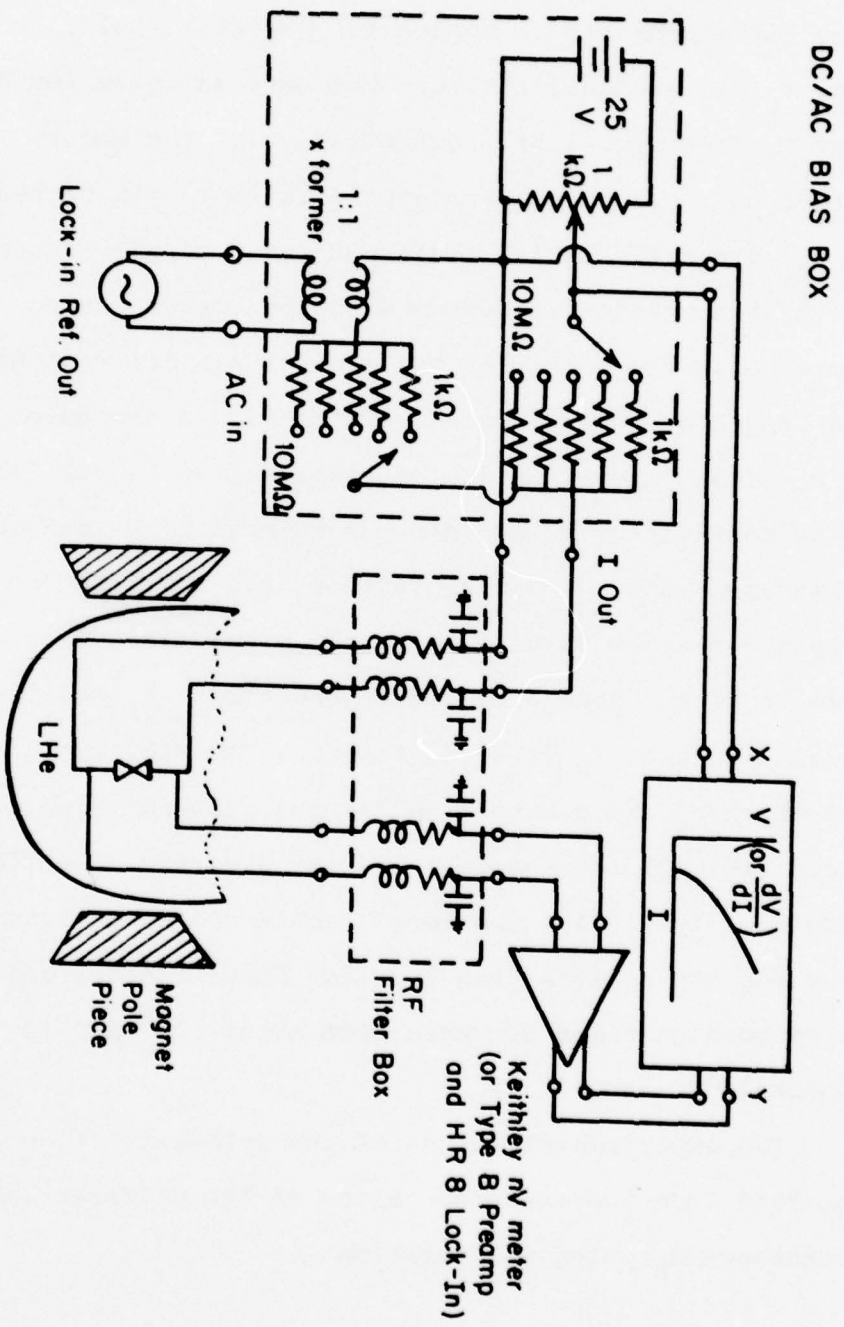

Fig. 2.3 Schematic of electrical measuring system.

2.3 Behavior of the Transverse Relaxation Time τ_R

As we have noted earlier, the I-V characteristics of a tin microstrip in a parallel magnetic field, for T near $T_c(H)$, are qualitatively the same as those for H=0 near T_c (see Fig. 1.5). Quantitatively, the major effect of increasing the magnetic field is the decrease of R_n, the differential resistance of a single PSC in the plateau region, together with the corresponding increase in the number of PSC's which can "fit" along the length of the bridge. There is also a variation of R_n with temperature for constant H (see Fig. 2.1), which consists of a weak divergence near $T_c(H)$ and an enhancement due to heating farther away. Still, one can take the minimum value of R_n for a given field H as a measure of the general field dependence of R_n and the relaxation time τ_R inferred from it. In Fig. 2.4, these values of τ_R are plotted against the reduced magnetic field $H/H_{c\|}(0)$ for the first PSC of a series of different samples. Typically, the length scale decreases from about 5 μm for H=0 to less than 1 μm for large fields, and the corresponding times decrease from about 10^{-9} sec to almost 10^{-11} sec.

The experimental values of the relaxation time were inferred from the measured values of the differential resistance R_n using the relation

Fig. 2.4 Relaxation time τ_R versus reduced magnetic field $H/H_{c\|}(0)$. Each point corresponds to the minimum value of R_n of the first PSC for T near $T_c(H)$. This shows the general magnetic field dependence of τ_R, neglecting the divergence at $T_c(H)$. The experimental points are compared with three characteristic times, which are defined as in the text with $\tau_E(T_c) = 3 \times 10^{-10}$ sec.

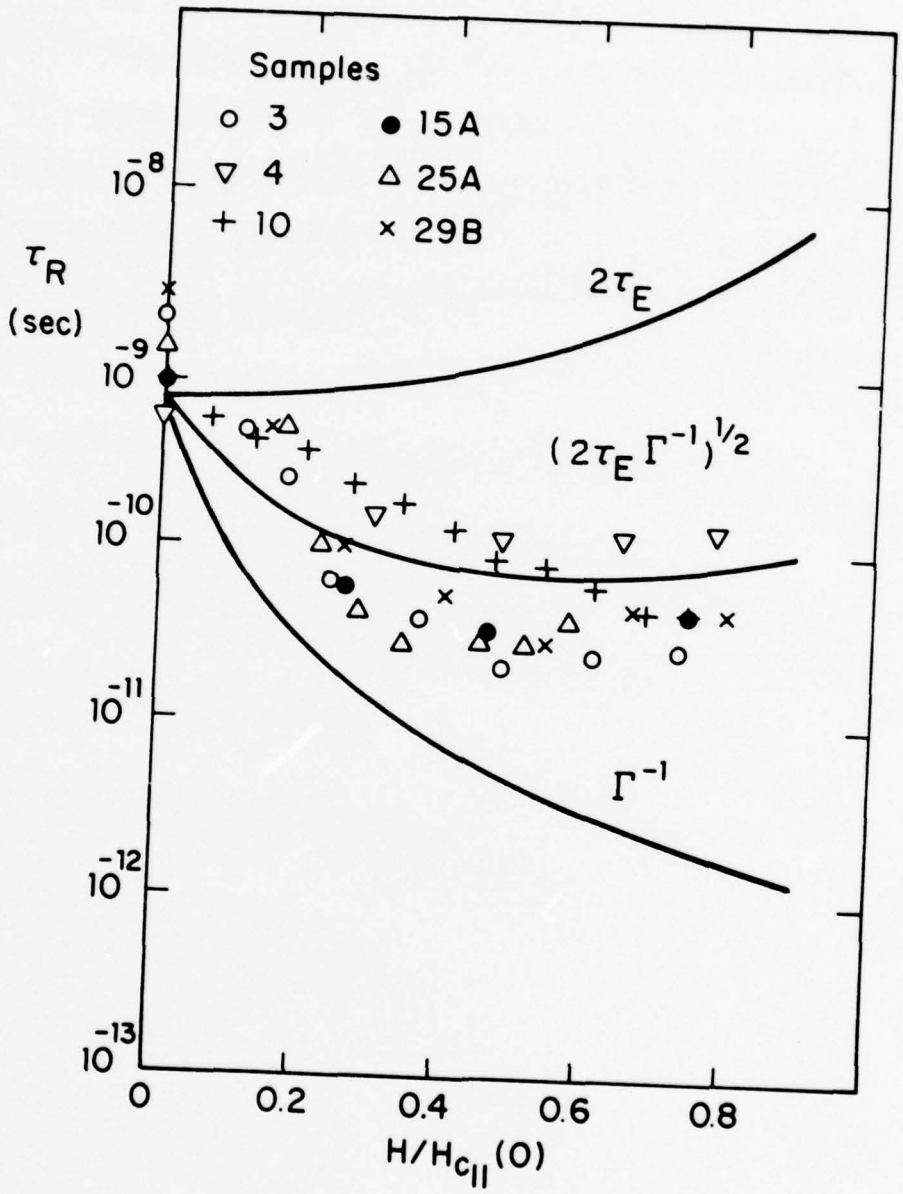
Samples
○ 3
● 15A
▽ 4
△ 25A
+ 10
× 29B
τ_R
(sec)
10^{-8}
10^{-9}
10^{-10}
10^{-11}
10^{-12}
10^{-13}
$2\tau_E$
$(2\tau_E\Gamma^{-1})^{1/2}$
Γ^{-1}
0
0.2
0.4
0.6
0.8
$H/H_{c_{11}}(0)$

Fig. 2.4

$$\tau_R = \frac{1}{D}\left(\frac{wd}{2\rho}\right)^2 R_n^2 \qquad (2.6)$$

Here d is the film thickness, w is the bridge width, and ρ is the normal-state remnant resistivity. This resistivity was determined either from the resistivity ratio of the sample between room temperature and 4.2 K or from the bridge geometry and its 4.2 K resistance. The geometry was measured from optical or scanning electron micrographs. The diffusion constant $D=v_F\ell/3$ was determined using the relation $\rho\ell = 1.0 \times 10^{-11}$ Ω-cm^2 together with the value $v_F = 0.7 \times 10^8$ cm/sec.[36] We estimate that taking into account the various uncertainties in all these measurements, the proportionality constant between τ_R and R_n^2 should be known for a given sample to within a factor of two.

In zero field, SBT made the tentative identification $\tau_R \simeq \tau_E(T_c)$, where τ_E is the electron-phonon collision time. In the absence of a comprehensive understanding of the problem, we initially expected that the effect of a magnetic field would be to replace T_c by the reduced $T_c(H)$, yielding $\tau_R \simeq \tau_E[T_c(H)]$. Since the phonons "freeze out" at low temperatures, this time gets substantially longer: $\tau_E \propto T^{-3}$. This, however, is in strong disagreement with the experimental data (see Fig. 2.4); the basic trend goes in the other direction.

There is, however, another characteristic time in the problem. A parallel magnetic field in a dirty superconductor ($\ell << \xi_o$) is one member of the class of pair-breaking perturbations, which in the limit of strong perturbation leads to gapless superconductivity.[20] The effect of any of these perturbations on the gap and the excitation spectrum can be characterized in terms of the pair-breaking energy 2α , or equivalently the pair-breaking time $\tau_s = \hbar/(2\alpha)$, which for a magnetic field parallel to a thin film take the form [20]

$$2\alpha = \frac{\hbar}{\tau_s} = \frac{1}{3}\frac{De^2H^2d^2}{\hbar} \qquad (2.7)$$

For large pair-breaking, superconductivity will be totally destroyed (i.e. the critical temperature driven to zero) when this pair-breaking energy is equal to the energy gap in the absence of pair-breaking:

$$2\alpha_c(0) = \Delta(T=0,H=0) = 1.76\ k_B T_c \qquad (2.8)$$

The zero-temperature critical field can therefore be expressed as

$$H_{c\parallel}(0) = \left(\frac{\Delta(0,0)\,3\hbar}{De^2d^2}\right)^{\frac{1}{2}} \qquad (2.9)$$

so that we can write

$$\tau_s = \frac{\hbar}{2\alpha} = \frac{\hbar}{\Delta(0,0)}\frac{H_{c\parallel}^2(0)}{H^2} \qquad (2.10)$$

For small pair-breaking, the depression of the critical temperature is linear in the pair-breaking energy,

$$T_c - T_c(H) = \frac{\pi\alpha}{4k_B} \tag{2.11}$$

so that the pair-breaking time can also be written

$$\tau_s = \frac{\pi\hbar}{8k_B[T_c - T_c(H)]} \tag{2.12}$$

[cf. the Ginzburg-Landau time $\tau_{GL} = \pi\hbar/8k_B(T_c - T)$] and the temperature dependence of the critical field takes the form

$$H_{c\parallel}(T) = 1.2\ H_{c\parallel}(0)\ (1-T/T_c)^{\frac{1}{2}} \tag{2.13}$$

Eq. (2.13) is approximately valid down to about $\frac{1}{2}T_c$.

In practice, we use Eq. (2.13) to determine $H_{c\parallel}(0)$, by fitting to the measured values of $T_c(H)$. Since we want this to correspond to the critical temperature of the uniform film and not that of the weak spot (which is somewhat depressed in many of our samples), this $T_c(H)$ is determined by the onset of an essentially normal linear I-V characteristic.

If other pair-breaking mechanisms are present, the total pair-breaking energy is the sum of the individual ones. Collisions with phonons also break pairs, so that the complete pair-breaking time is [12]

$$\Gamma^{-1} = \left(\frac{1}{\tau_s} + \frac{1}{2\tau_E} \right)^{-1} \tag{2.14}$$

which crosses over from $2\tau_E$ in zero field to τ_s in large fields. As one can see in Fig. 2.4, Γ^{-1} is too small and has the wrong field dependence to fit the data for τ_R.

But the geometric mean between τ_E and Γ^{-1} turns out to have the right order of magnitude, and furthermore, seems to be justified theoretically in the work of Schmid and Schön[12] and others[37-39].

The relaxation time in the presence of pair-breaking derived by Schmid and Schön for a homogeneous transverse mode disequilibrium (which can be produced by uniform quasiparticle injection into a film) is

$$\tau_R(T) = \frac{4k_BT}{\pi\Delta}\left(\frac{\tau_E}{2\Gamma}\right)^{\frac{1}{2}}\left(1 + \frac{\hbar^2\Gamma}{2\Delta^2\tau_E}\right)^{\frac{1}{2}} \qquad (2.15)$$

where $\Delta = \Delta(T,H)$ and $\tau_E = \tau_E(T)$. For our experiments the final factor is close to unity, so that

$$\tau_R(T,H) \simeq \frac{4k_BT}{\pi\Delta}\left(\frac{\tau_E}{2\Gamma}\right)^{\frac{1}{2}} \rightarrow \begin{cases} \dfrac{4k_BT}{\pi\Delta}\,\tau_E \equiv \tau_Q\,, & \text{for } \tau_s >> \tau_E \\ \dfrac{2\sqrt{2}k_BT}{\pi\Delta}\,(\tau_E\tau_s)^{\frac{1}{2}}, & \text{for } \tau_s << \tau_E \end{cases} \qquad (2.16)$$

Note that this reduces correctly to τ_Q for H=0 (the above relaxation time is in effect a generalized τ_Q), while in the high-field limit (typically $H \gtrsim H_{c\|}(0)/10$) one gets the geometric mean between τ_E and Γ^{-1}, with a divergence as Δ^{-1} at $T_c(H)$. Similar expressions to Eq. (2.15) have been derived by Artemenko *et al.*[37], Shelankov,[38] and Entin-Wohlman and Orbach.[39]

The temperature and field behavior of R_n for two

different samples are shown in Figs. 2.5 and 2.6. The values of R_n are plotted as a function of bath temperature T for various constant values of parallel magnetic field H. In Fig. 2.5, we also include values of R_n corrected for heating effects, as will be discussed in Section 2.4. Also plotted (the solid lines) are the corresponding theoretical values from Eq. (2.16), taking

$$\tau_E(T) = \tau_E(T_c)(T_c/T)^3 \tag{2.17}$$

$$\Delta(T,H) = \Delta(T)[1-H^2/H_{c\parallel}^2(T)]^{\frac{1}{2}} \tag{2.18}$$

$$R_n = (2\rho/wd)[D\tau_R^{(T)}]^{\frac{1}{2}} \tag{2.19}$$

and treating $\tau_E(T_c)$ as a fitting parameter for all the data from the particular sample. We find rather good agreement, considering all the uncertainties. This agreement is achieved using values of $\tau_E(T_c)$ in the range from 1 to 5×10^{-10} sec for all our samples. Variation within this range does not seem to correlate with any particular sample parameter, indicating that it may be due to uncertainties in some of the experimental constants (e.g. sample geometry and mean free path) in Eq. (2.19) which relate R_n and $\tau_R^{(T)}$. However, all of the values of $\tau_E(T_c)$ which we have inferred are in reasonable accord with other experimental and theoretical estimates of the same constant for tin.[18,19,36,40] For example, Clarke and Paterson[36] obtained 1.4×10^{-10}

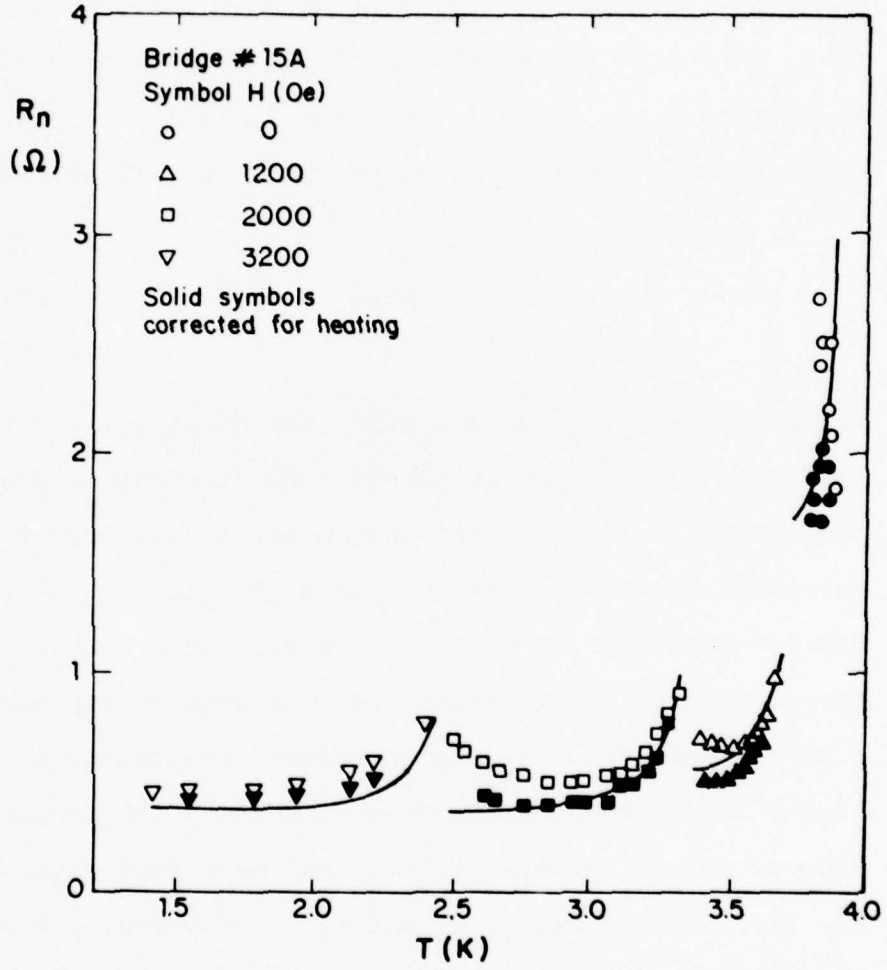

Fig. 2.5 Differential resistance R_n of the first PSC in tin bridge #15A, for various constant values of H ||J, as a function of T_{bath}. The solid curves represent the theoretical predictions of Eqs. (2.17) - (2.19), with $\tau_E(T_c) = 3 \times 10^{-10}$ sec. The solid symbols include corrections for heating-induced distortion (Section 2.4).

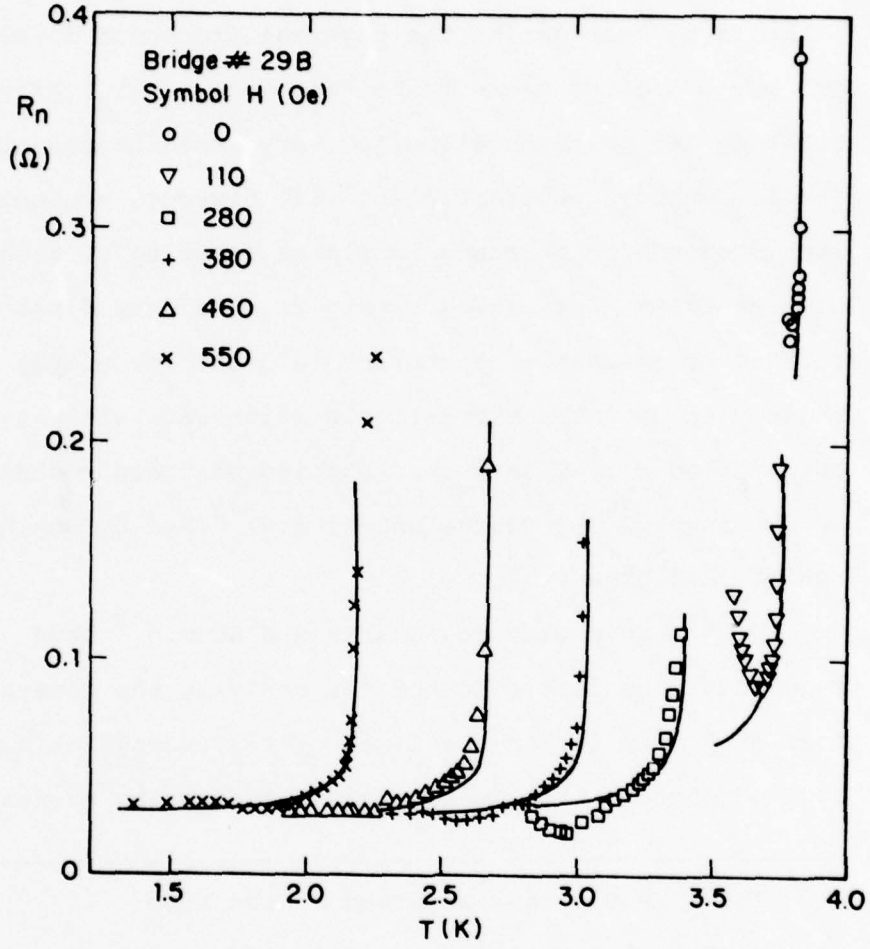

Fig. 2.6 Same as Fig. 2.5, but for bridge #29B, with $\tau_E(T_c) = 5 \times 10^{-10}$ sec.

sec * and Kaplan et al.[40] calculated 2.8×10^{-10} sec.†

The complete form of Eq. (2.16) is difficult to understand in detail, but one can gain a partial understanding by considering the physical processes involved. The basic picture seems to be that when $\tau_s << \tau_E$, pair-breaking interactions allow for very rapid branch-crossing for low energy quasiparticles. If, however, a significant amount of the branch imbalance is being created at high energies, the excess quasiparticles must first be relaxed by inelastic scattering into the low energy region, so that the overall relaxation rate will involve both τ_s and τ_E. This interpretation has been emphasized by Shelankov,[38] by Clarke and Schmid,[42] and by Entin-Wohlman and Orbach.[39]

Within this picture, Clarke and Schmid[42] have suggested a heuristic method for deriving the general form of Eq. (2.16) in the limit $\tau_s << \tau_E$. Consider a BCS superconductor, with quasiparticle scattering events

---

* Their result was expressed in the form $\tau_Q(T) = 1.0 \times 10^{-10}$ sec $[\Delta(0)/\Delta(T)]$.

† They computed a different characteristic electron-phonon time, $\tau_o = 2.3 \times 10^{-9}$ sec, which is related to τ_E by the relation[41] $\tau_E(T_c) = \tau_o/7\zeta(3) = \tau_o/8.4$.

across the Fermi surface induced by the pair-breaking interaction. The transition rate is proportional to the coherence factor[43]

$$(uu' + vv')^2 = \tfrac{1}{2}\left(1 + \frac{\xi\xi'}{EE'} - \frac{\Delta^2}{EE'}\right) \qquad (2.20)$$

where ξ is the normal electronic energy referred to the condensate chemical potential and $E = \sqrt{\xi^2+\Delta^2}$ is the quasiparticle excitation energy (a pair-breaking interaction due to magnetic fields or paramagnetic impurities is a "Type II" perturbation[43]). For scattering straight across from one branch to the other, $\xi' = -\xi$, and the coherence factor is Δ^2/E^2. This is reasonable, since a branch-crossing transition is forbidden in a normal metal where $\Delta=0$. The branch-crossing transition at a given energy will proceed at a rate $\frac{1}{\tau_s}\Delta^2/E^2$, and if this is faster than the rate at which additional nonequilibrium quasiparticles can scatter down from higher energies, the latter rate will determine the net rate of branch imbalance relaxation. The cross-over between these two rates occurs at an energy

$$E_o \sim \Delta\sqrt{\tau_E/\tau_s} \qquad (2.21)$$

and if we assume that the nonequilibrium quasiparticles are created with an initially thermal distribution, a fraction $\sim E_o/k_BT$ of the inelastic scattering events will involve scattering into the lower energy region and consequent branch imbalance relaxation. The net

branch imbalance relaxation rate is then

$$\frac{1}{\tau_R^{(T)}} \sim \frac{E_o}{k_B T} \frac{1}{\tau_E} = \frac{\Delta}{k_B T} \frac{1}{\sqrt{\tau_E \tau_s}} \qquad (2.22)$$

effectively the Schmid and Schön result in the appropriate limit.

A problem with this argument is that it is only valid when E_o is less that $k_B T$, i.e. $\tau_R^{(T)} > \tau_E$. This condition is seldom satisfied and usually strongly violated in our experiments. It is, however, the same condition under which Schmid and Schön originally derived Eq. (2.15). The preceeding argument seems to suggest that if $E_o > k_B T$, then the overall relaxation rate will be of order $\frac{1}{\tau_s} \frac{\Delta^2}{(k_B T)^2}$. Nevertheless, Shelankov[38] has proposed conditions whereby Eq. (2.16) should be valid over a wide range of fields, which seem to be approximately fulfilled in our experiments, and Schmid and Schön have made similar suggestions.[44] Furthermore, Lemberger and Clarke[45] have recently taken measurements on the branch imbalance induced by tunnel injection into superconductors doped with paramagnetic impurities, and have confirmed Eq. (2.16), again largely outside the regime in which the theoretical basis is most certain. Taken together with these other considerations, our experimental evidence helps establish a broader validity of Eq. (2.16) for the transverse relaxation time.

2.4 Heating Effects

We have discussed how the transverse mode disequilibrium determines the general form of the I-V curves. The longitudinal mode is also excited in a PSC, however, since the electric field deposits energy into the quasiparticles. In general this produces a complicated disequilibrium of the quasiparticles and the phonons, but to a first approximation most of its properties can be accounted for in terms of an increased effective temperature of the electrons, i.e. local heating. Ironically, heating effects tend to be greater at lower temperatures, since the critical current and hence the characteristic dissipation level increases. For a sufficient amount of dissipation, the raised effective temperature at the center of the PSC rises to T_c and then surpasses it, at which point the dissipative region develops into an expanding normal self-heating hotspot.[46]

The properties of this hotspot, and more generally the effects of heating in long microbridges, were discussed by Skocpol *et al.*[1,46] in terms of a simple one-dimensional macroscopic steady-state heat equation

$$-K \frac{\partial^2 T}{\partial x^2} + \frac{\alpha}{d}(T-T_{bath}) = JE \qquad (2.23)$$

where d is the film thickness, α is the heat transfer coefficient per unit area (the reciprocal of the thermal boundary resistance), K is the thermal conductivity of the metal, and JE is the Joule heat per unit volume.

Conceptually, this equation balances heat production against conduction along the bridge and surface heat transfer across the interface with the substrate or He bath. The length scale is characterized by a "thermal healing length"

$$\eta = (Kd/\alpha)^{\frac{1}{2}} \qquad (2.24)$$

which represents the decay length of the temperature near a localized heat source.

We are assuming in Eq. (2.23) that the energy enters the electronic system, is transported along the bridge by quasiparticles (the lattice thermal conductivity can be neglected near the critical temperature of a superconductor), and is transferred out of the film via phonons. Since the electrons and phonons in the film can be characterized by some temperature T, which is larger than the bath temperature T_{bath}, the bottle-neck in the energy transfer is not between the electrons and the phonons in the film, but between the phonons in the film and those in the thermal bath. This is supported experimentally by the fact that when the He bath passes through the lambda-point transition, there is an abrupt change in the effective electron temperature, because of the greatly enhanced phonon transfer to superfluid He.[46,*]

---

* There is some evidence in the Russian literature[47] that under certain circumstances (below the lambda-point, and for a wide range of temperatures for extremely narrow films) the heating can be described in terms of electron "super-heating" relative to the lattice.

Near the critical temperature, the electronic thermal conductivity is approximately that in the normal metal[48], since only the quasiparticles and not the superconducting pairs can transport entropy. We can therefore write, using standard kinetic theory,

$$K = C_{el} D \tag{2.25}$$

where D and C_{el} are the diffusion constant and heat capacity of the normal metal at T_c. The thermal conductance to the bath can be expressed in terms of the phonon properties

$$\frac{\alpha}{d} = C_{ph}/\tau_{esc} \tag{2.26}$$

where C_{ph} is the phonon heat capacity and τ_{esc} is the characteristic escape time of a phonon out of the film. The thermal healing length of Eq. (2.24) can then be written as

$$\eta = \sqrt{D\tau_{esc} C_{el}/C_{ph}} \equiv \sqrt{D\tau_{eff}} \tag{2.27}$$

where τ_{eff} is the effective electronic cooling time. Furthermore, by detailed balance and energy conservation we have

$$C_{ph}/\tau_{ph} = C_{el}/\tau_E \tag{2.28}$$

where τ_{ph} is the inelastic phonon-electon collision time (i.e. the average time for a given phonon to scatter inelastically off any electron). Therefore we can write

$$\tau_{eff} = \tau_E \, (\tau_{esc}/\tau_{ph}) \tag{2.29}$$

This is completely analogous to previous studies of nonequilibrium quasiparticle recombination times at low temperatures.[49] The "hot" electrons diffuse a distance $\sqrt{D\tau_E}$ before coming to equilibrium with the phonons in the film. In the limit that the phonons in the film are maintained in equilibrium at the bath temperature, $\tau_{eff} = \tau_E$.* In the more usual case of "phonon trapping", however, $\tau_{esc} >> \tau_{ph}$, and a hot phonon is much more likely to interact with the electrons to maintain the heated electron distribution than to escape the film, producing an enhancement by the factor τ_{esc}/τ_{ph} in the relevant quasiparticle relaxation time. In general, whenever phonon trapping is dominant, the spatial extent of heating gives no information on the intrinsic quasiparticle relaxation time, but rather provides a measurement of the phonon escape time. Note that a similar argument does <u>not</u> apply to the case of the transverse mode, since nonequilibrium phonons, being uncharged, cannot create or maintain a branch imbalance.

---

* This should be distinguished from the longitudinal relaxation time for transient processes in the superconductor, which near T_c takes the form[12]

$$\tau_R^{(L)} = \frac{\pi^3}{7\zeta(3)} \frac{k_B T}{\Delta} \tau_E$$

The difference between this divergent time and the steady-state relaxation time, which goes over continuously to the normal time τ_E at T_c, is due to the fact that in the former case the gap itself is changing in time. That these two should be different seems not to be generally appreciated.

For the SBT model of the PSC, where the electric field E decays exponentially over the distance Λ, Eq. 2.23 can be solved explicitly, yielding a temperature rise $\delta T = CVI$ in the center of the PSC[1,46], where the heating coefficient C is

$$C = \frac{1}{2(\eta+\Lambda)w\alpha} \qquad (2.30)$$

This is essentially what one would expect for a power input VI distributed over a distance 2Λ producing a temperature rise extending out over the larger range $2\Lambda + 2\eta$.* A rough estimate of the heating coefficient can be made as follows. For small values of the gap, most of the heat conduction is carried by quasiparticles, and the thermal conductivity is approximately that of the normal metal, which can be determined from the resistivity ρ using the Wiedemann-Franz law ($K=\pi^2 k_B^2 T/3e^2\rho$). The thermal boundary conductance α scales as T^3 since it is proportional to the density of phonons, so that $\eta = \sqrt{Kd/\alpha}$ should scale as T^{-1}. Values of $\alpha(T_c)$ of the order of 2 watts/cm^{2}K have been inferred from the I-V characteristic of long tin microbridges in the self-heating hotspot regime[46], where dissipation sustains the local temperature above T_c.

---

* We have assumed here that the heat generated goes as $JE \propto \exp(-x/\Lambda)$. It may be, on the other hand, that the heat from the normal component is generated as $J_n E \propto \exp(-2x/\Lambda)$, which will produce a heated region $\simeq 2\eta+\Lambda$, and the heat from the condensate component is generated in the core region, producing a heating region $\simeq 2\eta$. In any case, this treatment is only approximate, and furthermore, η is generally $>>\Lambda$ for our data.

We will assume that this heating analysis remains essentially valid near the reduced $T_c(H)$ in a magnetic field. The presence of the magnetic field will not affect the phonon properties, and the magnitude of the field is not large enough to produce any significant magnetoresistive effects in the relatively dirty thin-film samples.

If heating is important, of course, then one is no longer justified in simply substituting the bath temperature into Eq. (2.16) for the transverse relaxation time. If η is much larger than Λ, however, then the temperature rise at the PSC is approximately constant over the scale of Λ, and one can use the heating coefficient C to determine the raised temperature for substitution into Eq. (2.16). From the above estimates of η, we find that η is approximately twice Λ for H=0, whereas for larger H and lower T, η increases while Λ decreases substantially. To a first approximation, therefore, one can take the temperature rise to be constant within the PSC.

In the SBT model, the isothermal characteristic of a PSC in the plateau region is

$$V = R_n(I-\bar{I}_s) = R_n(I-fI_c) \qquad (2.31)$$

where f is a fraction ($\sim\frac{1}{2}$) which is at least approximately independent of T. Then, since heating causes I_c to decrease, it causes V to increase if I remains fixed.

If R_n diverges at $T_c(H)$, heating causes R_n to increase, thus furthering the same trend. Therefore, since the heat dissipation IV increases with increasing I, the slope dV/dI will increase as I increases. In our presentation of the I-V curves, with I along the horizontal axis, the curve turns upward in a region where it would otherwise be straight. Another characteristic indication of heating is the steepening at the onset of the PSC and the ultimate appearance of hysteresis between the zero-voltage and dissipative states for current-biased measurements. Again, this is because I_c in the dissipative state can be significantly below that corresponding to the bath temperature. These two trends can be seen in Fig. 2.7, where a set of simulated I-V characteristics are shown with and without heating effects included.

For this simulated model of heating, we take the set of I-V curves determined by the equation

$$V = \frac{R_n I_c}{\ell n[I/(I-I_c)]} \quad , I > I_c \tag{2.32}$$

where

$$I_c = I_{co}(1-T/T_c)^{3/2} \tag{2.33}$$

and

$$R_n = R_o(1-T/T_c)^{-\frac{1}{2}} \tag{2.34}$$

These isothermal curves (the solid lines in Fig. 2.7) are very steep near T_c, and for large I approach asymp-

Fig. 2.7 Simulated I-V curves calculated from Eqs. (2.32) - (2.34) with and without heating effects included, using parameters I_{co} = 22 mA, R_o = 0.55 Ω, and C = 2×10^6 K/W. These curves are modeled after the experimental curves of Fig. 2.8. The inset shows how the minimum differential resistance of the I-V curve varies with T_{bath}, with and without heating.

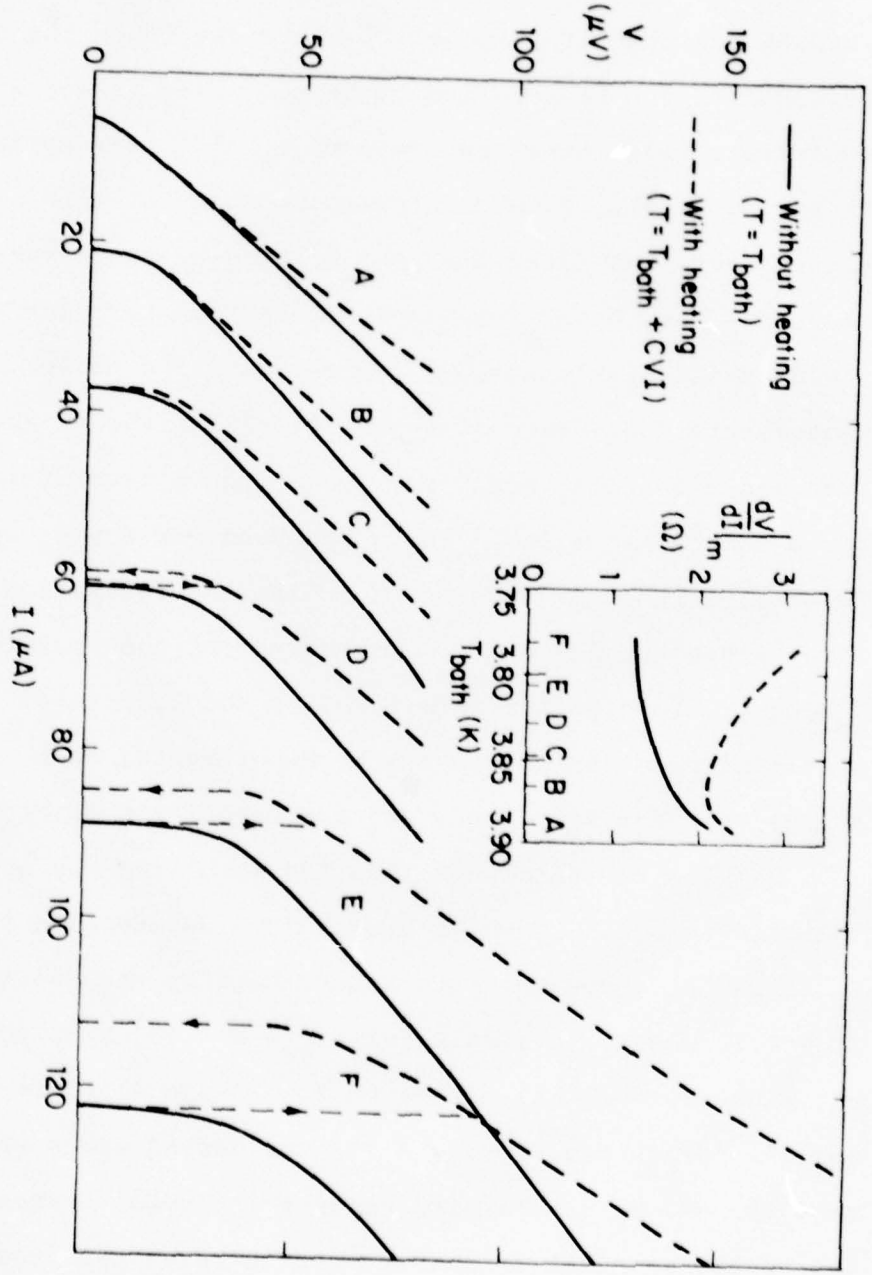
V (μV)
0
50
100
150
20
40
60
80
100
120
I (μA)
A
B
C
D
E
F
Without heating (T = T_bath)
With heating (T = T_bath + CVI)
dV/dI|_m (Ω)
0
1
2
3
3.75
3.80
3.85
3.90
T_bath (K)
F E D C B A

Fig. 2.7

totically the straight line $V = R_n(I-\frac{1}{2}I_c)$. The analytic form of Eq. (2.32) follows from a modified resistively shunted junction (RSJ) model,[50] where one takes the supercurrent-phase relation to be piecewise linear with an average value over the cycle of $\bar{I}_s = \frac{1}{2}I_c$ (see Appendix II for details). A current-phase relation of this general form was found for long bridges by DC measurements.[50] Many other reasonable current-phase relations yield qualitatively similar I-V curves. The above temperature dependence of the critical current is the standard mean-field behavior, and is the correct form for a long microbridge. The given behavior for R_n is in accord with a divergence of Λ^{-1} in the relaxation time within the SBT model. The values of the coefficients R_o and I_{co} in Fig. 2.7 were fixed by modeling this system after a particular set of experimental data, Bridge #15A for H=0, presented for comparison in Fig. 2.8.

Heating is introduced into the simulation by assuming that the temperature which enters into determining I_c and R_n is raised above the bath temperature by the quantity $\delta T = CVI$, where the single value $C = 2 \times 10^6$ K/W, consistent with experimental estimates for Bridge #15A, is used for all the curves in Fig. 2.7. The dashed lines represent the set of curves with heating included, corresponding to the same set of bath temperatures as the isothermal

Fig. 2.8 Experimental I-V curves for Sn bridge #15A for H = 0, for a range of temperatures near T_c. The temperatures, together with the corresponding measured values of R_n, are: curve a - T=3.889 K, R_n=1.83 Ω; B 3.867 K, 2.05 Ω; C 3.849 K, 2.49 Ω; D 3.828 K, 2.4 Ω; E 3.806 K, 2.55 Ω; F 3.782 K, 2.55 Ω. These curves are to be compared with the corresponding simulated I-V curves in Fig. 2.7.

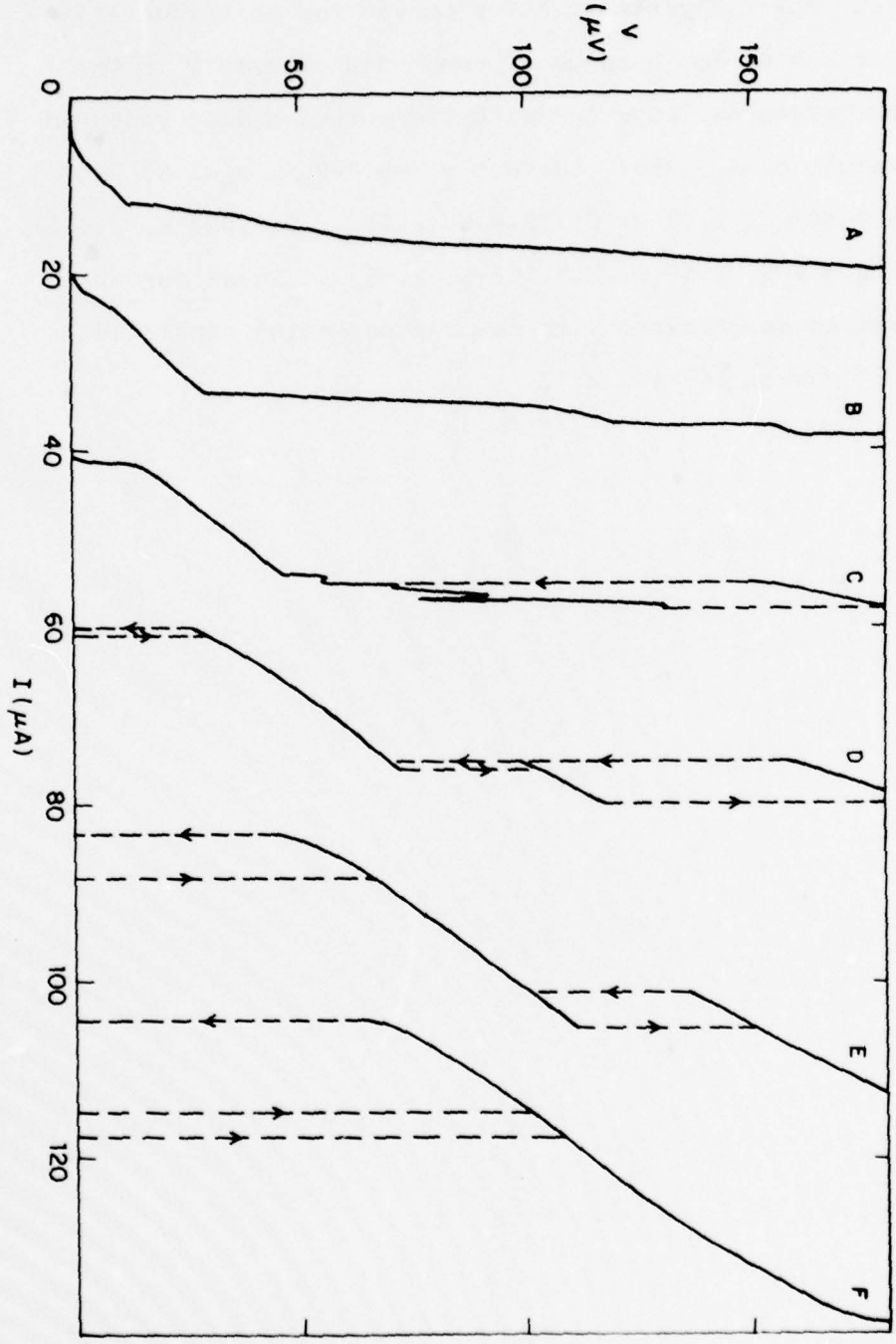

Fig. 2.8

curves. Note that the heating-induced distortion increases quite strongly the farther one goes from T_c. This follows from the fact that both V and I scale with I_c in the isothermal curve, so that the heat dissipation VI goes as I_c^2 for comparable positions along the curve.

If heating were negligible, the best measurement of the resistance R_n could be made at the largest current before the second PSC entered, since the curve is asymptotic to the straight line with slope R_n. In the presence of heating, with the tendency toward increasing values of dV/dI for large currents, we take the slope at the largest current before heating becomes evident, i.e. we take the minimum value of dV/dI. As one gets farther from T_c and heating becomes more significant, however, this becomes a less and less reliable method of measuring the appropriate slope. Since the intrinsic isothermal curve is concave downward and heating tends to make this concave upward for large currents, there can often be a deceptively straight region of the curve around dV/dI_{min}, which however is significantly greater in slope than R_n. This is evident from the inset of Fig. 2.7, which shows the major effect of heating upon dV/dI_{min}. In the case of the simulation here, the intrinsic resistance R_n (the solid curve) is decreasing as one moves away from T_c, while beyond a certain point the minimum value of

dV/dI with heating is increasing. The same thing occurs in our experimental data, and when heating is very significant, this can obscure the divergence in the relaxation time as $T \to T_c(H)$.

The hysteresis in the critical currents is also quite similar between Figs. 2.7 and 2.8. In part, this may be because the value of C was chosen so as to match the onsets of hysteresis in the two cases. The development of hysteresis for lower temperatures is also in good agreement, however, implying that this hysteresis may be largely attributed to heating. On the other hand, a few reservations about hysteresis may be in order. For one thing, constant current-biasing in a noisy environment may lead to premature switching to the dissipative state or back again (see e.g. curve F in Fig. 2.8), leading to a possible underestimate of the actual hysteresis. Secondly, the apparent onset of hysteresis in our samples[51] tended to occur at about 30 to 50 mK from T_c (in zero field), whereas measurements on similar samples of Skocpol,[51] taken in an rf-shielded room, indicated an onset considerably closer, typically 5 - 10 mK from T_c. It may be that some hysteresis in our data is hidden by rf noise-rounding, in spite of the rf filters used. (Note, in this regard, the rounded onsets of the non-hysteretic curves in Fig. 2.8.) In that case, an alternative explanation of hysteresis close to T_c might be

$\dot{Q}$ is the Joule heat per unit volume.

required (a possible source of intrinsic hysteresis is discussed in Chapter IV).

In practice, we do not know whether any simple set of formulas such as Eqs. (2.32) - (2.34) can actually generate our experimental I-V curves. We were able, however, to reconstruct isothermal curves from our raw data, at least when the heating-induced distortion was not too great (in particular, necessary information is lost in hysteresis). The procedure begins by considering a set of I-V curves for constant H and a series of bath temperatures near $T_c(H)$, as in Fig. 2.9a. Given a value for the heating coefficient C, the raised local temperature $T_{local} = T_{bath} + CIV$ can be computed at various points along each curve of the set. One can then connect the points corresponding to the same value of T_{local}, interpolating where necessary, to obtain a family of isothermal curves. The curves in Fig. 2.9a were processed in this way to yield those of Fig. 2.9b, using for simplicity a single value of C for all the curves. The magnitude of C was chosen so as to bring the greatest reduction in the amount of heating-induced curvature for the whole set of curves.

The values of C obtained in this way for several values of H are plotted in Fig. 2.10 as a function of T_{bath}. The horizontal bars represent the range of

under certain circumstances (below the lambda-point, and for a wide range of temperatures for extremely narrow films) the heating can be described in terms of electron "superheating" relative to the lattice.

Fig. 2.9 I-V curves for bridge #15A for H = 2000 Oe (||J) before and after processing to remove heating-induced distortion. a) Raw I-V curves for the first PSC. b) Reconstructed isothermal curves corresponding to the bath temperatures in (a). See text for clarification. Curves for bath temperatures N and O are not reconstructed because this would require extrapolation byond the measured data. Bath temperatures: A, 3.309 K; B, 3.284; C, 3.250; D, 3.212; E, 3.149; F, 3.086; G, 3.037; H, 2.977; I, 2.939; J, 2.852; K, 2.775; L, 2.670; M, 2.622; N, 2.546; O, 2.501.

$$\tau_{eff} = \tau_E \, (\tau_{esc}/\tau_{ph}) \qquad (2.29)$$

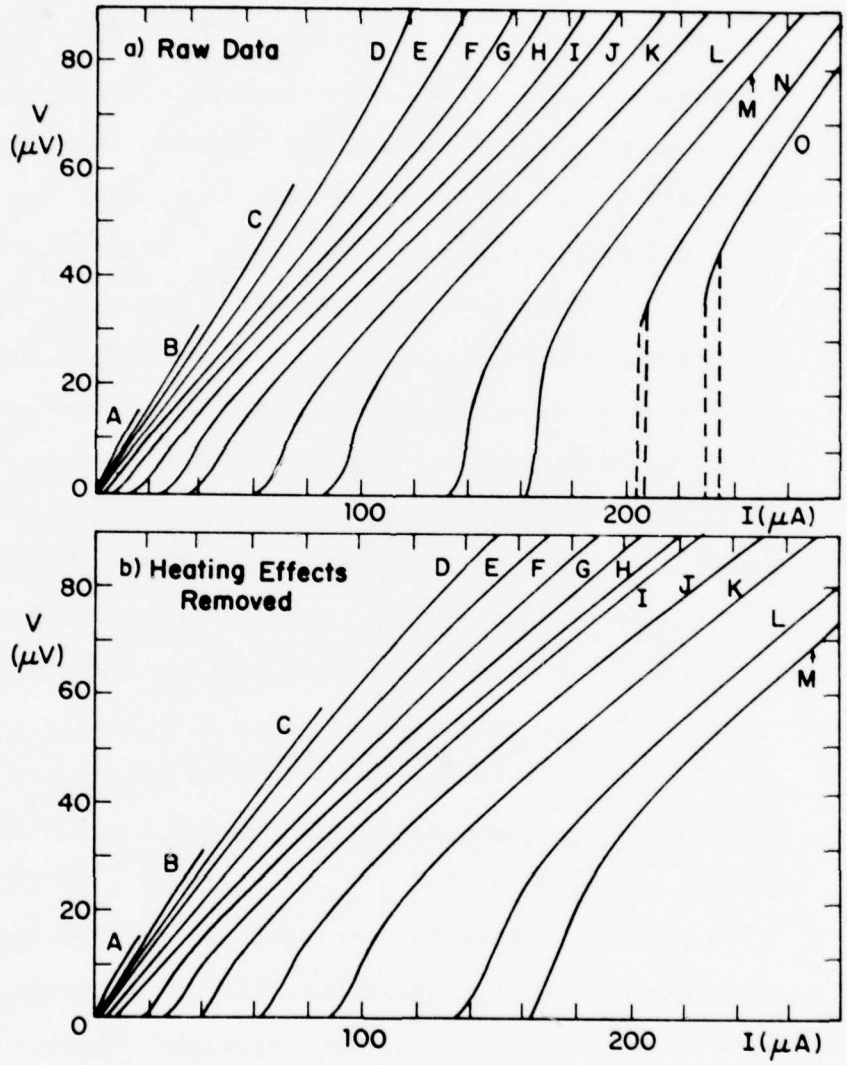

Fig. 2.9

these two should be different seems not to be generally appreciated.

temperatures over which the fit was made, and the vertical bars are the estimated uncertainties. These values are compared to independent estimates of C obtained from Eq. (2.30) and experimental parameters. The value of $\alpha(T_c)$ is known only roughly, from data by Skocpol[46] in the self-heating hotspot regime. In Fig. 2.10, curves are plotted using $\alpha(T_c) = 2$ and 3 W/cm^2K for $T > T_\lambda$ (where heat is transferred primarily to the substrate rather than directly to the normal He bath) and 8 W/cm^2K below the lambda point, where heat transfer out of the film suddenly increases due to the superfluid He. Since we are comparing with data in the presence of magnetic fields near $T_c(H)$, the lower temperatures correspond to higher fields, where $\Lambda \ll \eta$ and C becomes effectively a function only of T. Above about 3.4 K, however, $\Lambda(H)$ is sufficiently large compared to η to cause a significant dependence of C on magnetic field. The computed curves there are not unique, but use typical values of $\Lambda(H)$.

Overall, considering the roughness of the approach, the agreement between these two sets of estimates for C seems to be quite satisfactory, providing support for the simple heating model of Skocpol *et al.*[1,46] The evidence seems to indicate that the "electron heating" is dominated by phonon-trapping effects (at least for $T > T_\lambda$), so that

from the condensate component is generated in the core region, producing a heating region $\simeq 2\eta$. In any case, this treatment is only approximate, and furthermore, η is generally $>>\Lambda$ for our data.

Fig. 2.10 Heating coefficient C versus bath temperature for bridge #15A. The experimental points, marked by ⊢⊣, represent constant values chosen to minimize apparent heating-induced distortion for a set of I-V curves over a range of temperatures, with the indicated uncertainty. The lines represent semi-empirical predictions of Eq. (2.30), using typical values of $\alpha(T_c)$ and typical variation of $\Lambda(H)$. At the onset of superfluidity in the He bath (2.18 K), the appropriate value of $\alpha(T_c)$ changes abruptly, due to the additional heat-transfer ability of the superfluid.

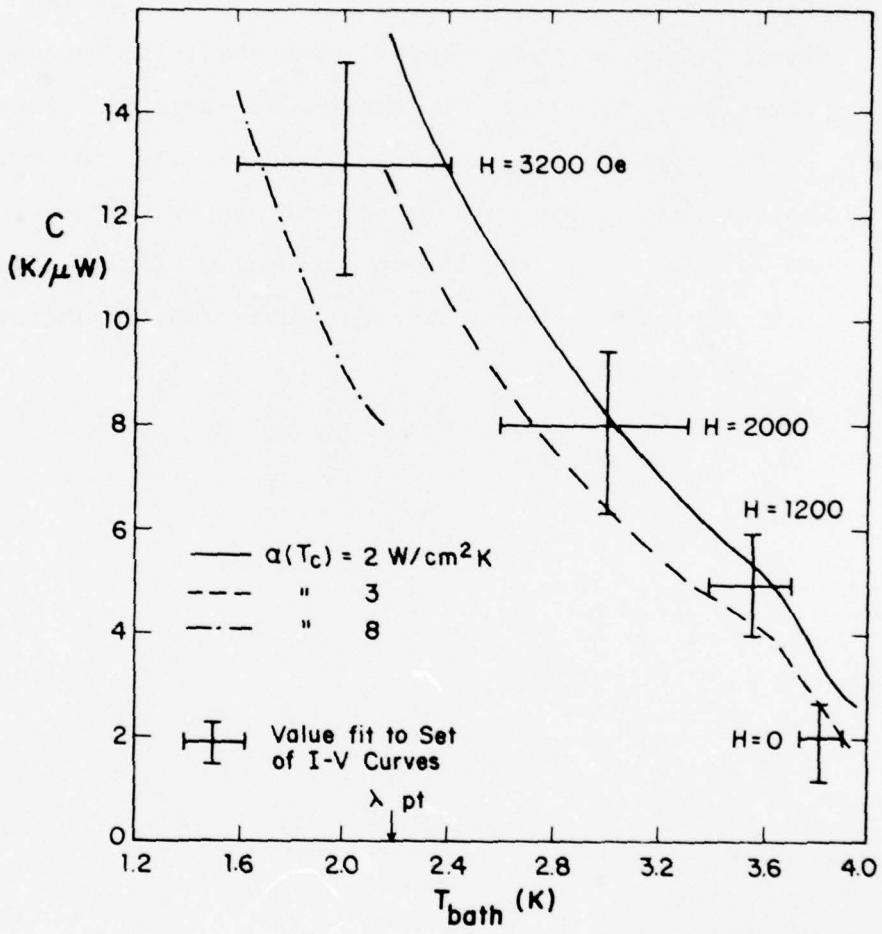
C
(K/μW)
14
12
10
8
6
4
2
0
1.2
1.6
2.0
2.4
2.8
3.2
3.6
4.0
T bath (K)
H = 3200 Oe
H = 2000
H = 1200
H = 0
α(T_C) = 2 W/cm²K
" 3
" 8
Value fit to Set
of I-V Curves
λ pt

Fig. 2.10

we are probably unable to obtain any information on the effect of the magnetic field on the intrinsic longitudinal relaxation time from the variation of the thermal healing length with field. In contrast to the transverse mode case, however, we would not expect the field to have a dramatic effect, since near $T_c(H)$ the intrinsic steady-state relaxation time should be approximately the electron-phonon collision time $\tau_E(T)$, which is essentially independent of magnetic field.

Using the curves corrected for heating effects, we have found that the variation of $\tau_R^{(T)}$ for constant H can be described fully by a divergence as $T_c(H)$ is approached; the increase of $dV/dI_{min}(T)$ in the raw data far from $T_c(H)$ is due to heating. This can be seen, for example, in the data in Fig. 2.5 for H = 1200 Oe. Using the data corrected for heating, we are able to provide a better fit to the Schmid and Schön formula Eq. (2.16).

Heating is a fundamental problem intrinsic to uniform one-dimensional superconducting filaments. An estimate of the degree of heating-induced distortion in zero field can be found in the dimensionless parameter

$$\gamma = \frac{\delta T}{T_c - T} = \frac{I_c^2 R_n}{2(\eta+\Lambda) w \alpha (T_c - T)}$$

$$= \frac{\eta^2}{K} \frac{J_c^2/\sigma}{T_c - T} \frac{\Lambda}{\eta+\Lambda} \qquad (2.35)$$

which represents the relative temperature rise at the characteristic dissipation level $I_c^2 R_n$. Here σ is the normal-state conductivity and J_c is the critical current density, which for H=0 in the dirty limit near T_c takes the form (see ref. 52 and Eqs. (3.28) and (3.29) in Chapter III)

$$J_c = n_s e v_c = \frac{\sigma}{2e\tau_o} \frac{2}{3} \frac{\hbar}{\sqrt{3}\xi(T)}$$
$$= 2.837 \frac{k_B(T_c-T)}{e\xi(T)} \qquad (2.36)$$

Then, using the Widemann-Franz law and estimating $\Lambda/(\eta+\Lambda) \simeq 1/3$, we obtain the very simple expression

$$\gamma \simeq \tau_{eff} \frac{\Delta(0)}{\hbar} (1-T/T_c)^2 \qquad (2.37)$$

where τ_{eff} is the effective cooling time discussed earlier.

This heating parameter is independent of the sample width, the electron mean free path, and even the thickness of the film (provided it is small enough to optimize phonon escape). Furthermore, since $\tau_{eff} \gtrsim \tau_E$, the coefficient $\tau_{eff}\Delta(0)/\hbar$ is very large, about 1000 for Sn. Even if T is within 1% of T_c, which is typical for our data, $\gamma \sim 0.1$, corresponding to a significant amount of heating and consequent distortion. For Al, with a value of τ_E two orders of magnitude larger than that for Sn, heating should be an even more serious problem at comparable reduced temperatures. In the clean

limit $\ell >> \xi_o$, γ is reduced by a factor $\propto \xi_o/\ell$, but it is difficult to obtain thin-film samples clean enough for this to apply (although it may in clean whisker crystals). The presence of a parallel magnetic field will reduce heating somewhat because of the lower characteristic resistance $R_n \propto \Lambda$, but heating will still be quite significant. The method we have used to reduce the effects of heating to manageable proportions is to produce a localized reduction in the critical current I_c, which will reduce the heating parameter γ by a factor of I_c^2. We will discuss the use of these localized weak spots further in the next section.

2.5 Localized Weak Spots

The critical currents of successive PSC's in a bridge which is nominally uniform can vary somewhat, due to slight variations in T_c or in cross-section along the bridge,[1,21] or to the influence of one PSC on others nearby.[1,53,54] Even so, it is often difficult in such uniform bridges to make certain that in following the PSC with the smallest I_c through large variations in T and H, one is actually following the same single unit. Furthermore, near $T_c(H)$ the second PSC often enters before the first PSC has reached the plateau region in its I-V curve, making an accurate determination of R_n difficult. For these reasons, a sample having a single deliberate "weak spot" associated with a locally reduced value of I_c is highly advantageous. In addition, since the heat dissipated at the PSC is of order $I_c^2 R_n$, decreasing I_c reduces the heating-induced distortion of the I-V curve substantially. Since we are interested in probing the nonequilibrium properties of the uniform region outside the weak spot, however, the length of this weak spot should be small compared with Λ and the resistance it contributes should be small compared with R_n.*

* If the weak spot is made by a constriction, it will add some additional resistance even if it is short. The requirement that this additional resistance be small relative to R_n puts a practical limit on the degree to which the critical current may be reduced by the constriction weakening illustrated in Fig. 2.2.

For a uniform bridge without a weak spot, the I-V curves are relatively independent of the orientation of the magnetic field relative to the direction of the current density J, as long as it is within the plane of the film. The critical current I_c of a weak spot, however, is depressed far more in a large magnetic field $H \parallel J$ (and perpendicular to the cut) than it is for the same field with $H \perp J$ (and parallel to the cut). For $H \perp J$, the critical current of the weak spot seems to behave similarly as a function of H and T to the corresponding I_c's of the other PSC's. The relative "weakness" of the weak spot is then presumably due to a simple decrease in the local cross-sectional area. For $H \parallel J$, on the other hand, not only is I_c of the weak spot smaller than that of the other PSC's, but it also goes to zero at a lower temperature. This seems to be particularly true for the "groove" type of weak spot (Fig. 2.2c) where the cross section at the weak spot is not really reduced at all. We note that in this orientation, the field has a component perpendicular to the surface at the weak spot. Since perpendicular critical fields are substantially smaller than parallel critical fields, a depression of the critical temperature $T_c(H)$ at the localized weak spot is not unreasonable. We will discuss some further aspects of the critical currents of these magnetically weakened regions in Section 5.2.

Due to the localized depression of $T_c(H)$, there is a significant range of temperatures for large H ||J where I_c of the weak spot has already gone to zero, whereas that of the second PSC has not. We are therefore able to extract $\tau_R^{(T)}$ from R_n of the first PSC over this entire range, and we find that nothing unusual happens when I_c of the weak spot (and presumably also the local value of the gap Δ) goes to zero.* The divergence of $\tau_R^{(T)}$ seems to occur at the undepressed value of $T_c(H)$ as determined by the higher PSC's. This is shown in Fig. 2.11a, where R_n^{-4} is plotted versus T to show that the divergence of R_n as $[1-T/T_c(H)]^{-\frac{1}{4}}$ occurs at a temperature 150 mK above the temperature where I_c went to zero. This can be understood by noting that the magnetic depression of I_c of the weak spot is a highly localized phenomenon. Outside this region, yet still within the range of the quasiparticle diffusion length, the appropriate critical temperature becomes that corresponding to the uniform film. The same is true, although to a much lesser extent, for a uniform bridge in zero magnetic field (see Fig. 2.11b). Even for the uniform bridge,

---

* When the center region has gone normal, what we have is more correctly an SNS junction than a phase-slip center. Some recent measurements[18] on large-area SNS junctions confirm that the excess resistance contributed by the superconductor corresponds near T_c to the length $\Lambda = \sqrt{D\tau_Q}$ on either side of the normal region.

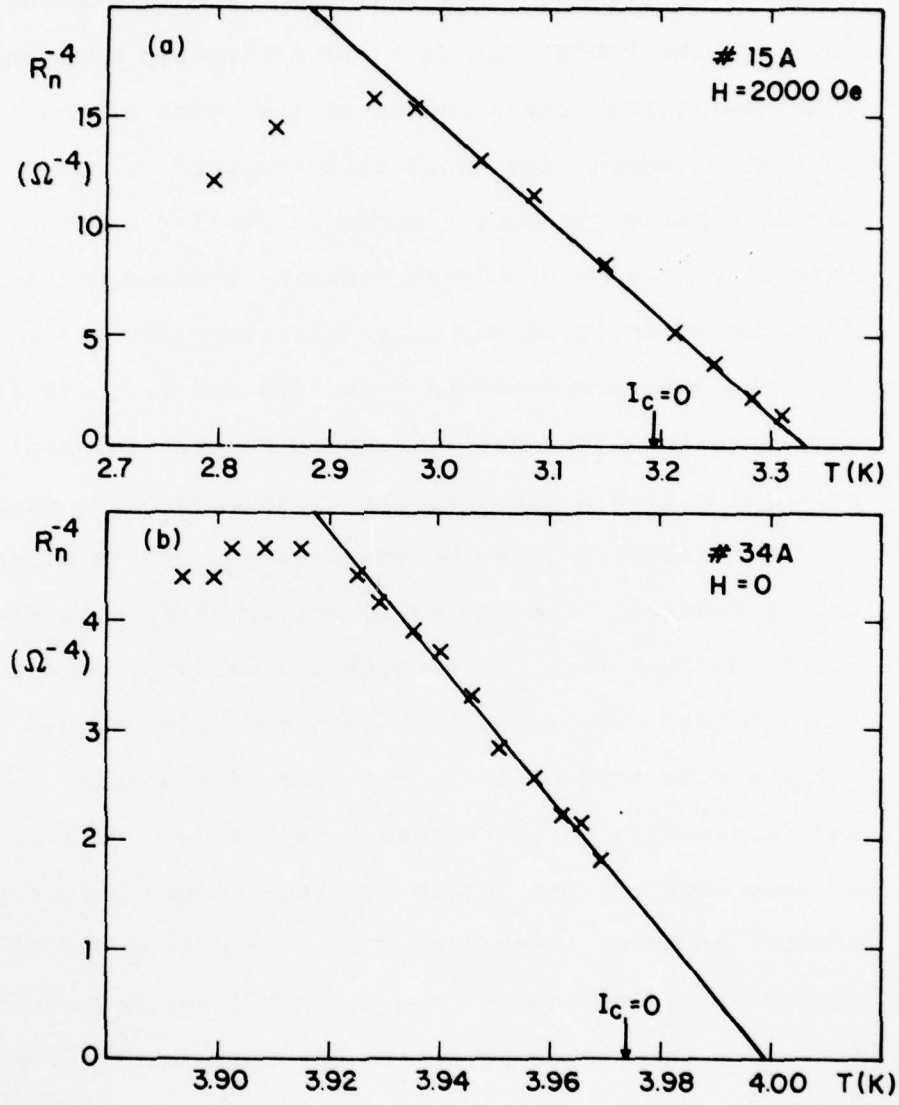

Fig. 2.11 Experimental data for R_n^{-4} vs. T, showing the range over which the divergence of the form $R_n \propto \Delta^{-\frac{1}{2}} \propto (1-T/T_c)^{-\frac{1}{2}}$ is observable. Note that the temperature at which I_c goes to zero is in each case less than the extrapolated value of $T_c(H)$. a) Bridge #15A, H = 2000 Oe. b) Bridge #34A, H = 0.

there are significant local variations of T_c, typically about 30 mK for Sn,[1,19] which cause some of the variation in I_c of the PSC's. Since I_c is determined by local characteristics over a region of the order of the coherence length, the "nucleation center" of a PSC may be expected to have a somewhat smaller value of T_c than that of some of the surrounding regions within a distance of the quasiparticle diffusion length Λ.

The data presented in Figs. 2.5 and 2.6 come from samples with magnetically weakened spots. In samples not containing such a feature, the divergence of R_n near $T_c(H)$ is often largely hidden by the presence of the other PSC's and by heating. The nominally uniform sample in Fig. 2.11b was less than 200 Å thick and was well-adhered to the sapphire substrate, both features which should optimize the conduction of heat out of the film. Yet data indicating the divergent behavior covered a range of only about 50 mK, before heating-induced distortion started becoming important. This distortion can be approximately removed by the methods described earlier to extend this range somewhat, but it remains quite limited. Compare this to Fig. 2.11a, where the corresponding data for a bridge with a magnetically weakened spot (not particularly optimized for heat removal) shows the divergent behavior over a range of 300 mK. It is perhaps ironic, but nontheless true, that it is necessary to use a weak spot to probe the properties of a uniform film.

2.6 Conclusions

In summary, we have examined the I-V curves of long tin microbridges in parallel magnetic fields and have successfully interpreted them within the phase-slip center model of Skocpol, Beasley, and Tinkham.[1] The differential resistance in the plateau region of the PSC, after correcting for dissipative effects using a simple heating model, is set equal to the normal resistance R_n of a region of the bridge with length $2\sqrt{D\tau_R}$, where D is the quasiparticle diffusion constant and τ_R is the appropriate relaxation time. The temperature and field dependence of τ_R thus inferred from our data agrees well with that of the transverse mode relaxation time in the presence of pair-breaking derived by Schmid and Schön[12] [Eq. (2.15)]. The values of $\tau_E(T_c)$ which provide the best fit with the data fall between 1 and 5×10^{-10} sec, and much of this scatter can be attributed to an uncertain knowledge of the experimental factors relating the measured resistance to the corresponding time. In any case, these figures are generally consistent with other estimates obtained for this constant in tin, both experimentally and theoretically. The elucidation of the role of heating in modifying the I-V characteristics has been very important in gaining a more complete understanding of them. By using a semi-empirical heat transfer

model with local heating, corresponding to the regime of phonon trapping, we have been able to account for most of these heating induced distortions. Finally, we re-emphasize the importance of the deliberately inserted weak spots, which caused significant depression of I_c for large $H \| J$, in allowing us to extend substantially the temperature range near $T_c(H)$ where data relatively undistorted by heating could be obtained.

CHAPTER THREE: CHARGE IMBALANCE DYNAMICS IN NONEQUILIBRIUM SUPERCONDUCTORS

3.1 Introduction

We now step back from phase-slip centers to examine more generally the dynamics of charge imbalance in nonequilibrium superconductors. Using a generalized two-fluid approach to BCS superconductors near T_c, we derive in Section 3.2 a charge imbalance wave equation, which provides a unified picture capable of dealing with both steady-state branch imbalance relaxation and high-frequency collective mode propagation. We show in Section 3.3 that the associated equations for the nonequilibrium currents and potentials are isomorphic to equations which describe electrical signals on a simple classical transmission line, and proceed to use analogies with this well-known case to illustrate directly and graphically the physical significance of the nonequilibrium processes. In Section 3.4 we demonstrate the facility of this transmission-line picture, as well as some of its limitations, by discussing a number of previous experiments involving nonequilibrium potentials in superconductors, and make some predictions for experiments yet to be performed. We conclude Chapter III by summarizing those elements of the analysis which will be useful in developing our model for the phase-slip center in Chapter IV.

3.2 Derivation of Charge Imbalance Waves

Our approach to charge imbalance dynamics follows in part the treatments of Waldram[10] and Pethick and Smith.[24] While many of our results have been obtained previously, our heuristic derivation of the charge imbalance wave equation clarifies the physical origin of the waves and brings out certain aspects not previously emphasized. The quantitative results are strictly limited to a regime very close to T_c in the absence of pair breaking, but we expect that the qualitative picture has a wider validity.

The electronic charge density in a BCS superconductor is

$$Q_e = 2e \sum_k [u_k^2 f_k + v_k^2 (1-f_k)] \qquad (3.1)$$

where the sum is over all electronic k-states (with the factor of two for the spins) and f_k is the quasiparticle distribution. The ion cores, of course, contribute an equal and opposite charge to maintain overall charge neutrality. The factors u_k^2 and v_k^2 can be interpreted as the probabilities that a given quasiparticle state represents an electron and a hole respectively, and are given by

$$u_k^2 = 1 - v_k^2 = \tfrac{1}{2}(1 + \xi_k/E_k) \qquad (3.2)$$

where

$$E_k = (\Delta^2 + \xi_k^2)^{\frac{1}{2}} \; ; \; \xi_k = \varepsilon_k - \varepsilon_s \qquad (3.3)$$

Here E_k is the quasiparticle excitation energy, positive on both the electron-like ($\xi_k>0$) and the hole-like ($\xi_k<0$) branches of the excitation spectrum, Δ is the BCS gap parameter, and ξ_k is the electron kinetic energy referred to the chemical potential ε_s of the superconducting condensate (which may be different from the Fermi energy $\varepsilon_F \equiv 0$). For simplicity, we have dropped the terms involving the superfluid velocity[55], even though this approximation may be valid only in situations where the supercurrent is small compared to the critical current.

We can express Q_e as the sum of the two components

$$Q^* = 2e\sum_k f_k(u_k^2 - v_k^2) = 2\sum_k q_k f_k \qquad (3.4)$$

and

$$Q_c = 2e\sum_k v_k^2 \quad . \qquad (3.5)$$

Q^* is the net charge density in the quasiparticle system, commonly called the branch imbalance or charge imbalance.* The quantity

$$q_k = e(u_k^2 - v_k^2) = e\,\xi_k/E_k$$

in Eq. (3.4) can be regarded as an "effective charge"

---

* Notation and units vary; our Q^* has units of charge density, that of refs. 9 and 14, number density ($=Q^*/e$), and that of ref. 10, energy ($=Q^*/2N(0)e$). The quantities $\delta Q_n^{l.e.}$ and δQ_n in ref. 24 are related to our Q^* by

$$\delta Q_n^{l.e.} = \frac{4k_BT}{\pi\Delta}\,\delta Q_n = Q^*/e \quad .$$

for a given quasiparticle. The remaining part Q_c of the total electronic charge density can be attributed to the condensate, but should not be confused with the superfluid density $n_s \propto \Delta^2$.

When the electronic system is in equilibrium, $\varepsilon_s=0$, and f_k is simply the Fermi function f^o, given by

$$f^o(\varepsilon_k) = [1 + \exp(\sqrt{\varepsilon_k^2 + \Delta^2}/k_B T)]^{-1} \qquad (3.7)$$

where k_B is Boltzmann's constant. (We will be considering only cases where the gap Δ and the temperature T are constant, so that we can safely suppress the functional dependence on them.) Since q_k is an odd function of ξ_k and $f^o(\varepsilon_k)$ an even one, the charge imbalance $Q^* = 0$ and all the electronic charge resides in the condensate. For a general disequilibrium, both ε_s and Q^* may be nonzero, but overall charge neutrality should still be maintained.[56] Therefore we have (see Fig. 3.1a)

$$Q^* + Q_c\big|_{\varepsilon_s \neq 0} = Q_c\big|_{\varepsilon_s=0}$$

so that

$$Q^* = 2e\sum_k (v_k^2\big|_{\varepsilon_s=0} - v_k^2\big|_{\varepsilon_s\neq 0}) = -2N(0)e\varepsilon_s \qquad (3.8)$$

where N(0) is the normal electronic density of states at the Fermi energy for one spin.

Looking back to the definition of Q^* in Eq. (3.4), we see that it will be affected by a change in either f_k or q_k:

$$\dot{Q}^* = 2\sum_k (q_k \dot{f}_k + f_k \dot{q}_k) \qquad (3.9)$$

AD-A078 441 HARVARD UNIV CAMBRIDGE MA DIV OF APPLIED SCIENCES F/G 20/3
NONEQUILIBRIUM PHENOMENA IN SUPERCONDUCTING PHASE-SLIP CENTERS.(U)
OCT 79 A M KADIN N00014-77-C-0085
UNCLASSIFIED TR-15 NL

2 OF 3
AD A078441

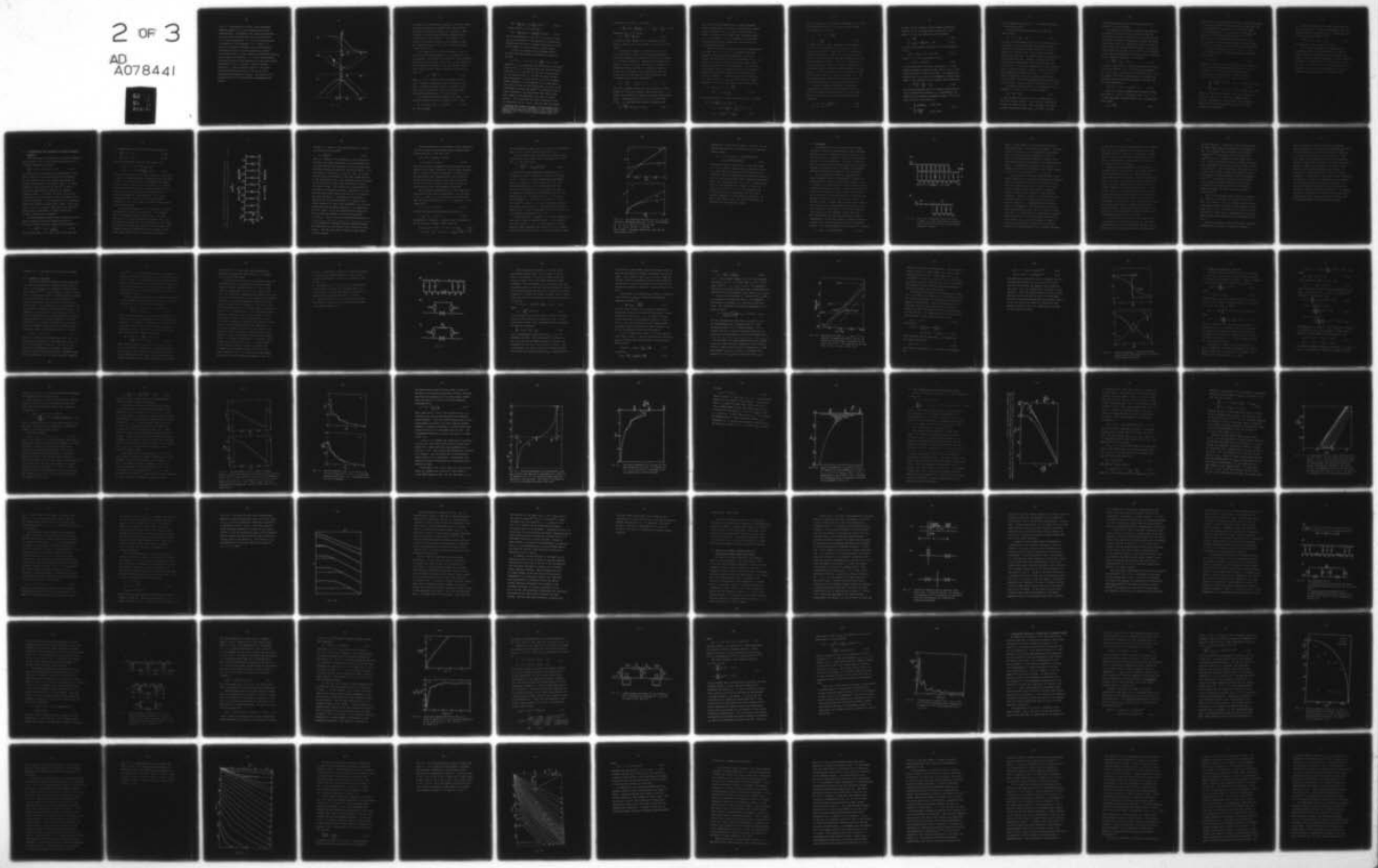

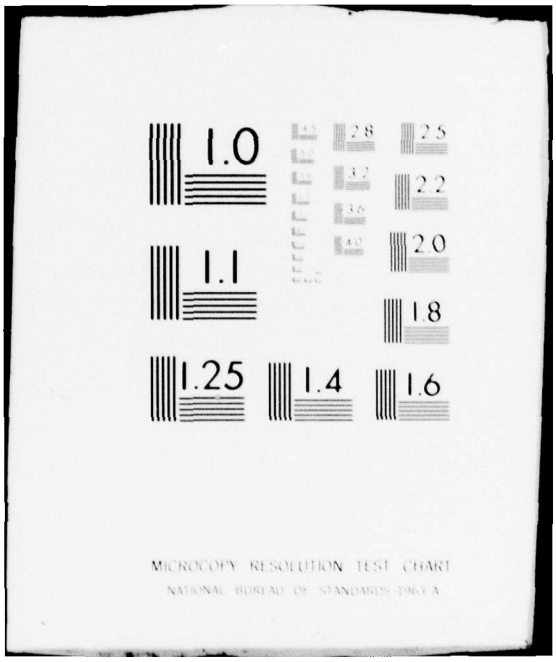
1.0
1.1
1.25
1.4
1.6
2.8
3.2
3.6
4.0
2.5
2.2
2.0
1.8
MICROCOPY RESOLUTION TEST CHART
NATIONAL BUREAU OF STANDARDS 1963 A

Fig. 3.1 The effects of a shift in the condensate chemical potential ε_s on the condensate and on the quasiparticles. The dashed lines indicate equilibrium, the solid lines disequilibrium, and the dotted line in (c) local equilibrium. a) v_k^2 gives the occupation of electrons in the condensate. b) A shift in ε_s shifts the excitation spectrum, but in the absence of inelastic collisions, a given quasiparticle remains at the same value of ε_k but changes its excitation energy E_k and its effective charge q_k. c) If the nonequilibrium quasiparticles can be characterized by a quasi-equilibrium distribution $f^o(\varepsilon_k-\varepsilon_n)$ around a "normal" chemical potential ε_n, this is actually closer to the global equilibrium distribution $f^o(\varepsilon_k)$ than to the local equilibrium distribution $f^o(\varepsilon_k-\varepsilon_s)$. The extent of the disequilibrium in the figures here is exaggerated for clarity.

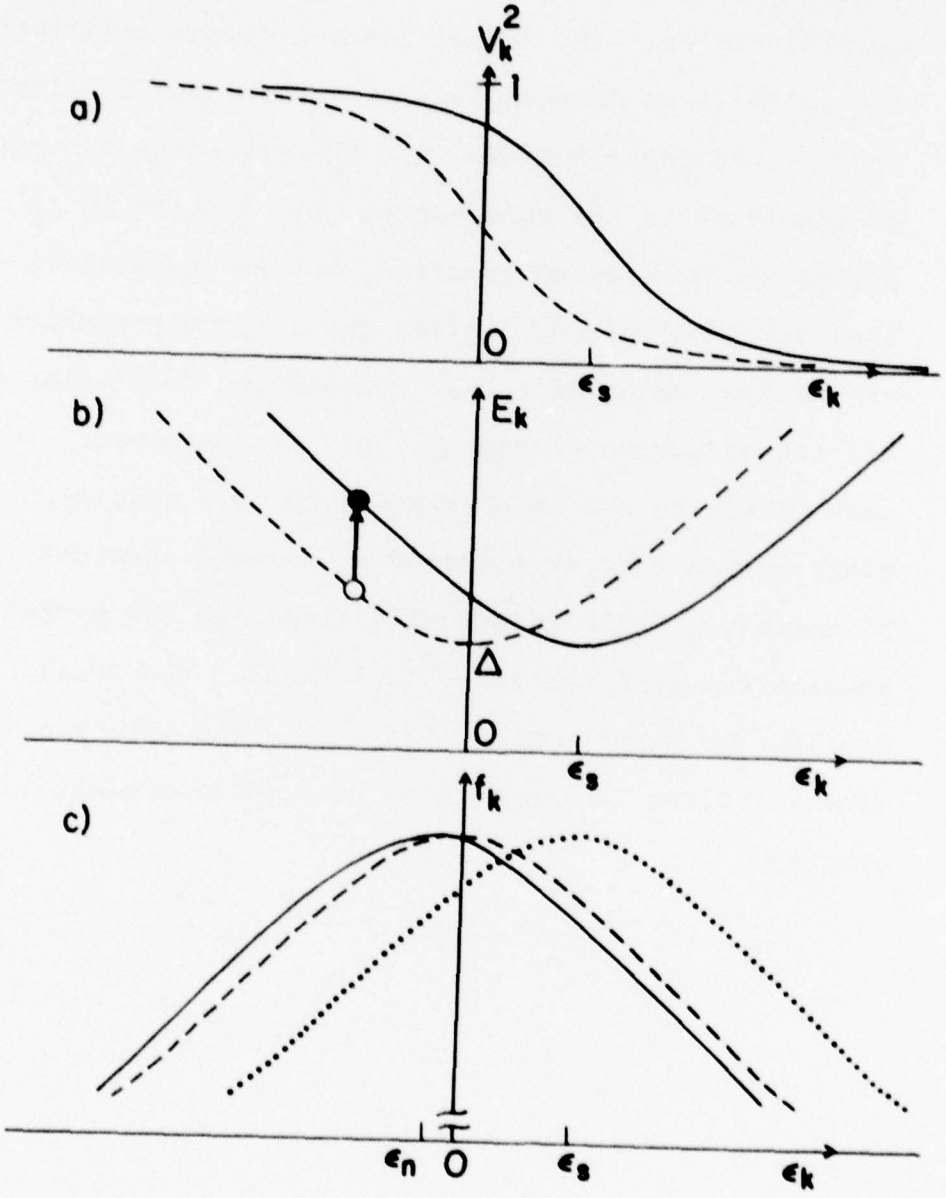
a)
V_k^2
1
0
ϵ_s
ϵ_k
b)
E_k
Δ
0
ϵ_s
ϵ_k
c)
f_k
ϵ_n
0
ϵ_s
ϵ_k

Fig. 3.1

A change in the distribution function f_k can occur either by direct injection of quasiparticles, quasiparticle diffusion from adjacent regions, or collisions. Thus inelastic electron-phonon scattering between states of different q_k will change Q^*. In addition, if ε_s changes, the effective charge q_k will change for <u>all</u> the quasiparticles (see Fig. 3.1b), which has an even greater effect on Q^*.

In a steady-state injection experiment, such as those by Clarke and colleagues,[13] ε_s and hence the q_k's are constant. The resulting steady-state charge imbalance will then be proportional to the time τ_{Q^*} which characterizes relaxation by changes in the distribution function alone, which has been shown to take the following form near T_c:[12]

$$\tau_{Q^*} = \frac{4k_BT}{\pi\Delta}\,\tau_E \qquad (3.10)$$

where τ_E is the inelastic electron-phonon collision time. The k_BT/Δ enhancement factor reflects the fact that a transition between states of different q_k can occur only if either the initial or the final state lies within approximately Δ of the gap edge.

In a pulsed experiment, however, the change in the effective charge q_k plays an essential role. Since

$$\dot{q}_k = e\dot{\varepsilon}_s \frac{\partial}{\partial\varepsilon_s}(\xi_k/E_k) = -e\dot{\varepsilon}_s\Delta^2/E_k^3 \qquad (3.11)$$

Eq. (3.9) becomes

$$\dot{Q}^* = 2\sum_k q_k \dot{f}_k - 2e\dot{\varepsilon}_s \sum_k f_k \Delta^2 / E_k^3 \quad , \qquad (3.12)$$

so that using Eq. (3.8) we obtain

$$\dot{Q}^* = [2\sum_k q_k \dot{f}_k]/[1 - \frac{1}{N(0)} \sum_k f_k \Delta^2 / E_k^3] \quad . \qquad (3.13)$$

Since the denominator in Eq. (3.13) is positive (for $f_k \leq \frac{1}{2}$) the response of the superfluid in maintaining electroneutrality acts to enhance the change in Q^* due to the change in the distribution function alone.

In order to evaluate this enhancement factor,* we write the nonequilibrium distribution function in the form

$$f_k = f^o(\varepsilon_k - \varepsilon_s) + \delta f_k \simeq \frac{1}{2} - \frac{E_k}{4k_B T} + \delta f_k \qquad (3.14)$$

where $f^o(\varepsilon_k - \varepsilon_s)$ represents the equilibrium distribution function [Eq. (3.7)] centered about the shifted chemical potential ε_s, and the form on the right is appropriate for low energies near T_c. We take the small deviation from equilibrium δf_k to be odd in ξ_k so as to produce a charge imbalance. A distribution of this form implies that the gap Δ has its equilibrium value, so that in the terminology of Schmid and Schön,[12] the disequilibrium is purely transverse, the longitudinal mode (which deals with changes in the magnitude of the gap) not being excited. If we substitute the above distribution into the denominator of Eq. (3.13), and note that δf_k cancels

---

* Although the present treatment is restricted to the regime close to T_c, the denominator in Eq. (3.13) can be evaluated more generally, in terms of the integral Z(T) defined in ref. 14, to yield an enhancement factor of $1/[1-Z(T)]$.

out since it is odd in ξ_k we obtain

$$1 - \int_{-\infty}^{\infty} d\varepsilon_k \left(\frac{1}{2} - \frac{E_k}{4k_BT}\right)\frac{\Delta^2}{E_k^3} = 1 - \left(1 - \frac{\pi\Delta}{4k_BT}\right) = \frac{\pi\Delta}{4k_BT} \quad . \quad (3.15)$$

Therefore, Eq. (3.13) becomes

$$\dot{Q}^* = \frac{4k_BT}{\pi\Delta}\left[2\sum_k q_k \dot{f}_k\right] \quad (3.16)$$

so that the total change in Q^* is enhanced over the explicit change (due to the changes in f_k) by the factor $4k_BT/\pi\Delta$.

In general the factor in brackets in Eq. (3.16) will be the sum of terms for the various mechanisms by which the quasiparticle distribution function can change, e.g. inelastic scattering, quasiparticle diffusion and tunnel injection. For the simplest case, relaxation of a homogeneous charge imbalance by inelastic scattering, we can use a relaxation time approximation with the single time τ_{Q^*} (although the actual relaxation time is expected to be energy dependent[40]):

$$\dot{f}_k = -\frac{\delta f_k}{\tau_{Q^*}} = -\frac{1}{\tau_{Q^*}}\left[f_k - f^o(\varepsilon_k - \varepsilon_s)\right] \quad . \quad (3.17)$$

Note that τ_{Q^*}characterizes the rate at which f_k relaxes toward the "local equilibrium" distribution $f^o(\varepsilon_k - \varepsilon_s)$, rather than towards the "global equilibrium" distribution $f^o(\varepsilon_k)$. Substituting into Eq. (3.16), we find that $f^o(\varepsilon_k - \varepsilon_s)$ contributes zero charge imbalance, and

$$\dot{Q}^* = \frac{4k_BT}{\pi\Delta}\left[-Q^*/\tau_{Q^*}\right] = -Q^*/\tau_E \quad (3.18)$$

Thus a time-resolved observation of charge imbalance decay following pulse injection of quasiparticles should yield a relaxation time τ_E, rather than the value τ_{Q^*} which is appropriate for steady-state experiments where ε_s is held constant. To our knowledge this prediction has not been previously emphasized, and remains to be verified experimentally.

Thus far the only assumptions about the disequilibrium have been that it is odd in ξ_k (transverse) and small compared to the equilibrium populations. Let us go further and assume that f_k may be described by $f^o(\varepsilon_k - \varepsilon_n)$, where ε_n is different from ε_s and can be viewed as the chemical potential of the quasiparticles. In effect, we are assuming that the quasiparticles come to equilibrium among themselves before they come to equilibrium with the pair condensate. Expanding the effective charge q_k in a Taylor series in $\varepsilon_s - \varepsilon_n$ (which we take to be small compared to Δ) and dropping higher order terms, we have

$$q_k = q_k\Big|_{\varepsilon_s=\varepsilon_n} + (\varepsilon_s-\varepsilon_n)\left.\frac{\partial q_k}{\partial \varepsilon_s}\right|_{\varepsilon_n}$$

$$= q_k\Big|_{\varepsilon_n} - (\varepsilon_s-\varepsilon_n)\left.\frac{\Delta^2}{E_k^3}\right|_{\varepsilon_n} \qquad (3.19)$$

If we substitute this into the evaluation of Q^*, we obtain

$$Q^* = 2N(0)\int_{-\infty}^{\infty} d\varepsilon_k \; q_k \; f^o(\varepsilon_k-\varepsilon_s)$$

$$= -(\varepsilon_s - \varepsilon_n)2N(0)\int_{-\infty}^{\infty} d\varepsilon_k \left.\frac{\Delta^2}{E_k^3}\right|_{\varepsilon_n} f^o(\varepsilon_k - \varepsilon_n)$$

$$= -(\varepsilon_s - \varepsilon_n)2N(0)\left(1 - \frac{\pi\Delta}{4k_BT}\right) \qquad (3.20)$$

where the integral is the same one evaluated in Eq. (3.15). If we compare this to Eq. (3.8) derived earlier from electroneutrality, we have

$$\varepsilon_s = (\varepsilon_s - \varepsilon_n)\left(1 - \frac{\pi\Delta}{4k_BT}\right)$$

or

$$\varepsilon_n = -\varepsilon_s \frac{\pi\Delta}{4k_BT} \tag{3.21}$$

to lowest order in Δ/k_BT. Therefore, as illustrated in Fig. 3.1c, the distribution $f_k = f^o(\varepsilon_k-\varepsilon_n)$ is much closer (by the factor $\pi\Delta/4k_BT$) to $f^o(\varepsilon_k)$, corresponding to global equilibrium, than to $f^o(\varepsilon_k-\varepsilon_s)$, which corresponds to local equilibrium with the condensate about the shifted chemical potential. This is a reflection of the point made earlier, that near T_c small changes in the distribution function produced enhanced changes in Q^* and hence ε_s. In what follows, since we are retaining terms only of leading order in Δ/k_BT, we will take $\varepsilon_n \approx 0$. This approximation should remain valid even when f_k cannot strictly be expressed in terms of a Fermi function.

In order to deal with spatially inhomogeneous disequilibria, we define electrochemical potentials μ_s for the superfluid condensate and μ_n for the quasiparticles, as the sum of the chemical and electrical potentials:

$$\mu_s = \varepsilon_s + e\phi = \frac{-Q^*}{2N(0)e} + e\phi \tag{3.22}$$

$$\mu_n = \varepsilon_n + e\phi \approx e\phi \tag{3.23}$$

We then use the standard Ginzburg-Landau expressions relating μ_s and the supercurrent density $\vec{J}_s$ to the phase θ of the superconducting order parameter,

$$\mu_s = -\tfrac{1}{2}\hbar\dot{\theta} \tag{3.24}$$

$$\vec{J}_s = n_s e\vec{v}_s = \frac{n_s e}{2m}\,(\hbar\vec{\nabla}\theta - 2e\vec{A}) \tag{3.25}$$

to obtain the following relation for the time evolution of $\vec{J}_s$:

$$\tau_o\dot{\vec{J}}_s = -\frac{\sigma}{e}\vec{\nabla}\mu_s - \sigma\dot{\vec{A}} = \sigma\vec{E} + D\vec{\nabla}Q^* \tag{3.26}$$

Here $\vec{E} = -\vec{\nabla}\phi - \dot{\vec{A}}$ is the electric field,

$$\sigma = ne^2\tau/m = 2N(0)e^2D \tag{3.27}$$

is the normal-state electronic conductivity, τ is the momentum-transport relaxation time, and $D = v_F^2\tau/3$ is the normal electronic diffusion constant. The supercurrent response time τ_o is one of the fundamental characteristic times in our treatment of the problem, and is defined by

$$\tau_o \equiv \frac{4\pi\lambda^2\sigma}{c^2} = \frac{m\sigma}{n_s e^2} = \frac{n}{n_s}\tau \tag{3.28}$$

This can be evaluated using the standard normalizations for the superelectron density n_s, or equivalently the formulas for the magnetic penetration depth λ,[29] in the clean and dirty limits near T_c:

$$\tau_o \rightarrow \begin{cases} \dfrac{\tau}{2(1-T/T_c)} & \text{Clean limit} \\ \dfrac{2k_B T_c \hbar}{\pi\Delta^2} & \text{Dirty limit} \end{cases} \tag{3.29}$$

We have assumed here that $n_s \propto \Delta^2$ is constant and holds its equilibrium value.

For the normal current density $\vec{J}_n$ we use the usual relation

$$\vec{J}_n = \sigma\vec{E} \simeq -\frac{\sigma}{e}\vec{\nabla}\mu_n - \sigma\dot{\vec{A}} \qquad (3.30)$$

but with the understanding that it is a good approximation only near T_c. This is because superconducting quasiparticles are not simply either electrons or holes, as they are in a normal metal, nor even particles with a well-defined charge q_k, but rather coherent superpositions of electrons and holes. However, quasiparticles with energies much greater than Δ (which form the majority in the limit $T \to T_c$) can be considered, at least operationally, as either electrons or holes. Pethick and Smith[24] have compared the normal current $\vec{J}_n = \vec{J} - \vec{J}_s$ with the current carried by the flow of quasiparticles (which they call $\vec{J}_n{}^Q$), and have demonstrated that the difference goes to zero as Δ/k_BT, as do the corrections to Eq. (3.30).

The physical significance of τ_o becomes clear if we subtract Eq. (3.30) from Eq. (3.26) to obtain

$$\tau_o\dot{\vec{J}}_s - \vec{J}_n = D\vec{\nabla}Q^* \quad . \qquad (3.31)$$

In the equilibrium case where $Q^*=0$, a sudden change in the total current density $\vec{J} = \vec{J}_s + \vec{J}_n$ will initially be carried as normal current. This will decay into supercurrent exponentially with time τ_o, so that τ_o is the

equilibrium response time of the supercurrent to a change in the total current.

The presence of $\vec{J}_n$ means that charge can leave the quasiparticle system in a given region of space not only through inelastic scattering, but also through the net inflow or outflow of quasiparticle current as determined by the term $\vec{\nabla}\cdot\vec{J}_n$. Because this acts to produce a direct change in the distribution function, it enters as a term inside the brackets in Eq. (3.16), and is subject to the same enhancement factor as that due to to inelastic charge imbalance relaxation. We thus have

$$\dot{Q}^* = \frac{4k_BT}{\pi\Delta}\left[-\frac{Q^*}{\tau_{Q^*}} - \vec{\nabla}\cdot\vec{J}_n\right] . \qquad (3.32)$$

Similarly a quasiparticle injection term would also enter inside the brackets. Now, if we take the divergence of Eq. (3.31), add τ_o times the time derivative of Eq. (3.32), and assume $\vec{\nabla}\cdot\vec{J}=0$ from electroneutrality, we obtain the following partial differential equation involving only the charge imbalance Q^*:

$$D\tau_{Q^*}\nabla^2 Q^* = \tau_o\tau_E\ddot{Q}^* + (\tau_o+\tau_E)\dot{Q}^* + Q^* \qquad (3.33)$$

This is the charge imbalance wave equation we have been seeking. In the low frequency limit $\omega<<\tau_o^{-1}$, τ_E^{-1} it describes charge imbalance decay with a characteristic decay length

$$\Lambda_{Q^*} = \sqrt{D\tau_{Q^*}} \quad . \qquad (3.34)$$

This length, the quasiparticle diffusion length corresponding to the branch imbalance relaxation time τ_{Q^*}, has been used to characterize the penetration of an electric field into a superconductor in the presence of a current flow through a normal-superconducting boundary.[10,17,18] From here on, we will denote this length simply by Λ, but it should be clearly distinguished from the related length $\sqrt{D\tau_E}$, for which the same notation was used by SBT.

In the high frequency limit ($\omega << \tau_E^{-1}, \tau_o^{-1}$), Eq. (3.33) describes waves of charge imbalance, propagating with velocity

$$v = \Lambda/\sqrt{\tau_o \tau_E} \tag{3.35}$$

Physically, this is the same phenomenon as the propagating collective mode observed experimentally by Carlson and Goldman[23] in the tunneling fluctuation spectra of superconducting films below T_c. We can evaluate Eq. (3.35) by substituting in for τ_o from Eq. (3.29):

$$v \to \begin{cases} v_F\left[\frac{8k_BT}{3\pi\Delta}\left(1-\frac{T}{T_c}\right)\right]^{\frac{1}{2}} \simeq 0.53\, v_F \left(1-\frac{T}{T_c}\right)^{\frac{1}{2}}, & \text{Clean limit} \\ (2D\Delta/\hbar)^{\frac{1}{2}} \simeq 0.61\, v_F \left(\ell/\xi_o\right)^{\frac{1}{2}} \left(1-\frac{T}{T_c}\right)^{\frac{1}{4}}, & \text{Dirty limit} \end{cases} \tag{3.36}$$

where v_F is the Fermi velocity, $\ell = v_F\tau$ is the mean free path, and $\xi_o = \hbar v_F/\pi\Delta(0)$ is the BCS coherence length. The above expressions for the velocity are identical to those derived for this propagating mode within other theoretical frameworks.[22]

For the more general case where neither the high nor the low frequency limits is appropriate, Eq. (3.33) describes damped, dispersive waves of charge imbalance with the dispersion relation[57,58]

$$-\Lambda^2 k^2 = (1 + i\omega\tau_o)(1 + i\omega\tau_E) \qquad (3.37)$$

for waves which vary as $\exp[i(\omega t - \vec{k}\cdot\vec{r})]$.

Thus, the two phenomena of dc electric field penetration into a superconductor and the high frequency propagating collective mode are both special cases of the more general phenomenon of charge imbalance dynamics in a superconductor, governed by Eqs. (3.31) to (3.33). We will show in the next section that these equations in turn can be represented by a physically transparent transmission-line equivalent circuit.

3.3 A Transmission-Line Equivalent for Charge Imbalance Dynamics

When expressed in one dimension, the charge imbalance wave equation (3.33) is well known historically as the telegraph equation, in the form

$$\frac{\partial^2 E}{\partial x^2} = LC\,\ddot{E} + (RC + GL)\,\dot{E} + RG\,E \quad . \qquad (3.38)$$

This describes the propagation of electromagnetic waves down a cable with a series inductance and resistance per unit length L and R, and a shunt capacitance and leakage conductance per unit length C and G. An early treatment of the problem was by Kelvin[59] in 1855 to explain the wave-carrying properties of submarine telegraph cables. In general, the waves are not only attenuated, but are dispersed as well; the phase velocity depends on frequency. Since dispersion is an undesirable feature when sending a signal down a cable, it was noted early on that in the special case that RC=GL, the wave, although still attenuated, is dispersionless with velocity $1/\sqrt{LC}$ for all frequencies.

The correspondence between these telegraph waves and charge imbalance waves can be made more explicit. Defining the gauge-invariant nonequilibrium potential Φ

$$\Phi = \phi + \frac{\hbar}{2e}\dot{\theta} = -\varepsilon_s/e = \frac{\Omega^*}{2N(0)e^2} \quad , \qquad (3.39)$$

we can rewrite Eqs. (3.31) and (3.32) in the form (for

a one-dimensional wire with cross-sectional area A):

$$\frac{\partial I_n}{\partial x} + G\Phi + C\dot{\Phi} = 0 \qquad (3.40)$$

$$\frac{\partial \Phi}{\partial x} + RI_n - L\dot{I}_s = 0 \qquad (3.41)$$

where the parameters (each per unit length) are:

$$R = \frac{1}{\sigma A} \;\; ; \;\; G = 2N(0)e^2 A/\tau_{Q^*} = \frac{\sigma A}{\Lambda^2}$$

$$L = \frac{\tau_o}{\sigma A} \;\; ; \;\; C = 2N(0)e^2 A \frac{\pi\Delta}{4k_B T} = \frac{\sigma A}{\Lambda^2}\tau_E \qquad (3.42)$$

This system of equations, strictly valid only in the limit $\Delta << k_B T$, is represented by the transmission-line equivalent in Fig. 3.2. The resistive line represents the channel for the normal current I_n and its voltage μ_n/e, and the inductive line represents the condensate channel with I_s and μ_s/e (we can ignore the vector potential $\vec{A}$ for a quasi-one-dimensional superconductor). The voltage between the lines $(\mu_n - \mu_s)/e$ is the nonequilibrium potential Φ. Eqs. (3.40) and (3.41) then follow directly from Kirchoff's laws.

The circuit parameters R, L, C, and G have a simple and appealing physical interpretation. The relaxation of Φ is governed by the time constant $\tau_E = C/G$, while the ratio L/R is the characteristic response time τ_o for the supercurrent when $\Phi=0$. The resistance per unit length R is simply the normal resistance per unit length of the filament, while the inductance per unit length L is the usual London theory kinetic inductance of the super-

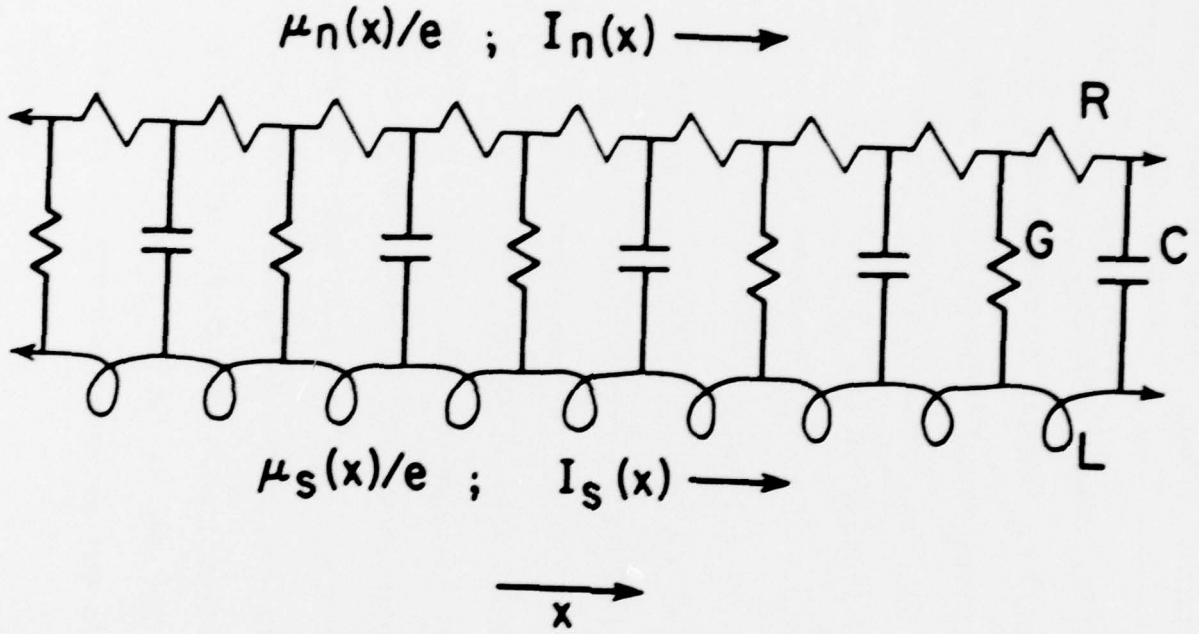

Fig. 3.2 Transmission-line equivalent of the charge imbalance wave equation. The electrical parameters per unit length are given by Eq. (3.42)

current.* To assist in the interpretation of C and G, we introduce the quantity[24]

$$Q_n = \frac{\pi\Delta}{4k_BT} Q^* \qquad (3.43)$$

which is a measure of the departure of the distribution function from global equilibrium, as distinguished from Q^*, which measures the departure from local equilibrium. Neglecting conversion processes, we obtain from Eq. (3.32) the continuity equation $\dot{Q}_n = -dJ_n/dx$. Thus, Q_n is the quantity which is analogous to the "free charge density" in the transmission line. The capacitance per unit length C is then equal to Q_nA/Φ, which differs from Q^*A/Φ by the factor $\pi\Delta/4k_BT$. This factor can be interpreted as an effective "dielectric constant" (although it is less than one rather than greater than one as is the case for the usual dielectric), representing the fact that a change of the "free charge density" Q_n induces a much larger change of Q^*, due to the adjustment of ε_s required to maintain overall charge neutrality. The conductance per unit length G gives the proportionality between the rate at which Q_nA changes by conversion processes ($= -Q^*A/\tau_{Q^*} = -Q_nA/\tau_E$) and the nonequilibrium potential Φ.

---

* The geometrical inductance remains undefined because the return path for the current is not included in this circuit. For our usual case of constant total current it can be ignored.

The significance of the equivalent circuit parameters can also be seen from the energy balance equation which follows from Eqs. (3.40) and (3.41):

$$I_n^2 R + \Phi^2 G + \frac{\partial}{\partial t}[\tfrac{1}{2}LI_s^2 + \tfrac{1}{2}C\Phi^2]$$

$$= -\frac{\partial}{\partial x}\,(I_n\mu_n/e + I_s\mu_s/e) \qquad (3.44)$$

The first two terms represent energy dissipated by Joule heating in the normal resistance, and by charge imbalance decay. Energy is stored "inductively" in the motion of the supercurrent and "capacitatively" in the field of the nonequilibrium potential, and can be carried into or out of a region of space by the flow of normal or supercurrent at their corresponding potentials.

The propagation characteristics of the transmission line depend on the relative magnitudes of the two times τ_o and τ_E. When $\tau_o=\tau_E$, we have the special dispersionless case mentioned earlier ($L/R = C/G$), where Eq. (3.37) simplifies to

$$k = k_R + ik_I = \omega\frac{\tau_o}{\Lambda} + \frac{i}{\Lambda} \qquad (3.45)$$

so that the phase velocity and decay length are

$$v = \frac{\omega}{k_R} = \frac{\Lambda}{\tau_o} \quad ; \quad k_I^{-1} = \Lambda\ , \qquad (3.46)$$

independent of frequency. Otherwise they are bounded by the low and high frequency limits given by

$$\Lambda/[(\tau_o+\tau_E)/2] = v(0) < v < v(\infty) = \Lambda/\sqrt{\tau_o\tau_E} \qquad (3.47)$$

$$\Lambda = k_I^{-1}(0) > k_I^{-1} > k_I^{-1}(\infty) = \Lambda\sqrt{\tau_o\tau_E}/[\frac{\tau_o+\tau_E}{2}]\,. \qquad (3.48)$$

For illustration we show in Fig. 3.3 the real and imaginary parts of $k(\omega)$ for two values of the ratio τ_E/τ_o.

We can compare these characteristic times for some representative superconductors by evaluating Eq. (3.29) for τ_o in the dirty limit:

$$\tau_o = \frac{2k_B T_c \hbar}{\pi \Delta^2} = \frac{5.2 \times 10^{-13} \text{ sec}}{(T_c - T) \quad [K]} \tag{3.49}$$

(τ_o here has the same temperature dependence as $\tau_{GL} = \pi\hbar/[8k_B(T_c-T)]$ but is smaller by a factor of $\pi^4/14\zeta(3) = 5.79$). Thus for a typical experimental temperature about 50 mK from T_c, τ_o is of order 10^{-11} sec. The electron-phonon time τ_E is a normal-metal property and hence is nonsingular at T_c, so that we can take it as essentially temperature-indendependent for any given material near T_c. It varies from 2.3×10^{-11} sec in Pb [40] through 1.5×10^{-10} sec in Sn [36] to 1.3×10^{-8} sec in Al,[41] so that $\tau_E > \tau_o$ is the more usual relationship except very close to T_c. The dispersion relations shown in Fig. 3a and 3b correspond to Sn and Al respectively at reduced temperature $T/T_c = 0.99$.

The characteristic impedance $Z(\omega)$ of the transmission line can be found by standard methods. If we constrain the total current $I = I_s + I_n$ to be constant in time, then the charge imbalance wave equation (3.33) is obeyed not only by Φ, but also by I_n. If we now consider a wave

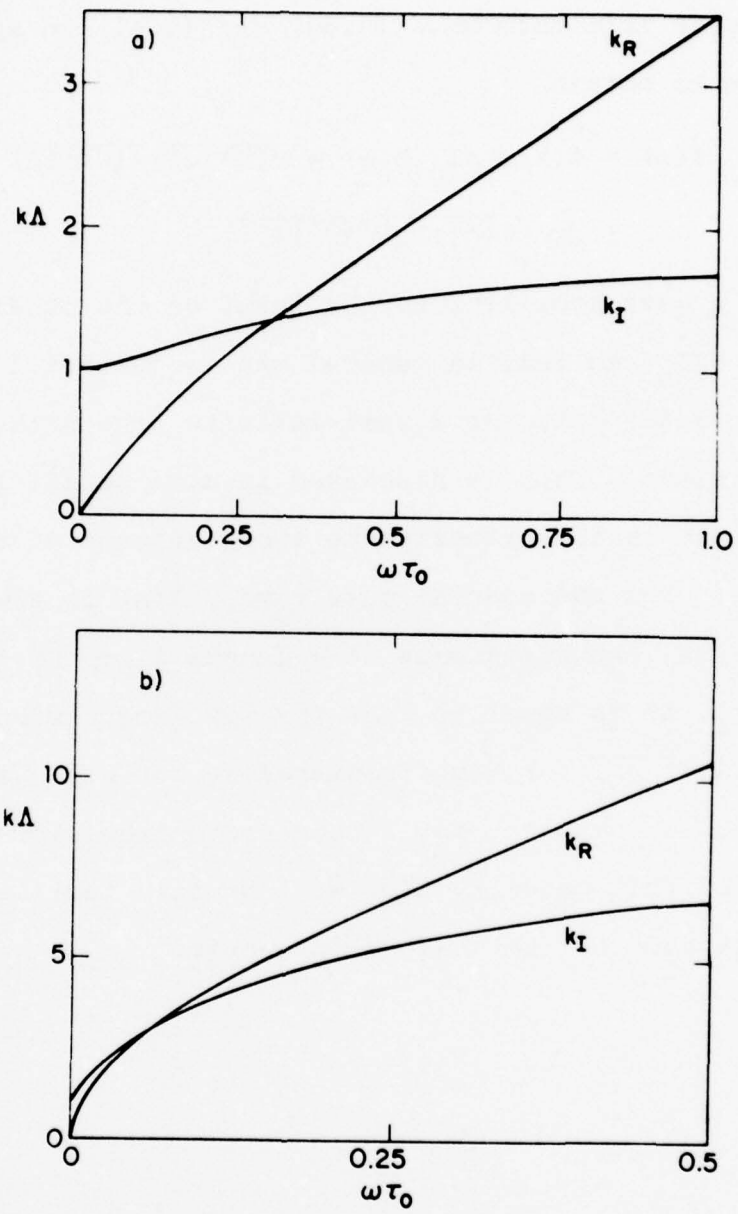

Fig. 3.3 The dispersion relation $k(\omega) = k_R + k_I$ for the charge imbalance waves [Eq. (3.37)] for the cases
a) $\tau_E = 11\ \tau_o$ (Sn at $T = 0.99\ T_c$), and
b) $\tau_E = 280\ \tau_o$ (Al at $T = 0.99\ T_c$).
For a given , the phase velocity is ω/k_R and the decay length is k_I^{-1}.

propagating to the right as $\exp[i\omega t - ik(\omega)x]$, we can Fourier transform Eqs. (3.40) and (3.41) in space and time to obtain

$$Z(\omega) = \tilde{\Phi}(k,\omega)/\tilde{I}_n(k,\omega) = \sqrt{(R+i\omega L)/(G+i\omega C)}$$

$$= \frac{\Lambda}{\sigma A}\sqrt{(1+i\omega\tau_o)/(1+i\omega\tau_E)} \qquad (3.50)$$

For a wave traveling to the left, on the other hand, $\tilde{\Phi} = -Z\tilde{I}_n$, so that in general one is justified in using Eq. (3.50) only for a semi-infinite line with no reflections. This is discussed in more detail in Appendix III, as is the extension to short lengths of transmission line. For the special case $\tau_o=\tau_E$, $Z(\omega)$ is always equal to $\Lambda/\sigma A$, the resistance of a length Λ of the line. If $\tau_o\neq\tau_E$, it is equal to $\Lambda/\sigma A$ for low frequencies and $(\Lambda/\sigma A)\sqrt{\tau_o/\tau_E}$ for high frequencies, but will have a reactive component for intermediate frequeicies. The use of this quantity $Z(\omega)$ will greatly facilitate our discussion of the phase-slip center.

3.4 Discussion

The transmission-line equivalent which we have developed to describe superconducting charge imbalance dynamics provides a coherent picture in which to view the whole range of phenomena involving a nonequilibrium potential in a superconductor. In order to highlight both its usefulness and its limitations we will briefly consider its applicability to a number of experiments that have already been described in the literature.

As we discussed in Chapter I, the concept of branch imbalance was first introduced[9] to explain the measurements by Clarke[13] of differences between μ_n and μ_s induced in a superconducting film by spatially uniform quasiparticle tunnel injection. Within the regime near T_c where our transmission-line picture is most valid, we can represent the physical processes involved by the equivalent circuit of Fig. 3.4a (cf. Fig. 1.3a). A constant current I tunnels from a normal film through an oxide barrier into a superconducting film below. This current creates "free charge" in the normal channel at a rate $(\dot{Q}_n)_{inj}=I/(\ell A)$, charging up the capacitors. They discharge at the same rate through the leakage conductance G, so that the current I leaves the nonequilibrium region as pure supercurrent in the condensate channel. The induced nonequilibrium potential is therefore

$$\Phi = I/(G\ell) = I\tau_{Q^*}/[2N(0)e^2\ell A] \qquad (3.51)$$

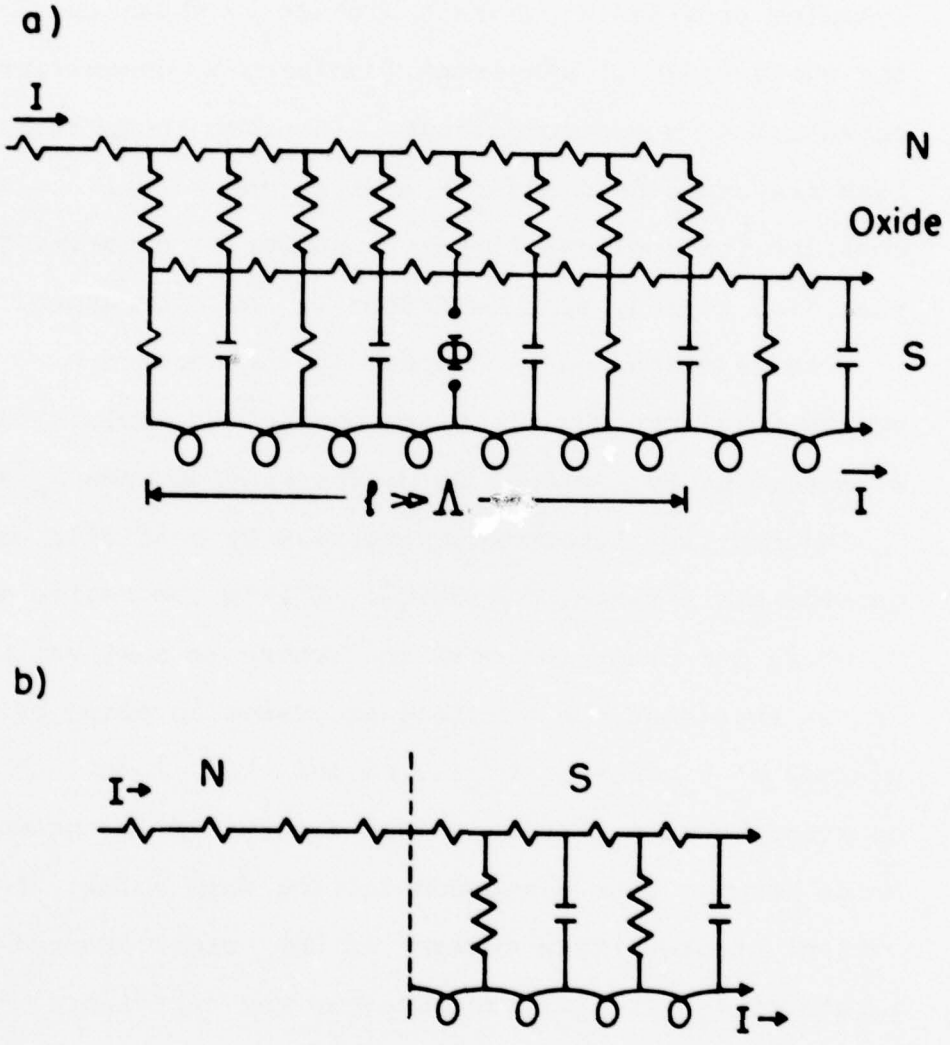

Fig. 3.4 Use of the transmission-line equivalent to model a) uniform quasiparticle injection, and b) current flow through a normal-superconducting boundary.

where ℓ is the length of the nonequilibrium region, much larger than Λ (to minimize edge effects). The form on the right of Eq. (3.51) is essentially the same as that originally derived by Tinkham and Clarke[9] to explain the nonequilibrium potential, measured using superconducting and normal probes in the nonequilibrium region. We reemphasize here that if the current is suddenly turned off, the potential Φ will decay exponentially with a time constant $C/G = \tau_E$, not τ_{Q^*}.

One can also see from this picture why the S and N probes measure their respective electrochemical potentials, within the region near T_c where the picture is valid. The normal detector junction is similar to the normal injector junction, except that there is negligible current passing through (assuming a high-impedance voltmeter). Therefore there is no voltage drop across the oxide barrier, and the potential of the normal probe is equal to μ_n. A superconducting probe may be either a continuation of the superconducting film out of the nonequilibrium region (as it was for the Clarke experiment) or a superconductor-superconductor Josephson tunnel junction (as in the Dolan-Jackel experiment[19]). In the former case, μ_s will be constant in space in a steady-state situation, provided that the critical current of the superconducting film is nowhere exceeded.

In the latter case we have essentially the same condition. There may be a difference in the values of μ_n on the two sides of the S-S junction, so that there is quasiparticle current passing through the barrier, but so long as a counterflow of supercurrent is possible, μ_s will be the same on both sides.

Another important phenomenon in which charge imbalance plays a crucial role is the excess resistance on the superconducting side of a current-carrying superconducting-normal interface. We can represent this (again for T near T_c) by the equivalent circuit in Fig. 3.4b, in which the normal current connects up to the "normal" channel on the superconducting side. Over a length equal to Λ, the current leaks over to the condensate line by charge imbalance decay, and the excess resistance is the normal resistance of the length Λ. Furthermore, the equivalent circuit gives rather directly the exponentially decaying nonequilibrium potential near the boundary, which as discussed in Chapter I was observed by Yu and Mercereau[16] using small normal and superconducting probes (see Fig. 1.3b).

As in our model for the PSC, the pictures in Fig. 3.4 are strictly valid only very near T_c. For lower temperatures the fact that quasiparticles near the gap have both electron-like and hole-like characteristics

becomes important. A fraction of the injected current of order Δ/k_BT_c enters the condensate line directly in Fig. 3.4a, reducing the contribution to the charge imbalance.[9,13] Similarly, electrons with energy $< \Delta$ approaching the N-S boundary from the normal side in Fig. 3.4b are reflected as holes via Andreev reflection, with superconducting pairs to carry the current in the superconductor. This corresponds to modifying Fig. 3.4b so that some fraction $\sim\Delta/k_BT_c$ of the current from the normal metal is injected directly into the condensate line.[37,18] A microscopic analysis which calculates this fraction of current Andreev-reflected at the boundary has been used successfully to explain the observed boundary resistance over a wide range of temperatures.[18]

Within the restricted range in which the pictures are valid, we can use them to consider ac effects as well. For instance, for an ac current, the decay length of the nonequilibrium potential becomes shorter, as was noted in Eq. (3.48). Similarly, an ac injection current localized at a point along a superconducting strip will generate charge imbalance waves which propagate down the strip.

We wish to emphasize that this physically appealing transmission-line picture is exactly equivalent in

physical content to some of the recent generalized two-fluid theories of nonequilibrium superconductors.[24,57] These theories also include only the leading order term in Δ/k_BT and are therefore valid only near T_c. They also ignore all pair-breaking effects of the superflow, and so are restricted to currents well below the critical current. Finally, the discussion is limited to a description of the transverse mode, thus ignoring all other effects which would lead to changes in the gap parameter Δ. Nevertheless, within their range of validity, the theories, and hence the transmission-line equivalent, are expected to contain the essential features of the spatial and temporal dependence of the potentials and currents in nonequilibrium superconductors. Even outside the range of quantitative validity, the same qualitative pictures might well continue to provide a useful guide to the understanding of superconducting dynamics.

CHAPTER FOUR: A NEW MODEL FOR THE PHASE-SLIP CENTER

4.1 Elements of the Model

The current-induced breakdown of superconductivity in a quasi-one-dimensional filament has been shown to occur via the nucleation of spatially-localized phase-slip centers.[1,60,61] We will consider a single isolated PSC (in zero magnetic field), centered about x=0, subject to a dc current bias ($\dot{I}$=0). We will follow SBT[1] in dividing the problem into two parts on two different length scales. The oscillations in the magnitude of the gap, which are necessary for the phase-slip process, are assumed to be restricted to a core region with size $\lesssim \xi$ which is small compared to the length scale Λ characterizing variations in the charge imbalance. We further assume that it is possible to model this core region by a discrete Josephson oscillator of zero length and zero resistance, with a current-phase relation of the form

$$I_s(x=0,t) = I_c f(\Delta\theta(t)) \qquad (4.1)$$

where $\Delta\theta$ is the phase difference across the core, f is some function with period 2π and amplitude 1, and I_c is the critical current of the core. The form of this function is undetermined in our model, although we would not expect the purely sinusoidal dependence since this is appropriate only for weak links small compared

to ξ.[50,31] I_c is to be taken as equal to or slightly smaller than the critical current of the adjacent regions of the filament. Our approximations consistently neglect the pair-breaking effects associated with the presence of near-critical supercurrents in these regions. However, we believe that the essential features of the model are qualitatively correct.

Since Josephson oscillations are driven by differences in the condensate electrochemical potential, we can write the voltage V(t) driving these oscillations as

$$V(t) = \frac{\hbar}{2e}\dot{\Delta\theta} = -[\mu_s(x=0^+,t) - \mu_s(x=0^-,t)]$$
$$= \Phi(0^+,t) - \Phi(0^-,t) \quad , \qquad (4.2)$$

where the condition that μ_n is continuous through the origin follows from our assumption of negligible junction resistance. By symmetry the magnitude of Φ must be equal on the two sides of the origin, and since V(t) is not identically zero the values of Φ on the two sides must have opposite signs. Therefore, we have

$$V(t) = 2\Phi(0^+,t) = 2\int d\omega\, e^{i\omega t}\, \Phi(0^+,\omega)$$
$$= 2\int d\omega\, e^{i\omega t}\, Z(\omega)\, I_n(0,\omega) \quad , \qquad (4.3)$$

where the expression in terms of $Z(\omega)$ as in Eq. (3.50) can be justified by regarding the Josephson oscillator as a source of waves propagating away from the origin. We are assuming here that there is not another PSC or a reflective discontinuity in the transmission line nearby

on the scale of Λ, since then waves would also be propagating towards the origin and Eq. (3.50) would not be directly applicable.

The above physical picture is equivalent within our transmission-line representation to placing an ideal Josephson element characterized by Eq. (4.1) in the inductive (condensate) line at x=0, as shown in Fig. 4.1a. As in standard transmission-line theory, the effect of the semi-infinite line on either side of the Josephson oscillator can also be obtained by replacing the line with its characteristic impedance $Z(\omega)$ as in Fig. 4.1b. The impedance shunting the Josephson element is then $2Z(\omega)$, and Eq. (4.3) follows directly. For the current-biased case being considered here, all the current far from the Josephson element flows as supercurrent. In Fig. 4.1b, this is modeled by connecting the external current source to the condensate side of the impedance $Z(\omega)$. [In the more general case of an ac total current, the current far from the Josephson element would be split between I_s and I_n in accordance with the ratio between R and $i\omega L$, so that the modified Fig. 4.1b would include connections to both sides of $Z(\omega)$. A simple generalization allows us also to consider cases where the resistance of the junction region itself R_J is not small compared to $Z(\omega)$, e.g. for small in-line tunnel junctions, as in the simplified schematic in Fig. 4c.]

Fig. 4.1 Equivalent circuits for a phase-slip center.
a) The ideal Josephson element is located on the inductive (condensate) line of the transmission line of Fig. 3.2.
b) The equivalent of (a) as far as the currents and potentials at the center are concerned, where $Z(\omega)$ is the complex frequency-dependent characteristic impedance of the transmission line [Eq. (3.50)].
c) A generalization of (b) to allow for cases where the intrinsic resistance R_J of the Josephson element is not small compared to $Z(\omega)$.

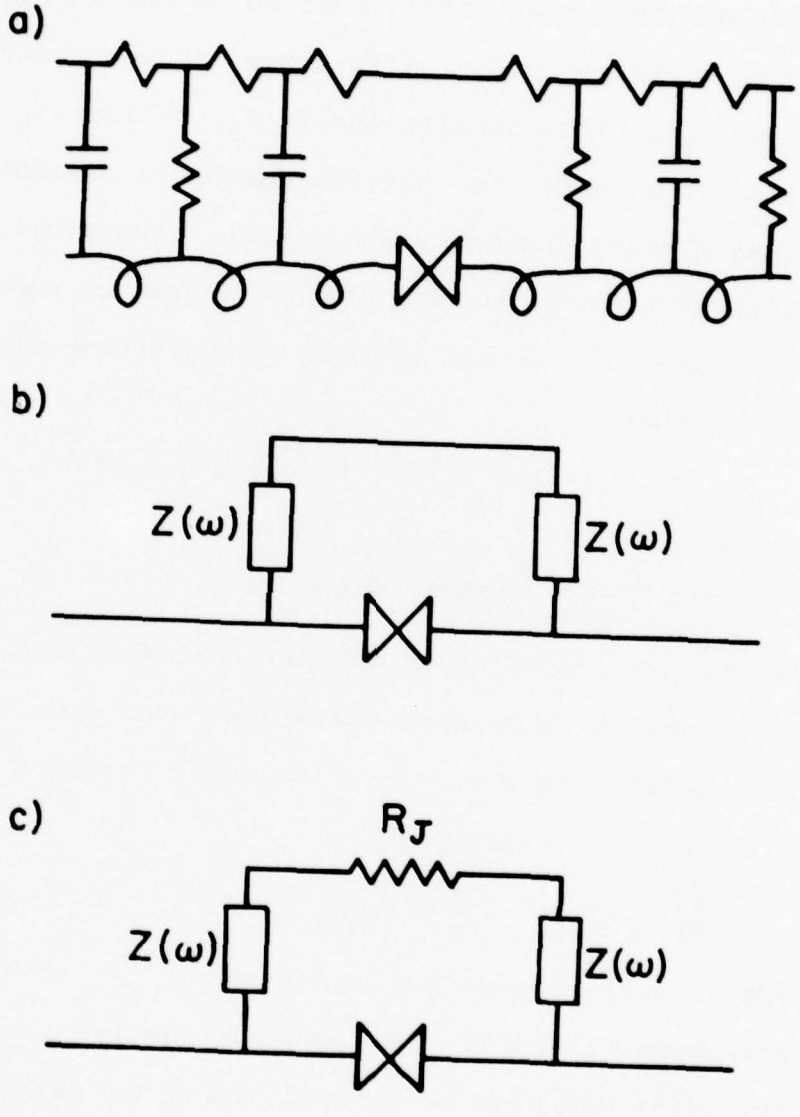

Fig. 4.1

The high-voltage dc behavior of the PSC takes a particularly simple form. At the center of the PSC most of the current $I>>I_c$ must be normal current I_n, which in terms of Fig. 4.1b flows through the shunt impedance. The oscillations in I_n of order I_c are then relatively small, so that the Josephson element is subject to an almost constant voltage bias. Therefore the phase difference $\Delta\theta$ across the element increases nearly linearly with time, and we can express the current-voltage relation in the form

$$\bar{V} = 2Z(0)[I - \overline{I_s(0,t)}] = \frac{2\Lambda}{\sigma A}(I - I_c\langle f\rangle) \qquad (4.4)$$

where

$$\langle f\rangle \equiv \frac{1}{2\pi}\int_0^{2\pi} f(\Delta\theta)\,d(\Delta\theta) \qquad (4.5)$$

is the average value of the periodic function f and the horizontal bars represent averages over time. In the high-voltage regime, then, the model predicts a constant differential resistance

$$\frac{d\bar{V}}{dI} = 2Z(0) = \frac{2\Lambda}{\sigma A} \equiv R_{eff} \qquad (4.6)$$

and an extrapolated excess current $I_{ex} = \langle f\rangle I_c$, in agreement with SBT. The high-voltage I-$\bar{V}$ relation of Eq. (4.4) can also be derived simply by replacing the impedances $Z(\omega)$ in Fig. 4.1b by their dc limits. This is equivalent to a simple resistively shunted junction (RSJ) model with shunt resistance R_{eff}, although here we

are allowing a more general supercurrent-phase relation that the sinusoidal one usually associated with the RSJ model. Note, however, that R_{eff} of the PSC is not the intrinsic junction resistance, which we have assumed to be negligible, but the resistance of the nonequilibrium region which extends a distance Λ on either side of the core.

This effective resistance R_{eff} suggests a characteristic voltage $V_c=I_cR_{eff}$, at which the fundamental Josephson frequency is

$$\omega_c \equiv \frac{2e}{\hbar} I_c R_{eff} = \frac{4eI_c\Lambda}{\hbar\sigma A} \qquad (4.7)$$

For much lower voltages, the Josephson oscillations become much more pulse-like and are dominated by higher harmonics of $2eV/\hbar$ up to $\sim \omega_c$. For larger voltages, on the other hand, the Josephson frequency is larger than ω_c, but the oscillations in this regime become negligibly small perturbations of the dc average, and do not significantly affect the PSC behavior.

It is of interest to compare ω_c^{-1} to the characteristic times τ_o and τ_E. This is facilitated by expressing R_{eff} in terms of the Ginzburg-Landau critical current of the strip[52]

$$I_c(\text{strip}) = An_s ev_c = \frac{\sigma A}{2e\tau_o} \frac{2}{3} \frac{\hbar}{\sqrt{3}\xi} \quad , \qquad (4.8)$$

in the form

$$R_{eff} = \frac{\hbar}{2e\tau_o} \frac{1}{I_c(\text{strip})} \frac{4\Lambda}{3\sqrt{3}\xi} \quad , \qquad (4.9)$$

so that

$$\omega_c\tau_o = \frac{4}{3\sqrt{3}} \frac{\Lambda}{\xi} \frac{I_c}{I_c(\text{strip})} \quad . \tag{4.10}$$

If $\Lambda >> \xi$, as our model assumes, and I_c is only slightly less than $I_c(\text{strip})$, it follows that $\omega_c\tau_o >> 1$.* In the usual regime $\tau_E > \tau_o$, $\omega_c\tau_E >> 1$ as well. In subsequent sections we will make considerable use of approximations involving this "high-frequency limit" where $\omega_c\tau_o$, $\omega_c\tau_E >> 1$.

In Fig. 4.2 we show how ω_c^{-1} compares with τ_o and τ_E as a function of temperature near T_c, for parameters appropriate for aluminum, tin, and lead in the dirty limit. The temperature and material dependence of ω_c^{-1} takes the form

$$\omega_c^{-1} = \frac{1.8 \times 10^{-18} \text{ sec}}{\tau_E^{\frac{1}{2}}[\text{sec}]\ T_c^{\frac{1}{4}}[\text{K}]} (T_c - T)^{-5/4}[\text{K}] \quad . \tag{4.11}$$

For this expression we have taken $I_c = I_c(\text{strip})$, with the understanding that a reduced value of I_c will increase the value of ω_c^{-1} proportionately. It is evident from Fig. 4.2 that of the three materials, Al satisfies the approximations in the high-frequency limit

---

* For the case of an ideal Josephson weak link (tunnel junction or small metallic constriction) with critical current I_c and intrinsic junction resistance R_J, it has been shown[31] that $I_cR_J = \hbar/(2e\tau_o)$. Therefore, the neglect of R_J in R_{eff} may be valid only when $\omega_c\tau_o >> 1$.

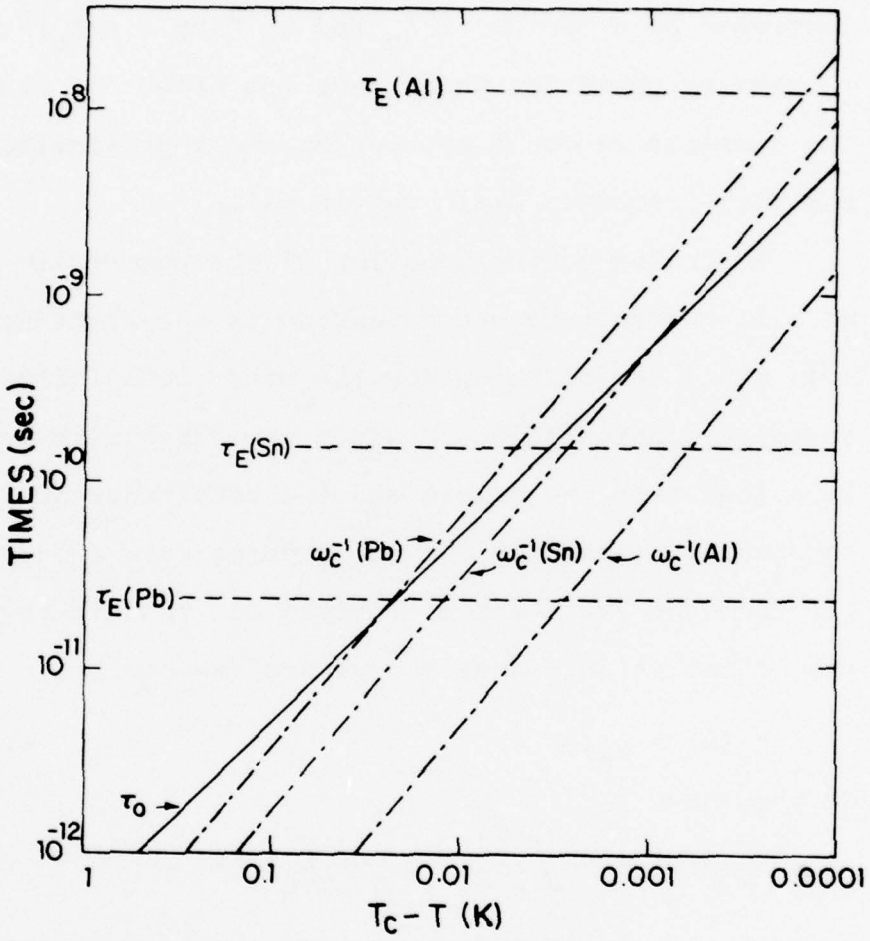

Fig. 4.2 Characteristic times τ_E, τ_o, and ω_c^{-1} as a function of temperature near T_c for Al, Sn, and Pb in the dirty limit, according to Eqs. (3.49) and (4.11). The values of τ_E are from refs. 41 (Al), 36 (Sn), and 40 (Pb).

over the widest range of temperatures. They are approximately true for Sn beyond about 10 mK from T_c, and generally untrue for Pb. In the clean limit, τ_o is increased by a factor $\simeq \ell/\xi_o$ and ω_c^{-1} by $\simeq (\ell/\xi_o)^{\frac{1}{2}}$ while τ_E remains the same, which have the effect of increasing the temperature range over which the approximations in the high-frequency limit remain valid.

Returning to the behavior of the phase-slip center, we will concentrate our attention on the right-hand side $x>0$, since the solution for the other side follows from symmetry considerations. Since the disequilibrium is localized near the origin and the total current is constant in time, the current becomes pure supercurrent far from the PSC. The potentials out in this region are then constant in space, and we are free to set

$$\mu_n(\infty) = \mu_s(\infty) = 0 \quad . \tag{4.12}$$

We then have

$$\mu_s(x,t) = eL\int_x^\infty \dot{I}_s dx = -eL\int_x^\infty \dot{I}_n dx$$

$$= -\frac{L}{R}\dot{\mu}_n(x,t) = -\tau_o\dot{\mu}_n(x,t), \quad x>0. \tag{4.13}$$

This, together with the fact that μ_n is bounded over all times, implies that

$$\bar{\mu}_s(x) = 0 \ , \ x > 0 \quad . \tag{4.14}$$

Since the dc decay length is Λ, the other time averages are:

$$\bar{I}_n(x) = I - \bar{I}_s(x) = \bar{I}_n(x=0)\, e^{-x/\Lambda} \qquad (4.15)$$

$$\bar{\mu}_n(x)/e = \bar{\Phi}(x) = \bar{I}_n(x=0)\frac{\Lambda}{\sigma A}\, e^{-x/\Lambda} \qquad (4.16)$$

This behavior is plotted in Fig. 4.3 together with the corresponding behavior on the left side of the PSC. Note that the currents are symmetric with respect to the origin, while the nonequilibrium potential is anti-symmetric. This time-averaged behavior of the currents and potentials is the same as that in the SBT model, which was confirmed experimentally by Dolan and Jackel.[19] In the next section we examine the associated time-dependent behavior within our transmission-line model for the phase-slip center.

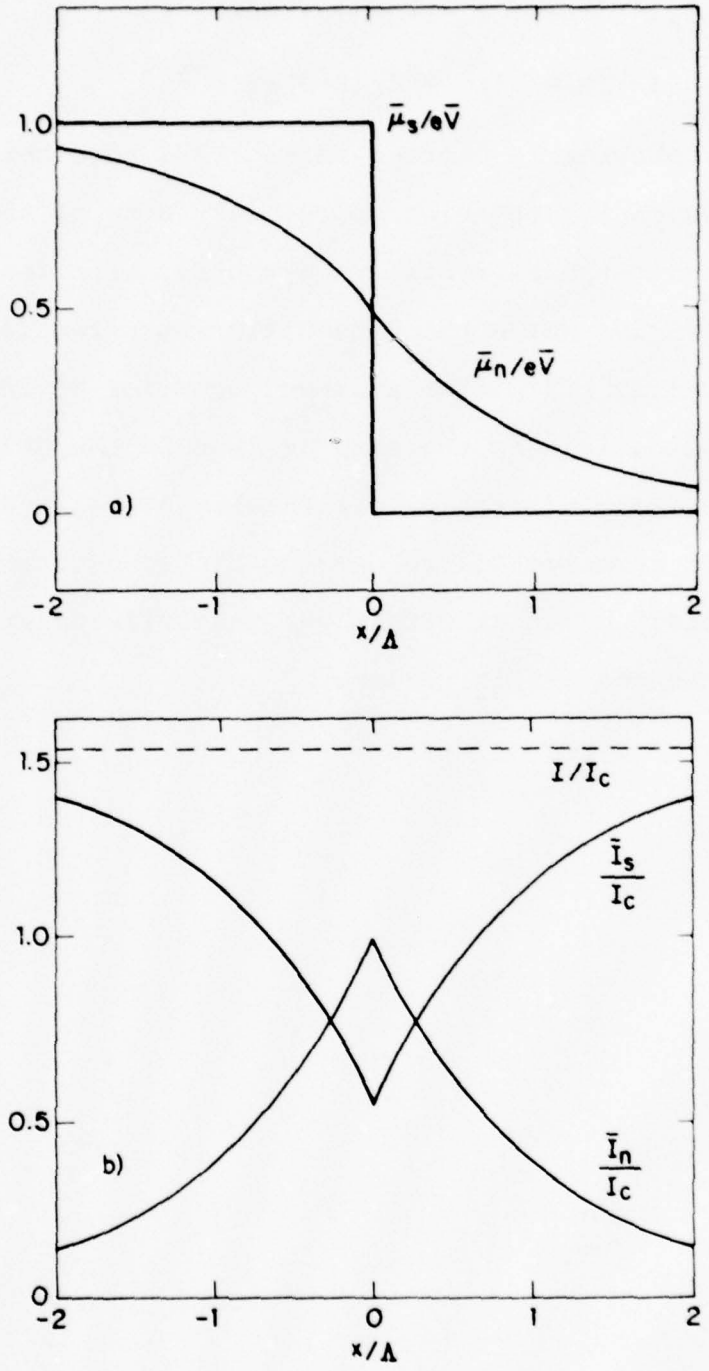

Fig. 4.3 Spatial dependence of the time-averaged potentials (a) and currents (b) in the region near a phase-slip center.

4.2 Waves in the Vicinity of the PSC

We first direct our attention to the oscillations at the origin, and look for a solution with I_n periodic in time with a fundamental frequency $\Omega = 2e\bar{V}/\hbar$. Expanding in a Fourier series with coefficients c_m, we have

$$I_n(x=0,t) = \sum_{m=-\infty}^{\infty} c_m(\Omega)\ e^{im\Omega t} \tag{4.17}$$

where

$$c_o = \bar{I}_n(0) = \bar{V}/R_{eff} \tag{4.18}$$

Applying the results of Appendix II [Eqs. (A2.18) and (A2.20)] for a Josephson element shunted by an impedance $2Z(\omega)$ (see Fig. 3.1b), we obtain

$$c_m(\Omega) = -\frac{\Omega I_c}{2\pi} \int_0^{2\pi/\Omega} dt\ e^{-im\Omega t} f(\Delta\theta(t)),\ m\neq 0, \tag{4.19}$$

where

$$\Delta\theta(t) = \Omega t + \frac{4e}{\hbar} \sum_{m\neq 0} Z(m\Omega)\ \frac{c_m}{im\Omega}\ (e^{im\Omega t}-1)\ . \tag{4.20}$$

Given any relation $f(\Delta\theta)$, these equations provide a formal solution to the problem, which can be evaluated on a computer by iteration, although the existence of a solution is not necessarily guaranteed. We will deal later with a particular $f(\Delta\theta)$ for which these equations can be solved analytically.

Given the set of these Fourier coefficients c_m, we can express the space and time dependence of all the physical quantities of interest in the problem. Considering the right-hand side $x>0$, we have

$$I_n(x,t) = I - I_s(x,t) = \sum_m c_m \, e^{i(m\Omega t - k_m x)}, \quad (4.21)$$

where

$$k_m = k_{m_R} + i k_{m_I} \equiv k(m\Omega) \quad (4.22)$$

is the wave vector from Eq. (3.37), and

$$k_{m_I} < 0 \;\; ; \;\; k_{m_R} \gtrless 0 \text{ for } m \gtrless 0 \, , \quad (4.23)$$

which corresponds to decaying waves propagating to the right. The potentials Φ, μ_n, and μ_s can likewise be expressed in terms of the c_m's:

$$\Phi(x,t) = \sum_m Z(m\Omega) \, c_m \, e^{i(m\Omega t - k_m x)} \quad (4.24)$$

$$\mu_n(x,t) = \frac{e}{\sigma A} \int_x^\infty I_n(x',t)\,dx'$$

$$= \frac{e}{\sigma A} \sum_m \frac{c_m}{ik_m} e^{i(m\Omega t - k_m x)} \quad (4.25)$$

$$\mu_s(x,t) = -\tau_o \dot{\mu}_n(x,t)$$

$$= -\frac{\tau_o e}{\sigma A} \sum_m \frac{im\Omega}{ik_m} c_m \, e^{i(m\Omega t - k_m x)} \quad (4.26)$$

The dependence for negative x can be obtained by symmetry: the currents I_n and I_s are symmetric on either side of the origin, the potential Φ is antisymmetric, and

$$\mu_n(-x) - \mu_n(0) = -[\mu_n(x) - \mu_n(0)]$$
$$\mu_s(-x) - \mu_n(0) = -[\mu_s(x) - \mu_n(0)] \quad (4.27)$$

The apparent asymmetry between the behavior of μ_n (and μ_s) at $x = \pm\infty$ arises from our arbitrary boundary condition

that $\mu_n(\infty) = \mu_s(\infty) = 0$. Since only potential differences are important, this is of no concern.

The condition of constant current implies that the voltage V_∞ across the PSC, as measured by probes far away from the nonequilibrium region, must include an ac component:

$$V_\infty = [\mu_n(-\infty) - \mu_n(\infty)]/e = 2\mu_n(0)/e$$
$$= \bar{V} + \frac{\Lambda}{\sigma A} \sum_{m\neq 0} c_m \, e^{im\Omega t}/\sqrt{(1+im\Omega\tau_o)(1+im\Omega\tau_E)} \quad . \quad (4.28)$$

This is analogous to the ac voltage which appears in the RSJ model, and follows from integrating the (spatially symmetric) oscillating normal current.

The linear relation

$$f(\Delta\theta) = \Delta\theta/2\pi \ , \quad 0 < \Delta\theta < 2\pi \ , \qquad (4.29)$$

which is one branch of a periodic sawtooth curve passing between zero and one, has the unique advantage of yielding an analytic solution for the Fourier coefficients. Although its instantaneous phase-slip at the end of each cycle may be physically unrealistic, similar dc supercurrent-phase relations have been measured and have been applied to explain properties of microbridges.[50,62] If we assume here that the system remains on a single branch for the entire period (i.e. there is a single phase-slip event at the beginning of each period), then the integral in Eq. (4.19) can be evaluated explicitly (see Appendix II) to yield

$$c_m = \frac{I_c}{2\pi i m} / \left[1 + \frac{I_c}{2\pi i m} \frac{2Z(m\Omega)}{\bar{V}}\right] , \quad m \neq 0 \qquad (4.30)$$

We will use this solution below to illustrate many of the more general features of the model.

Looking first at the oscillations at the center, we have plotted in Fig. 4.4 the time dependence of the quantities $I_n(0,t)$ and $\Phi(0^+,t)$ for Sn at $T/T_c = 0.99$, $\bar{V} = I_c R_{eff}$, and $I_c = I_c(\text{strip})$, using the linear current-phase relation. The oscillations repeat with the Josephson period $\tau_J = 2\pi/\Omega$, and the abrupt jumps at the end of each cycle represent the discontinuous phase-slip process built into the piecewise-linear $f(\Delta\theta)$. The ac parts of I_n and Φ are approximately proportional to one another. In the high-frequency limit where the effective impedance $2Z(m\Omega)$ becomes purely resistive and independent of m, the proportionality would be exact. In the present case $\omega_c \tau_o = 2.2$, so that the high-frequency limit is only approximately valid.

As we noted before, the oscillations at the origin can be regard as generating charge imbalance waves which propagate out in both directions from the center. In Fig. 4.5 we show the spatial dependence (for $x>0$) of the waves generated by the oscillations in Fig. 4.4, at a moment in time corresponding to $t = \tau_J/4$. The succession of periodically spaced vertical jumps correspond to phase-slip events successively earlier in time.

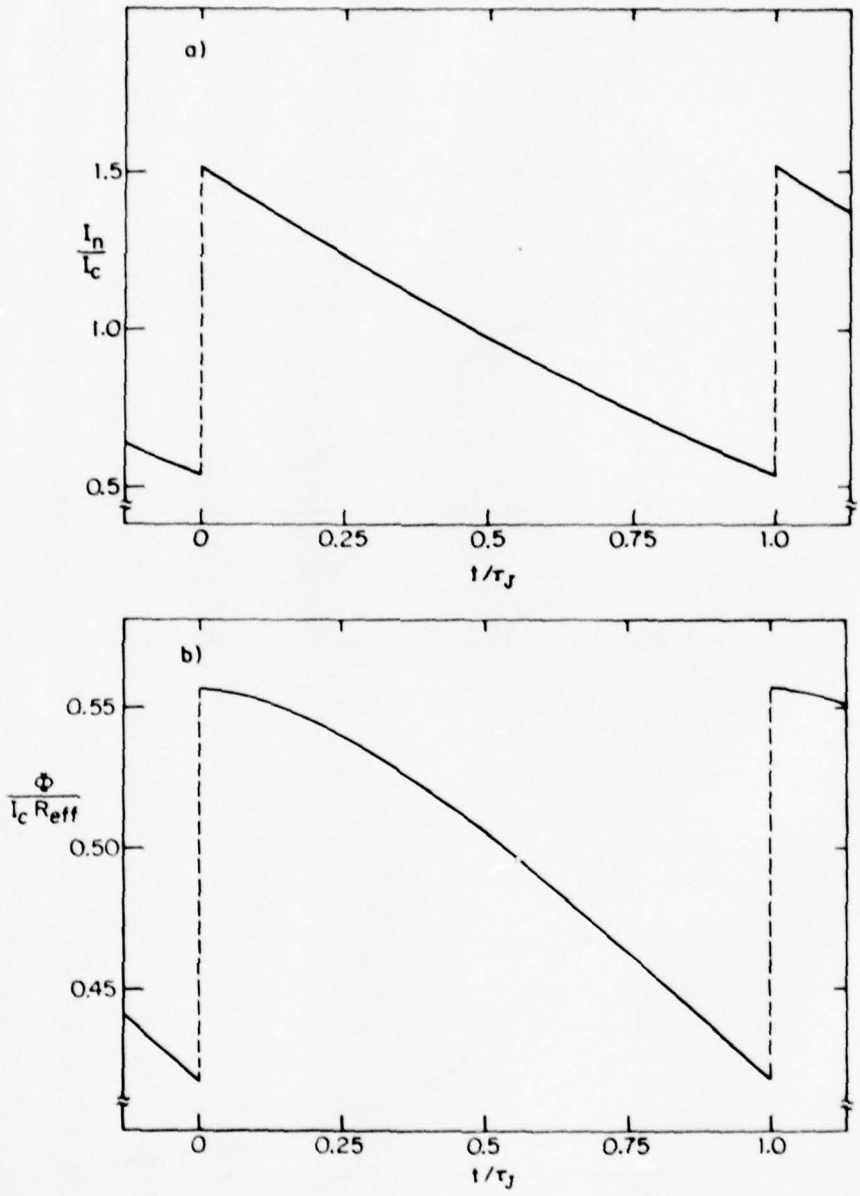

Fig. 4.4 Time dependence within a single Josephson period τ_J of the oscillations in the center of (a) $I_n(0,t)/I_c$ and (b) $\Phi(0,t)/I_c R_{eff}$ using the linear $f(\Delta\theta)$ and parameters $\tau_E/\tau_o = 11$, $\omega_c\tau_o = 2.2$, $\bar{V} = I_c R_{eff}$, and $I = 1.5\ I_c$, appropriate for Sn at $T/T_c = 0.99$. Both I_n and Φ are discontinuous at the beginning and end of each cycle for the linear $f(\Delta\theta)$.

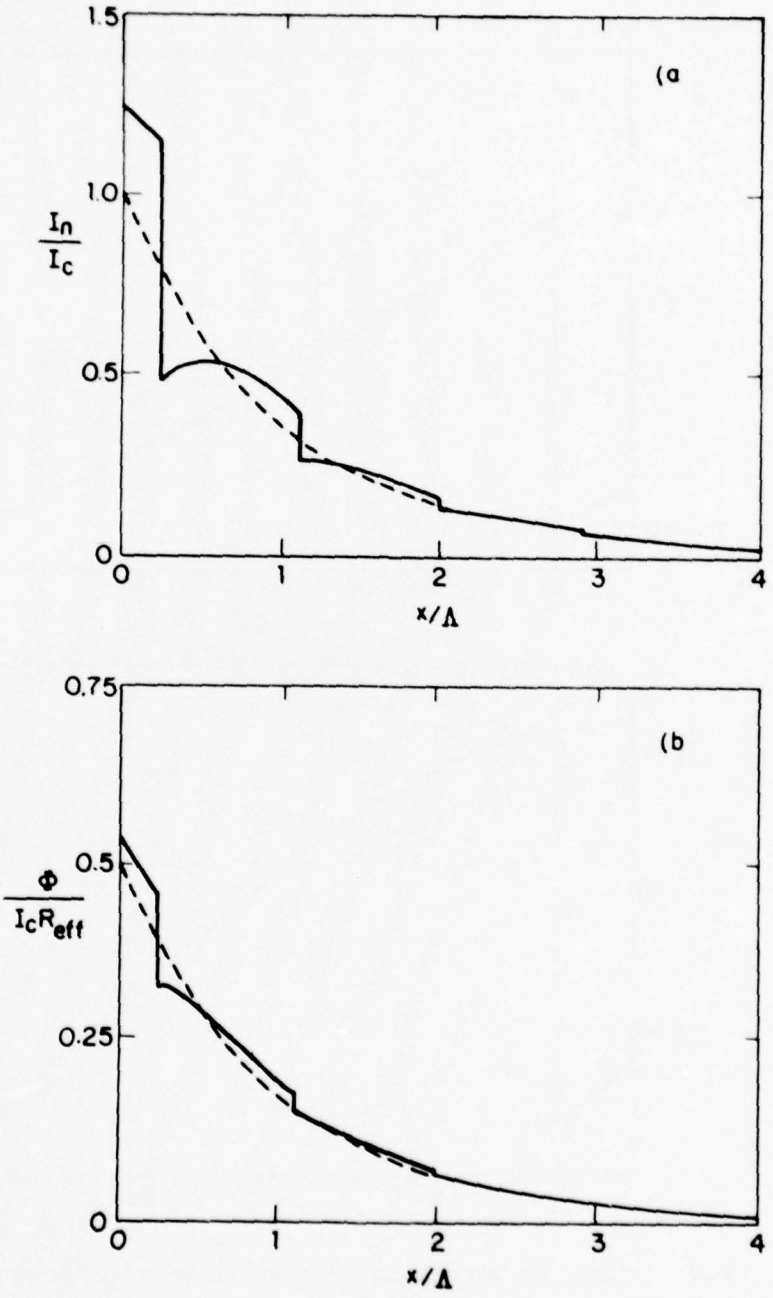

Fig. 4.5 Spatial dependence (for $x > 0$) of (a) I_n/I_c and (b) $\Phi/I_c R_{eff}$ at $t = 0.25\ \tau_J$ for the same parameters as in Fig. 4.4. The dashed curves are the dc averages.

The discontinuous nature of these jumps is again an artifact of the linear current-phase relation, but here they make the progression of the waves easily visible. Their wavelength L is given in the high-frequency approximation as

$$L = v\tau_J = \frac{\Lambda}{\sqrt{\tau_o \tau_E}} \frac{h}{2e\bar{V}} \quad , \tag{4.31}$$

which works out to $\simeq 0.85\ \Lambda$ for the case of Fig. 4.5. Increasing the voltage would decrease the wavelength proportionately. Since the high-frequency limit is only approximately valid here, the phase velocity depends somewhat on frequency, producing a waveform whose shape evolves slightly as it propagates down the line. The corresponding behavior of $\mu_n(x,t)$ and $\mu_s(x,t)$ is shown in Fig. 4.6.

In Fig. 4.7 we present the nonequilibrium potential $\Phi(x>0, t=\tau_J/4)$ which would arise from the classic sinusoidal $f(\Delta\theta)$, again using the same parameters as in Figs. 4.4 - 4.6. This solution was obtained by iteration on a computer. Here the waves have no discontinuous jumps, since $f(\Delta\theta)$ is continuous. Nevertheless, the essential picture of propagating and attenuating waves remains the same.

As we noted in Eq. (3.48), when $\tau_o \neq \tau_E$ the ac decay length Λ_{ac} becomes less than the dc decay length Λ. In the high-frequency limit, for the case where $\tau_E >> \tau_o$,

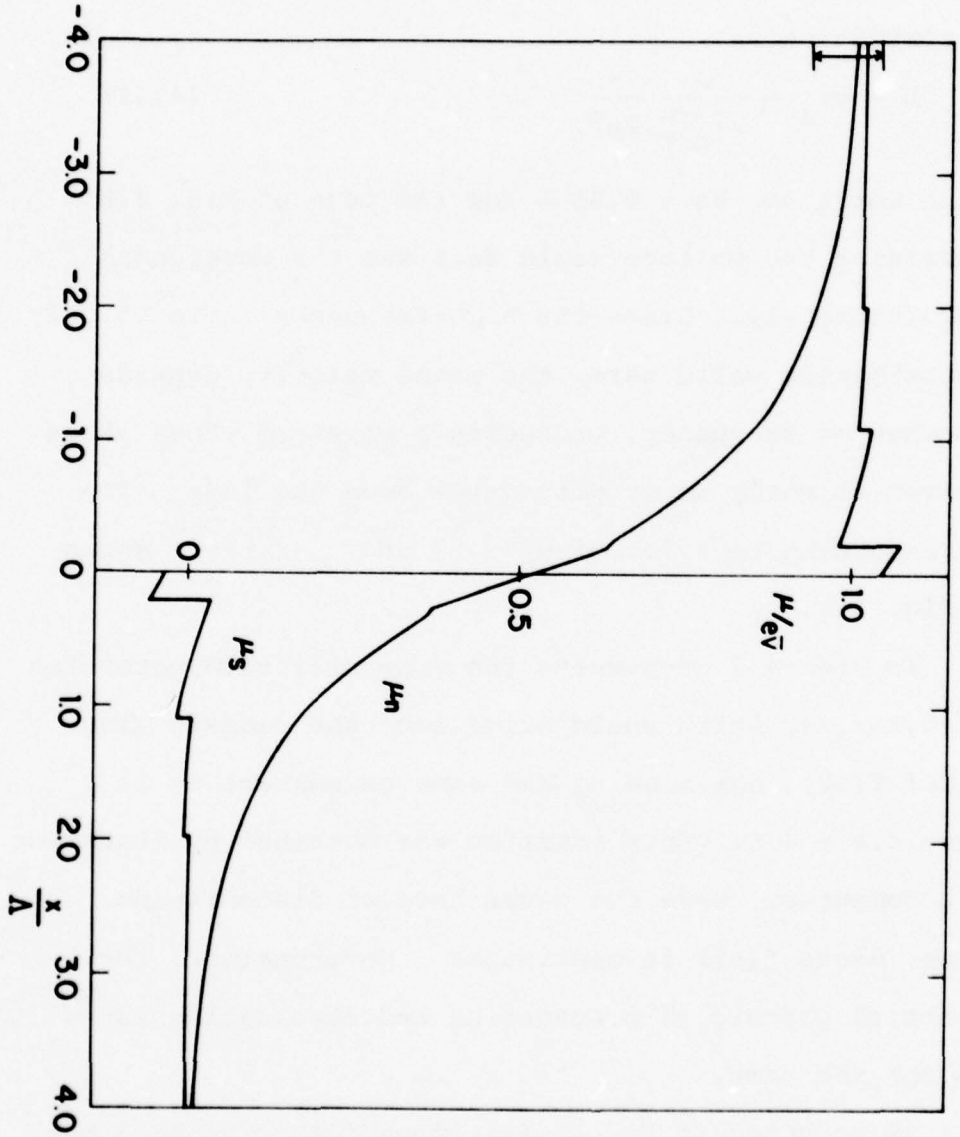

Fig. 4.6 Spatial dependence of the potentials $\mu_n/e\bar{V}$ and $\mu_s/e\bar{V}$ for the same set of parameters as in Fig. 4.5. The behavior for $x < 0$ is included to make clear the symmetry of the solutions. The range of variation of $\mu(-\infty)/e\bar{V}$ is indicated by arrows on the left.

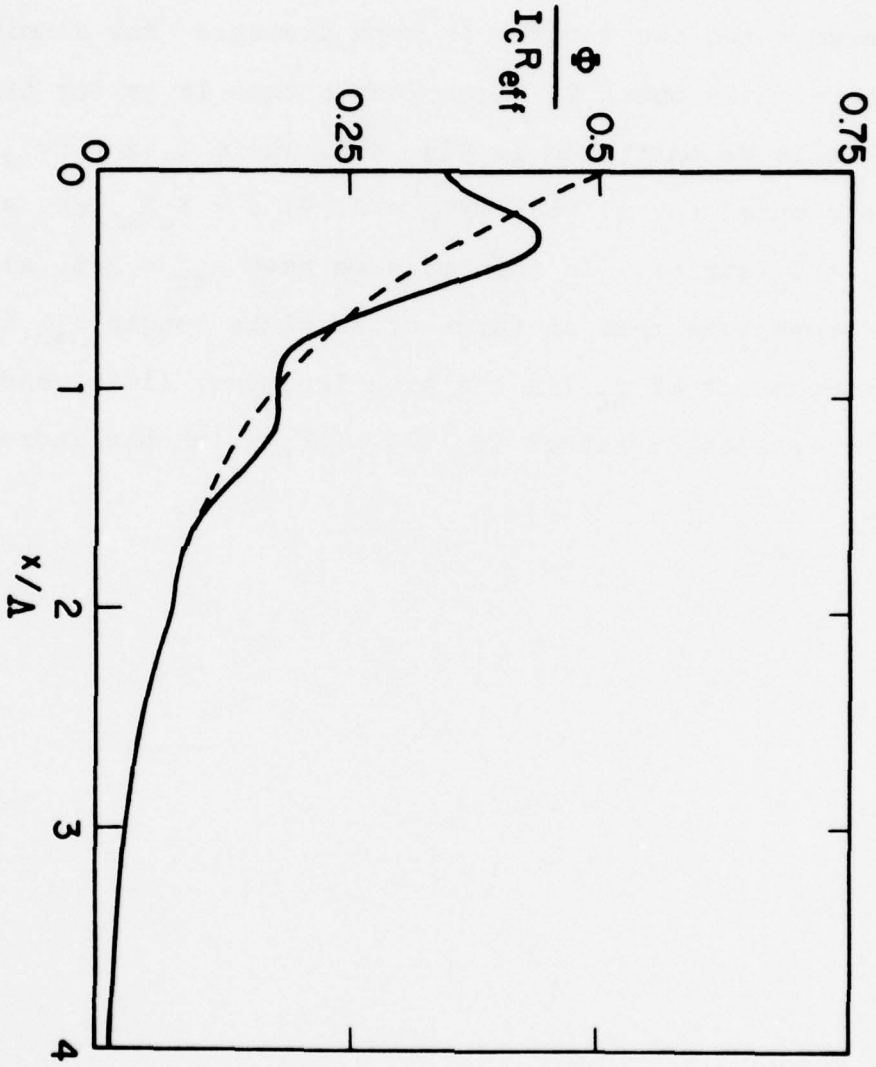

Fig. 4.7 The spatial dependence of $\Phi/I_c R_{eff}$ for the same parameters as in Fig. 4.5 (except for $I = 1.0\ I_c$), but using a sinusoidal $f(\Delta\theta)$. The dashed curve is the dc average.

we have

$$\Lambda_{ac} = 2\Lambda \sqrt{\tau_o/\tau_E} \ , \qquad (4.32)$$

which is about 0.6 Λ for Figs. 4.5 - 4.7. The difference between two two lengths is more dramatic for aluminum, where τ_E is about 80 times longer than it is for tin. This is demonstrated in Fig. 4.8, where $I_n(x>0, t=\tau_J/2)$ is plotted for Al with $T/T_c = 0.99$, $\bar{V} = I_c R_{eff}/2$, and $I_c = I_c(\text{strip})$. In this case we have $\Lambda_{ac} \simeq \Lambda/8$, although we emphasize that in terms of absolute length Λ_{ac} is independent of τ_E (in the high-frequency limit) and has not decreased; rather it is $\Lambda \propto \sqrt{\tau_E}$ which has increased.

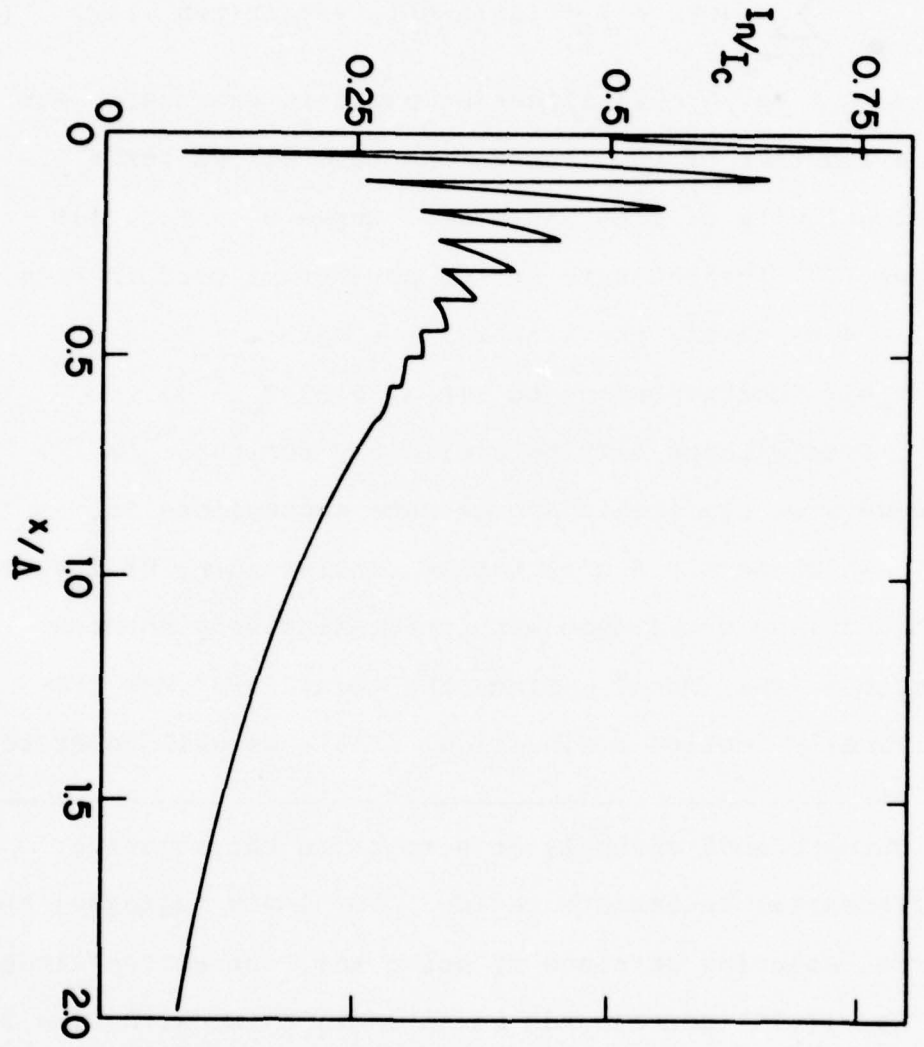

Fig. 4.8 Spatial dependence of $I_n(x,t=0.5\tau_J)/I_c$ for the linear $f(\Delta\theta)$ and parameters $\tau_E = 280\ \tau_o$, $\omega_c\tau_o = 11$, $\bar{V} = 0.5\ I_c R_{eff}$, and $I = 1.0\ I_c$, appropriate to Al at $T/T_c = 0.99$. Note that the horizontal scale is expanded by a factor of two compared to Fig. 4.5.

4.3 I-$\bar{V}$ Characteristics for the Phase-Slip Center

The I-$\bar{V}$ relation for a general $f(\Delta\theta)$ can be expressed in the form

$$I = I_n(x=0,t=0) + I_s(0,0)$$
$$= \sum_{m=-\infty}^{\infty} c_m(\Omega) + I_c[f(\Delta\theta(t=0^+)) + f(\Delta\theta(t=0^-))]/2 \quad . \quad (4.33)$$

Since $\Omega = 2e\bar{V}/\hbar$ this allows an explicit expression for I as a function of $\bar{V}$. (The second term allows for a discontinuity of $f(\Delta\theta)$ at t=0.) Curve b in Fig. 4.9 shows $I(\bar{V})$ for the same set of parameters used in Figs. 4.4 - 4.6, namely the linear $f(\Delta\theta)$ with $\omega_c\tau_o=2.2$ and $\tau_E/\tau_o=11$, corresponding to tin at 0.99 T_c.*

Even without solving explicitly for the c_m's, however, we can obtain approximate expressions for $I(\bar{V})$ which permit a qualitative understanding of its behavior, by comparison with the resistively shunted junction (RSJ) model. Since the terms "RSJ" has traditionally implied a sinusoidal $f(\Delta\theta)$, we will refer to

---

* Curve b ends abruptly at a point in the negative differential resistance region. For lower voltages, the formal solution obtained by using the Fourier coefficients of Eq. (4.30) corresponds to an oscillation with $\Delta\theta > 2\pi$ (and $I_s > I_c$) over a portion of the cycle. If we attempt to solve Eqs. (4.19) and (4.20) by computer iteration using the actual sawtooth $f(\Delta\theta)$, the c_m's do not converge to a self-consistent solution, implying that no such solution exists in this region.

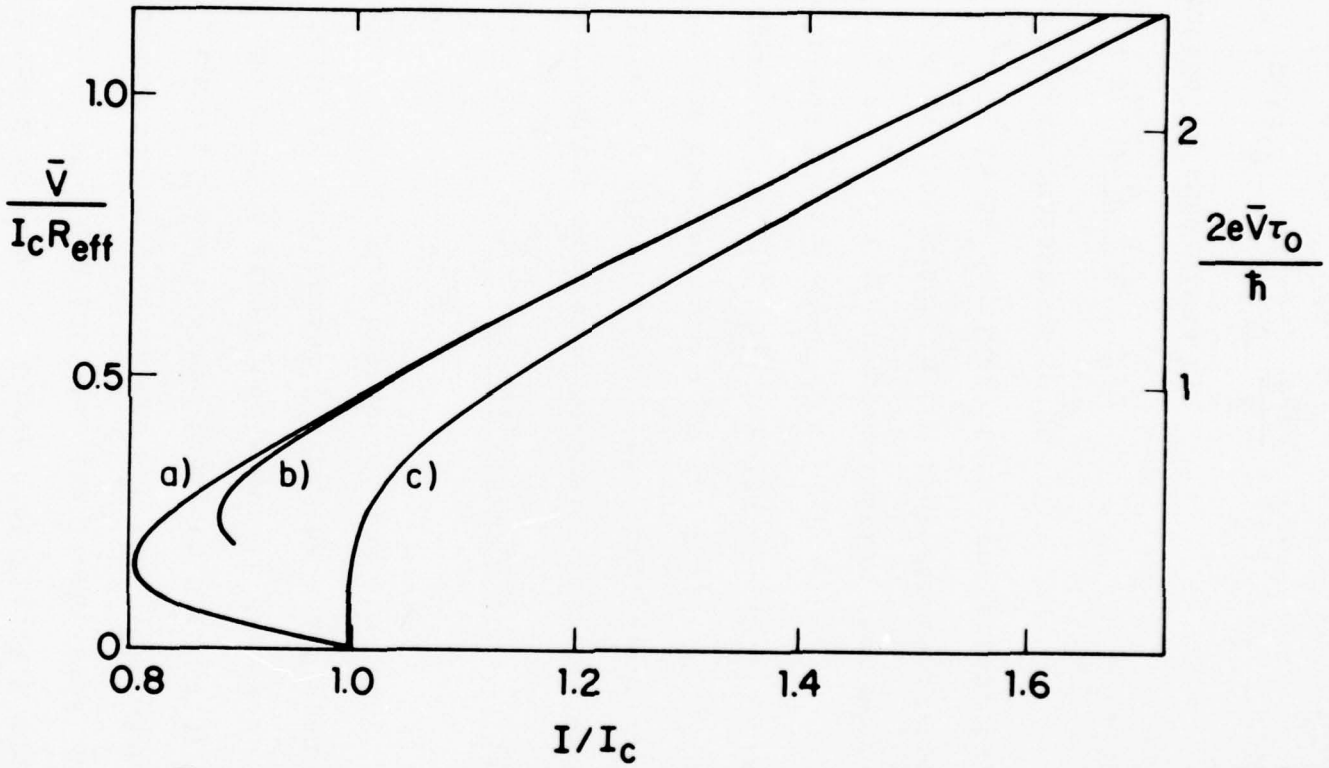

Fig. 4.9 I-$\bar{V}$ curves for τ_E/τ_o = 11 for the linear f($\Delta\theta$), for (a) the high-frequency limit [Eq. (4.36)], (b) the actual solution for $\omega_c\tau_o$ = 2.2 [Eq. (4.33)], and (c) the low-frequency or GRSJ solution [Eq. (A2.13)].

a "generalized RSJ" model (GRSJ) which is unrestricted in this regard. (See Appendix II for a detailed exposition of the GRSJ model.) Curve c of Fig. 4.9 shows the GRSJ curve [Eq. (A2.13)] for the linear $f(\Delta\theta)$ and a shunt resistance $R_{eff} = 2\Lambda/\sigma A$. In the limit of high voltages, curves b and c agree [compare Eqs. (4.4) and (A2.9)]. However, in the range shown in Fig. 4.9, curve c deviates substantially from the exact result of curve b. This occurs because of the frequency dependence of

$$Z_{eff} = 2Z(\omega) = R_{eff}\sqrt{(1+i\omega\tau_o)/(1+i\omega\tau_E)} \qquad (4.34)$$

which is the shunt impedance equivalent to the transmission lines on either side of the core, as in Fig. 4.1b. For the special case $\tau_o = \tau_E$, $Z_{eff} = R_{eff}$ for all frequencies and the GRSJ results Eq. (A2.13) is the exact solution for our model.

For $\tau_E \neq \tau_o$, a simple approximation that does much better, and becomes exact in the high-frequency limit $\omega_c\tau_o$, $\omega_c\tau_E >> 1$, is to consider the dc resistance to be R_{eff} but the ac resistance to be

$$R_{ac} = R_{eff}\sqrt{\tau_o/\tau_E} \ . \qquad (4.35)$$

The solution is then given by

$$I = I_{GRSJ}(\bar{V}, R_{ac}) + \bar{V}\left(\frac{1}{R_{eff}} - \frac{1}{R_{ac}}\right) , \qquad (4.36)$$

that is, by the inverse function of $\bar{V}_{GRSJ}(I,R_{ac})$ with a

correction that accounts for the different dc resistance. Using the limiting forms of I_{GRSJ} at I_c and for $I \gg I_c$ [Eq. (A2.11)], we have

$$I \to \begin{cases} I_c + (1 - \sqrt{\tau_E/\tau_o}\,)\bar{V}/R_{eff} , & \bar{V} \ll I_c R_{eff} \\ \langle f \rangle I_c + \bar{V}/R_{eff} , & \bar{V} \gg I_c R_{eff} \end{cases} \tag{4.37}$$

Thus we see that at high voltages we recover a differential resistance equal to R_{eff}. The solution (4.36) is plotted as curve a of Fig. 4.9, for the same parameters and linear $f(\Delta\theta)$ used in the other curves. Except for low voltages, this high-frequency-limit solution provides a very good approximation to the full solution of Eq. (4.33) even though $\omega_c \tau_o = 2.2$.

The most striking feature about curves a and b in Fig. 4.9 is the existence of nonzero-voltage solutions for currents less than the critical current I_c, so that voltage is a hysteretic function of current. In order to investigate this in greater detail, we have plotted in Fig. 4.10 the I-$\bar{V}$ relation of Eq. (4.36) for various values of τ_E/τ_o, using the linear current-phase relation. With the voltage scaled to $I_c R_{eff}$ and the current to I_c, the curves are independent of ω_c (provided that the high-frequency limit remains valid). For the special case $\tau_E = \tau_o$, Eq. (4.36) gives exactly the GRSJ curve. If $\tau_E \neq \tau_o$, the curve lies to the right of the GRSJ curve

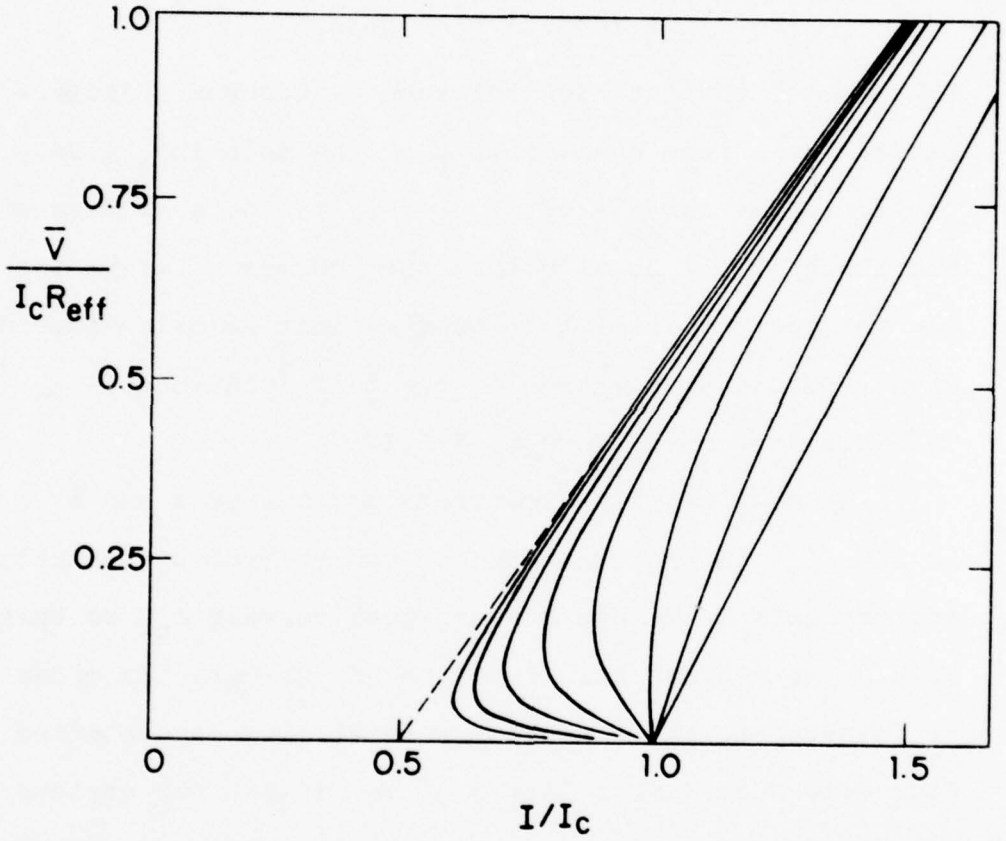

Fig. 4.10 I-$\bar{V}$ characteristics in the high-frequency limit, from Eq. (4.36), for the linear $f(\Delta\theta)$ and various values of τ_E/τ_o. The curves are scaled so that all have the same critical current and high-voltage differential resistance. The values of τ_E/τ_o corresponding to the curves from left to right are 1024, 256, 64, 16, 4, 1, ¼, and 1/16. The dashed line is the high-voltage asymptote.

[i.e. it has a larger $I(\bar{V})$], while in the more usual case $\tau_E > \tau_o$, it lies to the left. This is true for any current-phase relation, and since the GRSJ curve rises vertically at $I = I_c$, $\tau_E > \tau_o$ provides the condition for hysteresis.

This hysteresis can be qualitatively understood in terms of the fact that the effective ac resistance shunting the junction is smaller than the dc resistance [Eq. (4.35)] in the regime $\tau_E > \tau_o$ in which hysteresis is present. The amplitude of voltage oscillations across the junction is therefore reduced relative to the dc average value, so that the voltage driving the Josephson oscillation is closer to being a constant voltage bias. The resulting I-$\bar{V}$ curve then lies closer to the voltage-biased line which forms the high-voltage asymptote, and as is evident from Fig. 4.10 approaches this line at lower and lower voltages as τ_E/τ_o is increased. The maximum amount of hysteresis, therefore, corresponds to the curve remaining on the voltage-biased line all the way down to zero voltage:

$$I_m \to \langle f \rangle I_c \text{ as } \tau_E/\tau_o \to \infty , \qquad (4.38)$$

where I_m is the current at which the system switches hysteretically back into the zero-voltage state. Even when the high-frequency limit does not strictly hold,

as in curve b of Fig. 4.9, $\tau_E > \tau_o$ remains the condition for the presence of hysteresis, since the magnitude of $Z_{eff}(\omega_c)$ is still smaller than R_{eff}. The amount of hysteresis is somewhat reduced, but this is not a universal quantity even in the high-frequency limit, depending on the details of the current-phase relation. We note that the same argument can also explain qualitatively the well-known hysteresis in the capacitively-shunted RSJ model, where the effective impedance $R_J/(1 + i\omega R_J C_J)$ also decreases in magnitude with increasing frequency.

In an actual experiment, one typically measures voltage as current is swept out for a series of temperatures near T_c. In Fig. 4.11, we plot theoretical curves from our model in an analogous way, showing the onset and development of hysteresis. They correspond to the linear current-phase relation in the high-frequency limit, and were obtained from curves such as those in Fig. 4.10 by using the temperature scaling relations

$$\tau_E/\tau_o \propto (1-T/T_c)$$
$$I_c \propto (1-T/T_c)^{3/2} \qquad (4.39)$$
$$I_c R_{eff} \propto (1-T/T_c)^{5/4} \quad .$$

Within the given approximations these curves are independent of material. The onset of hysteresis at $\tau_E/\tau_o = 1$ would correspond to $T_c - T \approx 4$ mK for Sn, and ≈ 0.05 mK for Al.

Fig. 4.11 I-$\bar{V}$ curves for the linear current-phase relation in the high-frequency limit for various values of τ_E/τ_o, with the temperature dependence reintroduced in accordance with Eq. (4.39). The arrows pointing upward represent hysteretic switching at the critical current I_c into the dissipative state, and the downward-pointing arrows represent switching back into the zero-voltage state at the current I_m. The values of τ_E/τ_o corresponding to the curves from left to right are $\frac{1}{2}$, 1, 2, 3, 4, and 5.

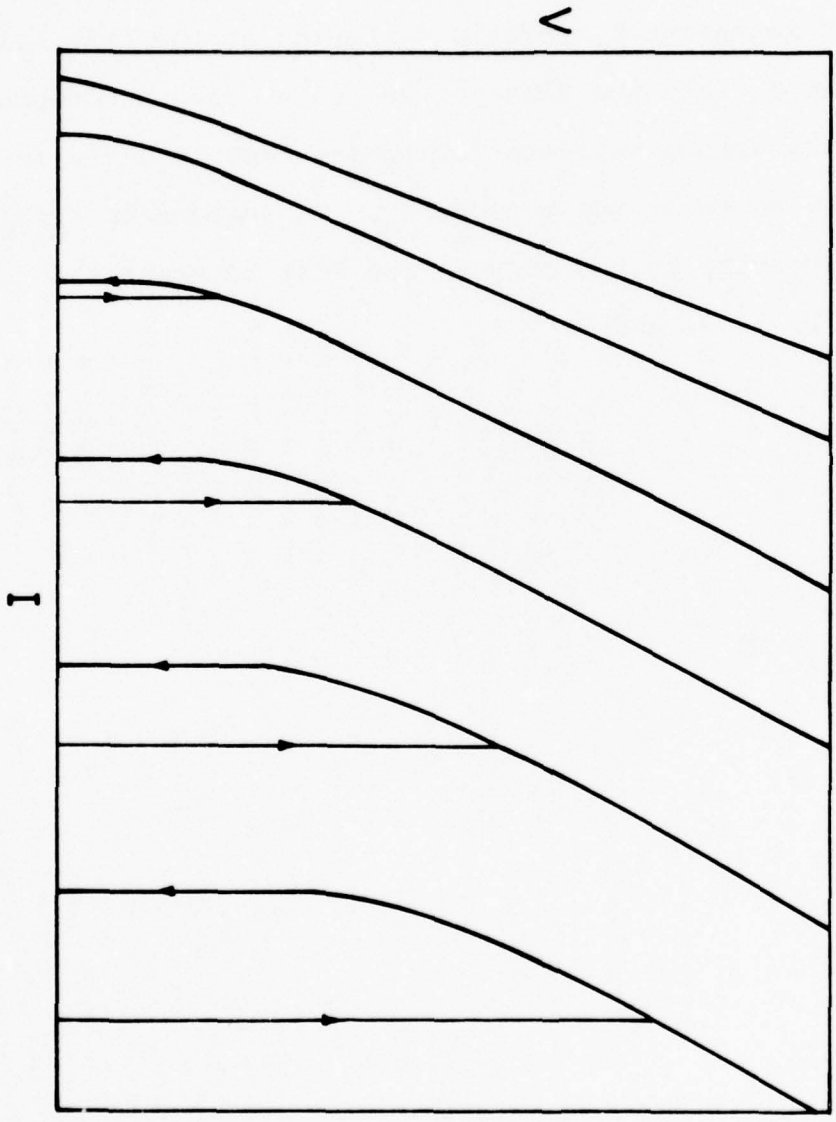

Fig. 4.11

The development of hysteresis in Fig. 4.11 is qualitatively similar to that seen in many experiments. Quantitative comparisons, however, are complicated by a number of factors which we have not considered in our model, such as noise-induced smearing of $I-\bar{V}$ curves close to T_c and heating effects farther from T_c. In particular, heating has been shown to account reasonably well for hysteresis in some cases.[1,46,47,63] The intrinsic hysteresis which our model predicts should be viewed not as an alternative explanation of hysteresis, but as a supplementary mechanism which should become important near T_c, where the heating-induced hysteresis disappears more rapidly.

We can, however, make some rough preliminary comparisons. In our model for intrinsic hysteresis, the normalized return current I_m/I_c saturates at a fixed value $\langle f \rangle$ with decreasing temperature, whereas that associated with heating decreases towards zero as the PSC eventually becomes a self-heating normal hotspot. In thin-film microstrips of tin, the latter behavior is typically seen. In clean tin whisker crystals, however, where heating effects should be somewhat less severe, Tidecks and Meyer[64] have noted a saturation effect similar to that predicted by our model. The onset of hysteresis near T_c is another basis for comparison. This onset has

been observed in the range from 1.5 mK to 10 mK from T_c for both tin whiskers[64] and tin microstrips[51], roughly consistent with the condition $\tau_o = \tau_E$ (about 4 mK in Fig. 4.2), although rather large sample-to-sample variations remain to be explained. Comparable data for tin microstrips in an electrically unshielded environment do not show hysteresis until significantly farther from T_c,[21,51] presumably because of rf noise rounding. Because of these effects, a careful set of measurements on hysteresis near T_c in well-characterized and well-shielded samples are needed to provide a more detailed and definitive comparison with our theory.

In summary, we have developed a new model for the phase-slip center, which is based on coupling Josephson oscillations in the core of the PSC to the transmission-line equivalent developed in Chapter III to describe charge imbalance dynamics. When averaged over time, our model reduces to the SBT picture of the spatial dependence of the potentials inside a PSC, which has been experimentally confirmed by Dolan and Jackel. Another important consequence of our model is the predicted existence of intrinsic hysteresis in the dc I-$\bar{V}$ curves, and preliminary comparisons with experiment are promising but complicated by heating and other factors. We have also made preliminary investigations

into the possible application of our model to the interaction of closely-spaced PSC's, with some encouraging results (see Section 5.1). In conclusion, our model provides a qualitative understanding of ac effects in PSC's, even though its quantitative validity remains uncertain.

CHAPTER FIVE: OTHER TOPICS

The previous chapters could not of course cover all aspects of nonequilibrium phenomena in superconducting phase-slip centers. In the present chapter we round off the main body of this report with a discussion of some additional topics which were dealt with in the course of our investigations. Although the treatment is not as complete as that in the earlier chapters, it should help provide guidance for future research in the area.

5.1 Detection of Charge Imbalance Waves and Interactions Between Phase-Slip Centers

How does one go about detecting high-frequency waves in a superconductor? Two ideas come to mind. One is the Carlson-Goldman experiment,[23] where a superconducting tunnel junction was made to serve as a frequency and wave-vector selective detector of thermally-activated collective waves by application of a dc voltage and an external magnetic field. The other is the detection of microwaves by the appearance of Josephson steps in a Josephson junction. These two methods are fundamentally rather similar, and in the present case one can use one Josephson element (e.g. a small tunnel junction probe) in a similar way as a selective detector of waves generated by another Josephson element (e.g. a phase-slip center in a long filament).

Consider Fig. 5.1a, where a superconducting microstrip contains a localized weak spot, and nearby on the scale of the ac decay length (of order the quasiparticle diffusion length Λ) is located a small Josephson tunnel junction. If the current flowing in the strip exceeds the critical current of the weak spot, then a PSC will nucleate there, and will generate charge imbalance waves which extend out beyond the tunnel junction probe. In particular, the condensate electrochemical potential μ_s will oscillate with fundamental frequency $\Omega = 2e\bar{V}/\hbar$ [Eq. (4.26)], where $\bar{V}$ is the total dc voltage across the PSC. If in addition, the upper electrode of the tunnel junction is biased at a dc voltage V' relative to the lower one (via the superconducting side-tab in Fig. 5.1a), then the potential difference $\Delta\mu_s$ across the junction will consist of the sum of a constant term eV' and a nonequilibrium oscillatory part $\propto e^{i\Omega t}$. Then, since the phase difference $\Delta\theta$ across the junction evolves as $\hbar\dot{\Delta\theta} = -2\Delta\mu_s$, $\Delta\theta$ will consist of a linear term and an oscillatory term. Because of the nonlinear mixing properties of the Josephson current through the junction, a time-average supercurrent will flow given the usual conditions for an ac Josephson step, namely $V' = n\hbar\Omega/2e = n\bar{V}$. Taking the amplitude of the nonequilibrium oscillations from Section 4.2, we find that the resulting

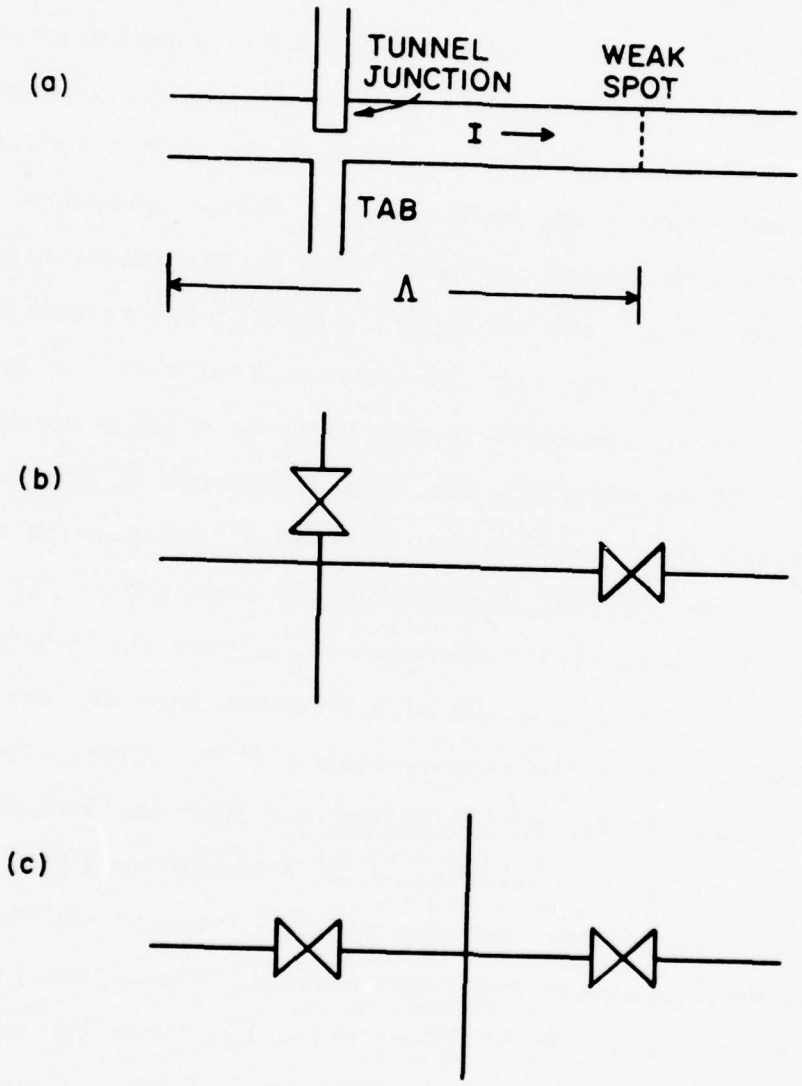

Fig. 5.1 Detection scheme for charge imbalance waves near a PSC. a) Physical picture. b) Schematic. c) Equivalent of b), emphasizing the similarity with the configuration for investigating coupled microbridges.

step size is at best several percent of the tunnel junction critical current for any reasonable set of parameters. This is small, but it should still be observable. Furthermore, a closely-spaced array of such tunnel junction probes would indicate directly the decay length of the charge imbalance waves, and thus distinguish this effect from that due to any possible microwave coupling between the PSC and the tunnel junctions.

A number of other issues should be addressed in connection with this proposed experiment. First, the current in the tunnel junction will include not only a supercurrent but also a quasiparticle current (which corresponds to a shifted potential due to the presence of a time-averaged charge imbalance in the strip), which if large might mask the desired effect. This can be minimized by making the upper electrode out of a material with a higher T_c than that of the strip, which will be just below its own T_c. Secondly, the phase difference $\Delta\theta$ is dependent not only on time, but on the position along the strip. In analogy to the time domain, this spatial dependence will consist of the sum of a linear part due to the dc supercurrent in the strip, and an oscillatory part due to the waves. If the tunnel junction probe is larger than either the wavelength of the charge imbalance waves or the coherence length $\xi(T)$ (assuming

the presence of a near-critical supercurrent in the strip), then the size of the desired effect will be attentuated. Fortunately, a tunnel junction ≈ 1 μm wide or smaller (within the capabilities of standard photoresist and liftoff techniques) seems to satisfy these requirements for reasonable materials, temperatures, and voltages.

A final point is that it has been assumed that the tunnel junction is acting as a passive probe of the strip, although it will be injecting some current into the strip. Ideally this current will be much smaller than the currents otherwise flowing in the strip. If it is too small, however, then the desired effects would likely be washed out by noise in the tunnel junction characteristics. In the opposite extreme of large injected currents, one can determine the effect of the tunnel junction on the strip by reversing the situation, and using the I-V characteristics of the PSC to probe the disequilibrium caused by the tunnel junction.

The experimental configuration we have been discussing, as indicated in Fig. 5.1b, is topologically equivalent to the configuration in Fig. 5.1c used to investigate the interactions between two closely-spaced microbridges. These experiments[65,67] and others on arrays of microbridges[66] have shown that under certain circumstances the Josephson oscillations of closely-spaced microbridges

will synchronize, i.e. the voltages across the individual bridges tend to lock together. By analogy with the tunnel junction detection scheme, our approach leads us to believe that these effects may be due in part to coupling via charge imbalance waves emitted by the adjacent bridges. Artemenko, Volkov, and Zaitsev[57] have made apparently similar predictions in discussing collective excitations in large arrays of proximity effect bridges, and Lindelof[67] has made similar suggestions. A better understanding of the criteria for coupling between microbridges should assist in the development of arrays of microbridges with potential applications as detectors and transmitters of radiation.

In experiments investigating microbridge coupling, the critical currents of the two microbridges typically have comparable values, so that each has a significant effect on the other, and the treatment becomes somewhat more complicated than the tunnel junction probe discussed earlier. We can present this problem in a tractable form, however, through the use of our transmission line equivalent circuit, in particular the formulas for the finite lengths of transmission line developed in Appendix III. Consider the simplified problem consisting of two PSC's located a distance 2ℓ apart on a uniform strip (Fig. 5.2a), represented in our transmission-line picture by Fig. 5.2b.

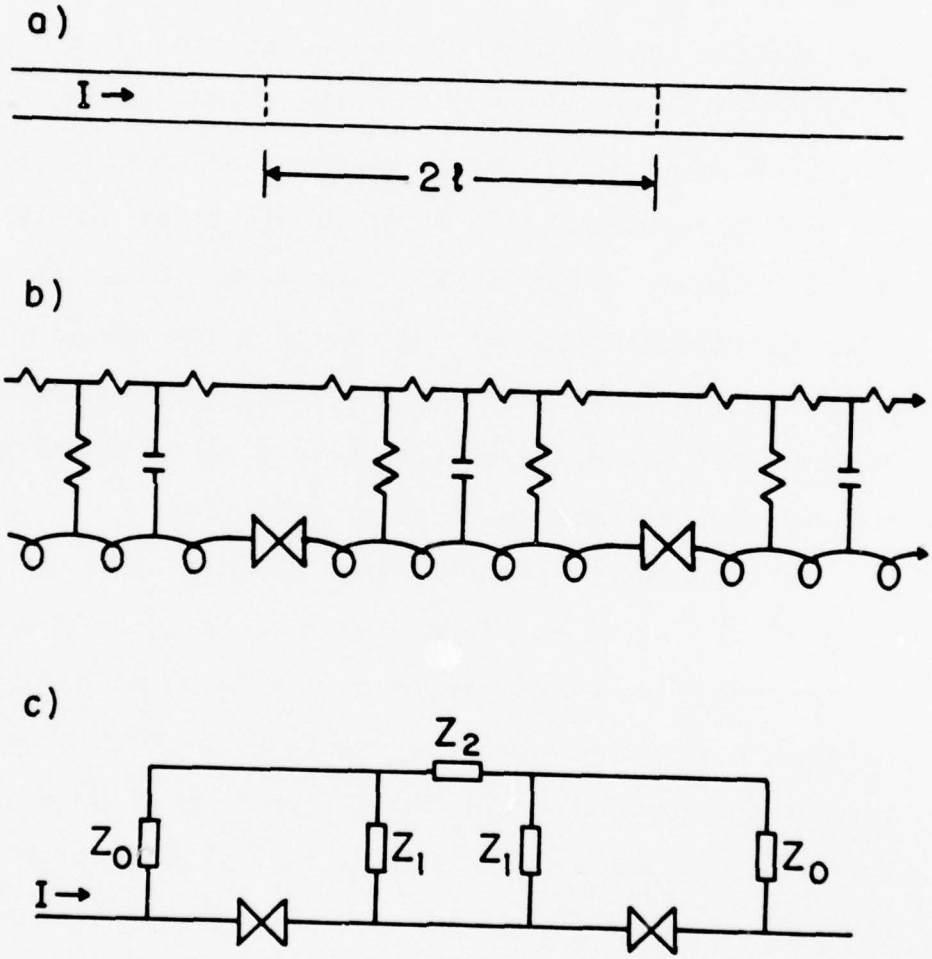

Fig. 5.2 Two interacting PSC's.
a) Superconducting strip with two weak spots (indicated by dashed lines) which act to nucleate PSC's.
b) Transmission-line equivalent of (a).
c) Lumped-impedance equivalent (using the pi-section of Eq. (A3.13)) of the transmission line in (b).

We can relate the currents and potentials at the two Josephson elements by replacing the length of the strip between the two with its lumped impedance equivalent, either the pi equivalent (Fig. 5.2c) or the tee equivalent (Fig. 5.5). The impedances here are the same as those of Eqs. (A3.13) and (A3.14). In general, the currents at one of the Josephson elements will modulate the voltage across the other, and vice versa.

Some simple consequences of these pictures can be seen even without working through the details of the interaction. Consider a string of identical PSC's, each adjacent pair separated by the distance 2ℓ, represented in terms of the tee section equivalent [Eq. (A3.14)] in Fig. 5.3a. By symmetry, the time-averaged voltage $\bar{V}$ across each Josephson element is the same, as is the average normal current $\bar{I}_n$ at each element. Therefore, in Fig. 5.3a, the average current passing through the impedances Z_2' must be zero, and the voltage across each PSC can be expressed as

$$\bar{V} = 2Z_1'(\omega=0,2\ell)\bar{I}_n = 2Z_o(\omega=0)\bar{I}_n \tanh(K(0)\ell)$$

$$= 2\Lambda R\bar{I}_n \tanh(\ell/\Lambda) \qquad (5.1)$$

using Eq. (A3.14), where R is the resistance per unit length and $\Lambda = 1/\sqrt{RG} = K^{-1}(0)$ is the dc decay length. Within the context of the SBT model, Tinkham[54] considered

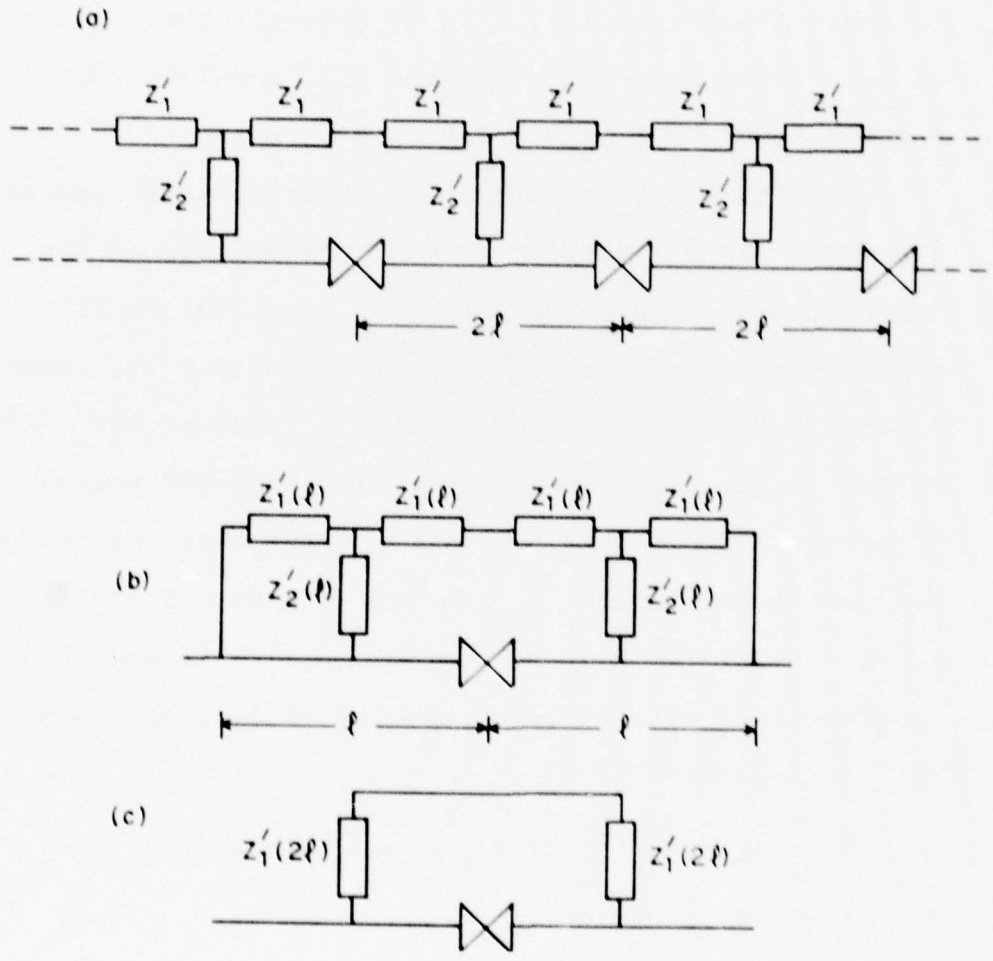

Fig. 5.3 Lumped-element equivalents for a) a long series of closely-spaced PSC's, and b) a single PSC in a short filament (length 2ℓ), using the tee section [Eq. (A3.14)]. c) The equivalent of (b), from Eq. 5.3.

the similar problem of an ideal uniform filament of length L, with n identical PSC's distributed evenly along its length. This corresponds to a separation of $2\ell = L/n$ between adjacent PSC's, with a distance $\ell = L/2n$ between the end of the filament and the initial (or final) PSC. By symmetry the nonequilibrium potential $\Phi = 0$ half-way between each pair of adjacent PSC's, and if we take the boundary condition at the end to be $\Phi = 0$ as well (the "banks" are maintained in equilibrium), then the voltage across each PSC is equal to that in Eq. (5.1), and the total voltage across the entire filament is

$$\bar{V}_T(n) = 2\Lambda nR\bar{I}_n \tanh[L/(2n\Lambda)] \quad . \qquad (5.2)$$

This is the same as Eq. (1) of ref. 54, derived from direct consideration of the equations for the SBT model.

Another problem that can be treated rather simply within the transmission-line picture is that of a single PSC in a filament of finite length, represented in Fig. 5.3b by a tee section equivalent for the length ℓ on either side of a Josephson element. By direct calculation we can show that

$$Z_1'(\ell) + [Z_1'(\ell) \,\|\, Z_2'(\ell)] = Z_o \tanh(K\ell) = Z_1'(2\ell), \quad (5.3)$$

(+ and $\|$ refer to the series and parallel combination of the impedances), so that we can represent the problem

by Fig. 5.3c, which shows a Josephson element shunted by an impedance

$$Z_s = 2Z_1'(2\ell) = 2Z_o \tanh(K\ell). \qquad (5.4)$$

(Note that in dc $\bar{V} = Z_s \bar{I}_n$ reduces to the result in Eq. (5.2) for n=1, as it should.) We can then proceed to solve the problem using the methods of Appendix II and Chapter IV. In Fig. 5.4 we have plotted the resulting I-V curve and its derivative ($dI/d\bar{V}$ vs. $\bar{V}$) for the same parameters as curve b of Fig. 4.8 (linear $f(\Delta\theta)$, $\omega_c\tau_o=2.2$, $\tau_E/\tau_o=11$) and using $2\ell = \Lambda$. The I-V curve is not particularly striking, but its derivative shows a series of sharp features. Their physical origin can be seen from the following discussion.

In a PSC in a long filament, charge imbalance waves propagate out from the center and decay in a distance of order Λ. If the filament is not so long, the waves reach the end before having decayed completely to zero, and partially reflect back due to the impedance mismatch at the boundary. They can then interact back on the Josephson element in the center. In general they will be phase-shifted relative to the waves then being generated, with the greatest effect occuring when they are either in phase or 180° out of phase. These resonance conditions correspond to a finite number of wavelengths or half-wavelengths contained in the length 2Λ, and lead to

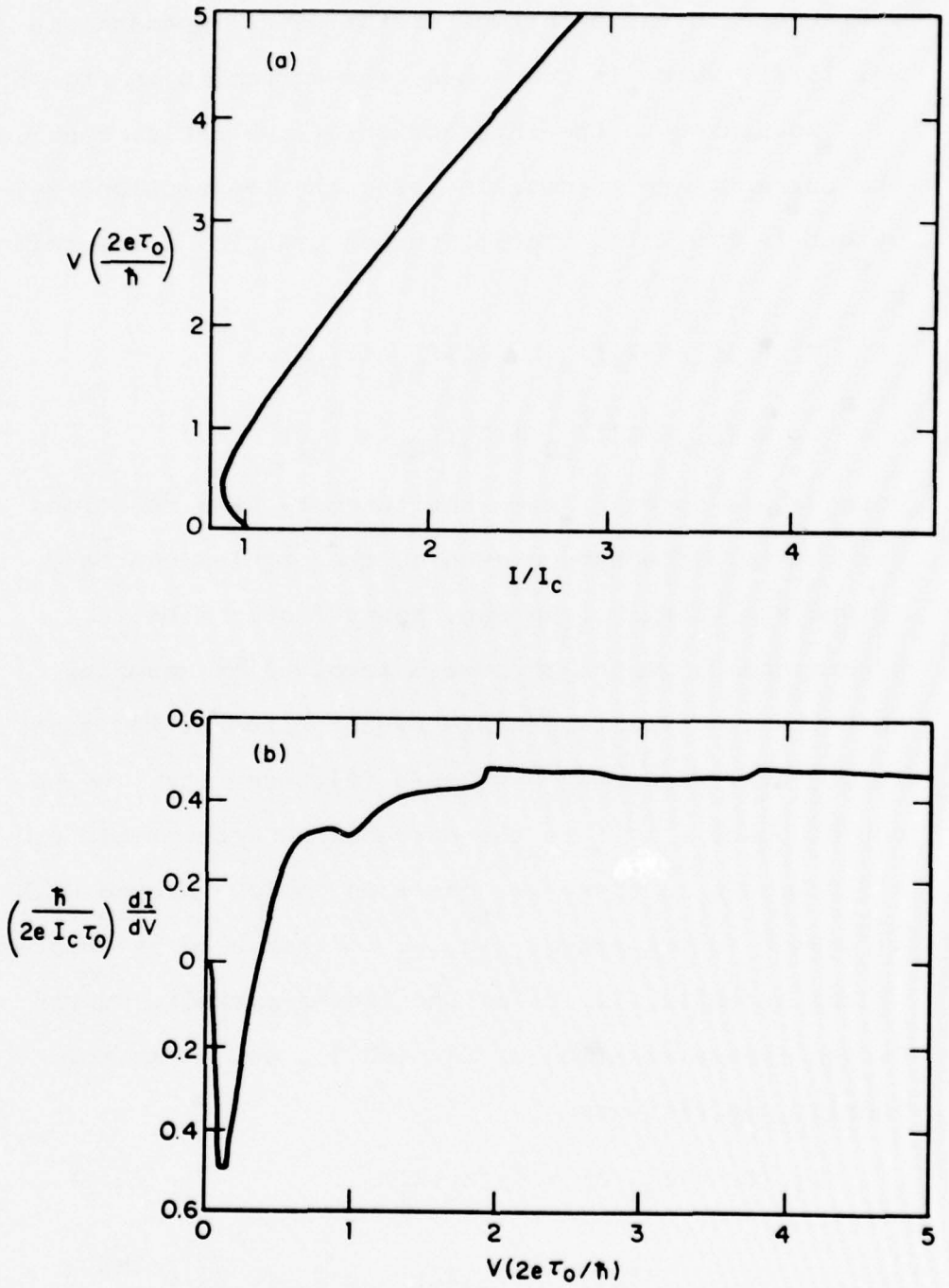

Fig. 5.4 Electrical characteristics of a PSC in a strip of length $2\ell = \Lambda$, with the same parameters as for curve b of Fig. 4.8. a) $\bar{V}$ vs. I. b) $dI/d\bar{V}$ vs. $\bar{V}$.

variations in the magnitude of the shunt impedance in Eq. (5.4), which in turn cause the structure in Fig. 5.4.

Returning to the interaction of two PSC's, consider the currents and potentials using the tee section equivalent in Fig. 5.5. Their Fourier transforms are related by

$$\begin{aligned} \tilde{V}_1 &= (Z_o + Z_1')\tilde{I}_{n1} + Z_2'(\tilde{I}_{n1} - \tilde{I}_{n2}) \\ \tilde{V}_2 &= (Z_o + Z_1')\tilde{I}_{n2} + Z_2'(\tilde{I}_{n2} - \tilde{I}_{n1}) \end{aligned} \quad . \tag{5.5}$$

Using these together with the current-phase relations for the two Josephson elements, the problem can be solved numerically. We can, however gain a better understanding of the phenomena involved by assuming that the two oscillators are synchronized at the same fundamental frequency $\Omega = 2e\bar{V}/\hbar$ (although they may be out of phase), so that the currents and potentials are all periodic in time. We can then follow through with a Fourier series method similar to that used in Chapter IV and Appendix II. Using the linear-periodic supercurrent-phase relation of Eq. (A2.3), we obtain the Fourier coefficients

$$\tilde{I}_{n1}(0) = \tilde{I}_{n2}(0) = \bar{V}/(Z_o+Z_1') \tag{5.6}$$

$$\tilde{I}_{n1}(m\Omega) = \frac{\frac{I_{c1}}{2\pi i m}\left(1 + \frac{I_{c2}Z_T}{2\pi i m\bar{V}}\right) + \left(\frac{I_{c2}}{2\pi i m}\right)^2 \frac{Z_2'\, e^{-im\Omega t_o}}{\bar{V}}}{\left(1 + \frac{I_{c1}Z_T}{2\pi i m\bar{V}}\right)\left(1 + \frac{I_{c2}Z_T}{2\pi i m\bar{V}}\right) - \left(\frac{I_{c1}Z_2'}{2\pi i m\bar{V}}\right)\left(\frac{I_{c2}Z_2'}{2\pi i m\bar{V}}\right)} ,$$

$$m \neq 0, \tag{5.7}$$

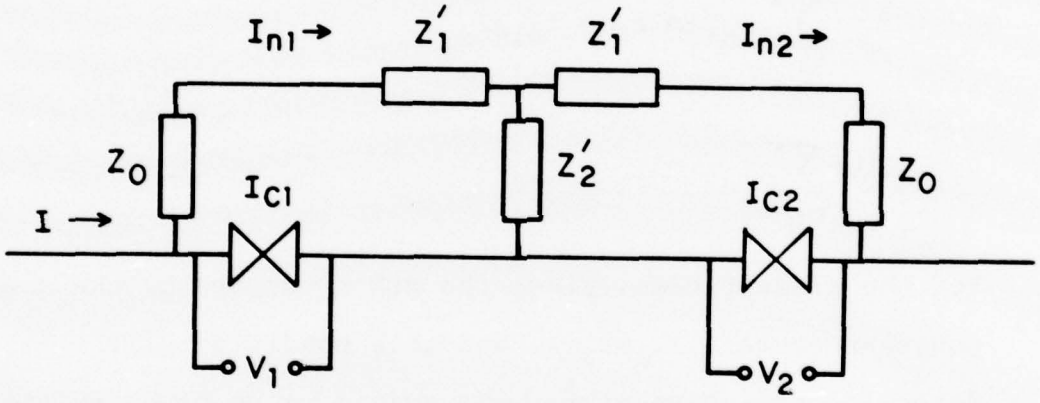

Fig. 5.5 Lumped-element equivalent for two interacting PSC's, separated by a distance 2ℓ, using the tee section [Eq. (A3.14)].

phase-slip center in a long filament).

where

$$Z_T = Z_o + Z_1' + Z_2' = Z_o[1 + \coth(2K\ell)] \qquad (5.8)$$

and the constant t_o is the time lag between the phase-slip events at the two Josephson elements. The expression for $\tilde{I}_{n2}(m\Omega)$ takes the same form but with I_{c1} and I_{c2} interchanged and $e^{-im\Omega t_o}$ replaced with $e^{+im\Omega t_o}$.

The total current at each element is equal to [as in Eq. (4.33)]

$$I_1 = \sum_{m=-\infty}^{\infty} \tilde{I}_{n1}(m\Omega) + I_{c1}/2$$

$$I_2 = \sum_{m=-\infty}^{\infty} \tilde{I}_{n2}(m\Omega) + I_{c2}/2 \qquad (5.9)$$

For the present case, since the PSC's are fed by the same constant current, $I_1=I_2=I$, and this condition will determine the value of t_o. If such a value of t_o exists, then a solution with the two oscillations synchronized ("voltage locking") is possible. If $I_{c1}=I_{c2}$ the two oscillations will always be synchronized, but if they differ by even a small amount then this voltage locking may be restricted to certain currents and separations. We may obtain an estimate of the strength of this voltage locking by considering Eq. (5.7) as the sum of two terms, and examining the second term which contains the parameter t_o which can be adjusted to achieve coupling. Taking for

simplicity m=1 and $I_{c1}=I_{c2}$, the absolute value of this term reduces to the expression

$$F(\bar{V},\ell) = I_c \Big/ \left| 4\pi^2 \frac{\bar{V}}{I_c Z_o(\Omega)} \sinh[2K(\Omega)\ell] - \right.$$

$$\left. - \frac{I_c Z_o(\Omega)}{\bar{V}} \cosh[2K(\Omega)\ell] \right| \qquad (5.10)$$

which is plotted in Fig. 5.6 as a function of $\bar{V}$ for a separation $2\ell = 0.5\Lambda$ and the parameters $\omega_c\tau_o = \omega_c\tau_E = 20$ [see Eq. (4.7)]. Where this function is large, voltage locking should occur over a wider range of critical currents I_{c1} and I_{c2}. The periodic peaks (after the first one) correspond to a resonance condition similar to that discussed earlier for the single PSC; the two junctions create an effective resonant cavity between them.

This type of multiple-peak structure in the strength of voltage locking is reminiscent of qualitatively similar structure seen by Jillie *et al.*[65] in the behavior of their pairs of In microbridges. Although the experimental situation was somewhat more complicated than our idealized problem, and the quantities being compared are actually different, our preliminary results are encouraging, and further work may be expected to clarify the picture.

coupled microbridges.

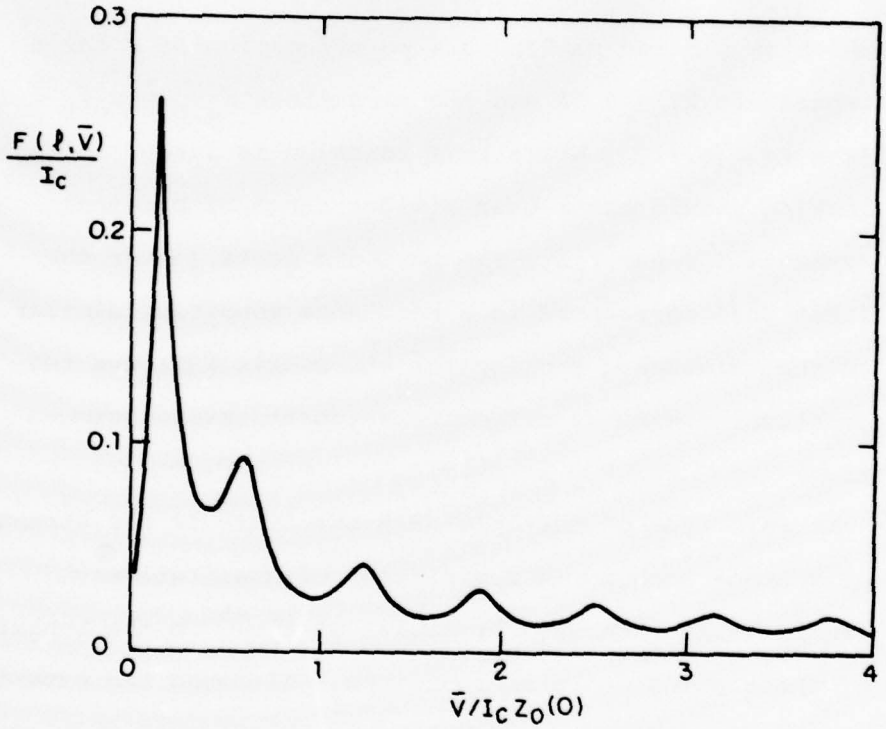

Fig. 5.6 Voltage-locking function $F(\bar{V},\ell)$ [Eq. (5.10)] vs. $\bar{V}$ for two interacting PSC's separated by a length $2\ell = \Lambda/2$, using parameters $\omega_c\tau_o = \omega_c\tau_E = 20$.

5.2 Unexplained Features of Microbridges in Magnetic Fields

We emphasized in Chapter II the importance of the localized weak spot in extending the range of useful data undistorted by heating, essentially because of the reduction in the local critical current relative to that of the uniform strip. As we noted in Section 2.5, this decrease in I_c was strongly dependent on the magnitude and the direction of the applied magnetic field (within the plane of the film). For H perpendicular to the current density J, the relative "weakness" of the weak spot corresponded to a simple decrease in the local cross-sectional area. For $H \| J$, however, it was far weaker than this would indicate. We speculated in Section 2.5 that this difference may have been due to the presence of a field component perpendicular to the surface at the weak spot, because of its geometry (see Fig. 2.2). Other orientations would presumably cause effects between these two limits, although these measurements were not carried out, in part because the changes in orientation required rotating the sample at room temperature (the magnet rotation was used to orient the field parallel to the film).

The depression of I_c for $H \| J$ consisted of two basic effects. First, the local critical temperature $T_c(H)$ at the weak spot, as determined by the temperature

at which I_c went to zero, was depressed below the value for the uniform strip (as indicated by the other PSC's). This "extra" depression of $T_c(H)$ increased as H^2, or what is equivalent, the critical field curves for both the uniform strip and the weak spot fit the form

$$H_{c\|}^2(T) = 1.44\ H_{c\|}^2(0)\ (1-T/T_c) \qquad (5.11)$$

but for different values of $H_{c\|}(0)$, with that for the weak spot being typically 10% less. It is not clear whether this behavior can be reconciled with the suggestion about a perpendicular component of field, inasmuch as $H_{c\perp}(T)$ (rather than its square) should be linear in temperature. In this regard, Tinkham has made an alternative suggestion[69] that the properties of the weak spot might be related to an enhanced value of the parallel magnetic field at the weak spot, due to the partial Meissner effect in the thin film.

Secondly, even after its onset, the critical current of the weak spot for H ||J increased substantially more slowly as the temperature was lowered than that of the uniform film. The Ginzburg-Landau expression for the critical current of a uniform film in a parallel field can be written as[68]

$$I_c(T,H) = I_c(T,H=0)\,[1 - H^2/H_{c\|}^2(T)]^{3/2}$$
$$\propto (1+t^2)^{\frac{1}{2}}\,[1-t^2-h^2(1+t^2)]^{3/2} \qquad (5.12)$$

where $t = T/T_c$, $h = H/H_{c||}(0)$, and in obtaining the latter expression the usual two-fluid temperature dependences of H_{cb} and λ have been used. When re-expressed in terms of $T_c(H)$, I_c varies as $[T_c(H)-T]^{3/2}$, and

$$\frac{dI_c^{2/3}}{dT}\Big|_{T=T_c(H)} \propto (1+h^2)^{1/6}(1-h^2)^{\frac{1}{2}} \qquad (5.13)$$

This was compared with experiment by plotting $I_c^{2/3}$ vs. T near $T_c(H)$, and measuring the slope of the straight line drawn through the points. For both $H \| J$ and $H \perp J$, the data seemed to fit a straight line reasonably, although for the latter case for large fields there was sometimes some minor irregularity or even irreproducibility of I_c as a function of T, perhaps associated with trapped flux. (For comparison, the behavior $I_c \propto [T_c(H)-T]$ has been observed for thin films in a perpendicular field.[70]) In Fig. 5.7, these measured slopes for Sn bridge #29B are plotted as a function of H for the two orientations, together with Eq. (5.13) normalized to the zero-field behavior. Although the results for both orientations differ from the theoretical curve, those for $H \| J$ differ far more. The reduced value of the slope for $H \| J$ reflects the comment made above, that the rate of increase of I_c with temperature below $T_c(H)$ is reduced below the value for the uniform film. This, taken together with the localized depression of

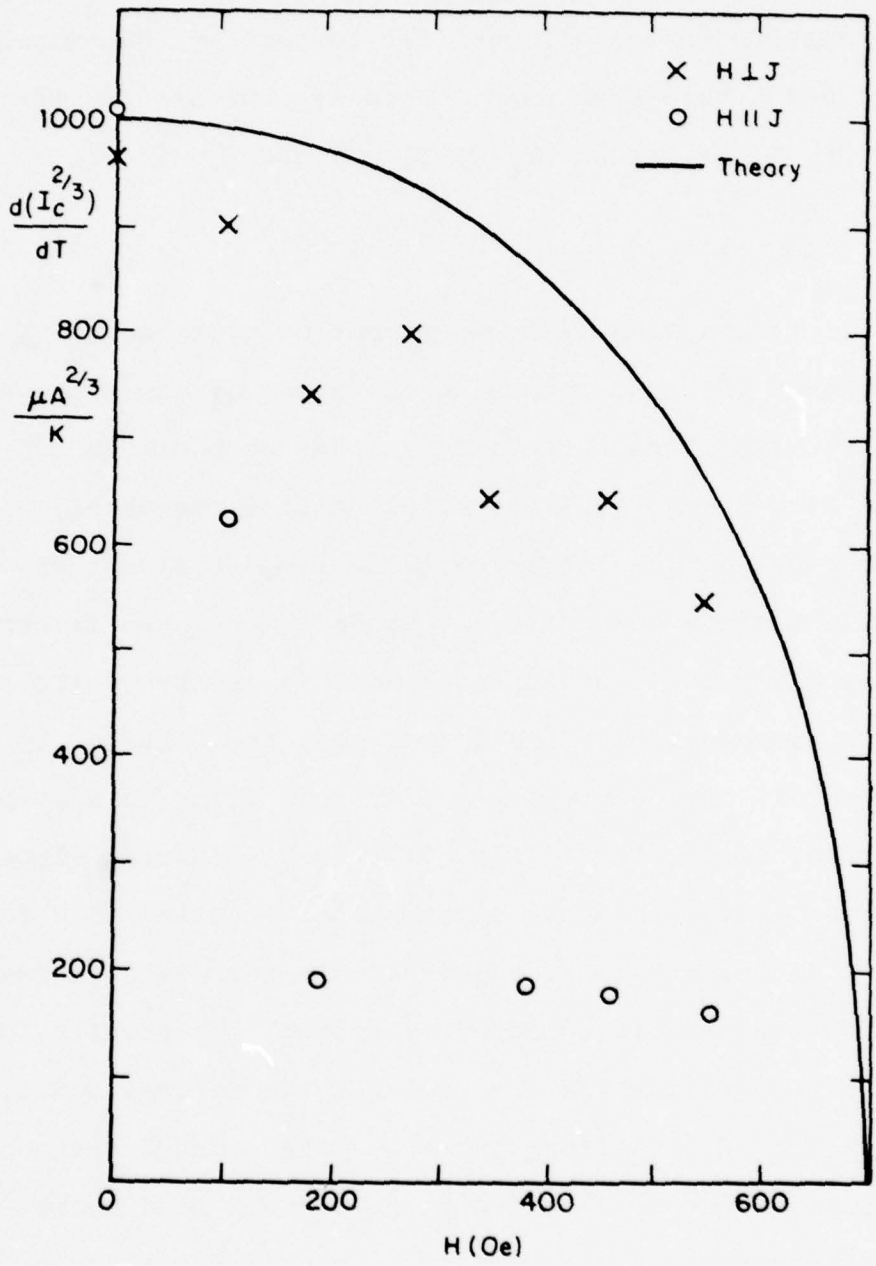

Fig. 5.7 Effect of magnetic field H on I_c for Sn bridge #29B with a weak spot: $d(I_c^{2/3})/dT$ for T near $T_c(H)$, vs. H for the parallel and perpendicular orientations. The theory curve is from Eq. (5.13).

$T_c(H)$, assures that the local value of I_c is well below that for the uniform film, particularly in large fields. The particular mechanism for this effect remains to be elucidated.

Another class of features which we sometimes observed in bridges with magnetically weakened spots is illustrated in Fig. 5.8. As the temperature was lowered to significantly below $T_c(H)$, a low resistance "foot" seemed to develop for currents just above the critical current. (This is the reason for some of the anomalously small values of R_n in Fig. 2.6.) The part of the curve for somewhat higher voltages seemed not to change very much over the same temperature interval, and our supposition is that this upper region represents the usual PSC behavior. In the sample for which the data in Fig. 5.8 was taken, this "foot" disappeared for large fields, and for small fields the corresponding temperature regime was dominated by heating effects. The exact form of this anomalous low-voltage behavior, which was most prominent in those samples with the "weakest" weak spots, varied from sample to sample, so that it may reflect the particular geometry of the weak spot. It is speculated that perhaps these features may be effectively a short microbridge phenomenon. Qualitatively similar features were observed by Octavio in the I-V characteristics of Sn variable-thickness microbridges in zero magnetic field.[71]

Fig. 5.8 I-V characteristics for Sn bridge #29B for H = 190 Oe (||J), showing the development of a low-voltage foot. The temperatures corresponding to the curves are: A 3.620 K; B 3.606; C 3.592; D 3.579; E 3.564; F 3.543; G 3.497; H 3.450; I 3.415; J 3.380; K 3.345; L 3.313; M 3.285; N 3.258; O 3.236; P 3.212; Q 3.182; R 3.163.

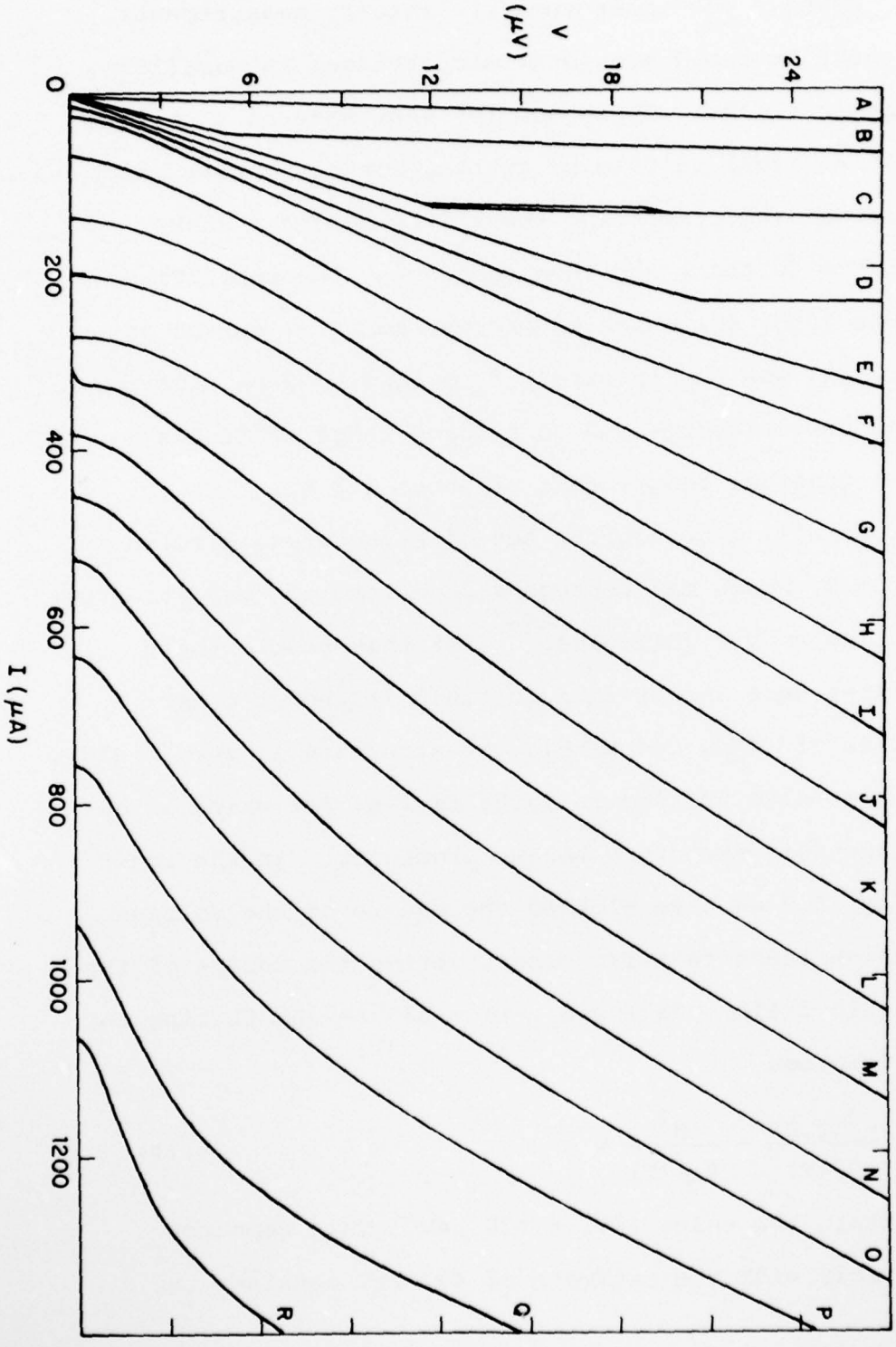
V (μV)
0
6
12
18
24
I (μA)
0
200
400
600
800
1000
1200
A
B
C
D
E
F
G
H
I
J
K
L
M
N
O
P
Q
R

Fig. 5.8

We have also made some preliminary measurements on short Sn two-dimensional microbridges in parallel magnetic fields. These samples were made on a uniform (1000 Å thick) Sn film by cutting with the sharp point of a diamond knife, lifting the knife, moving a short distance further, and then continuing the cut. Tin bridge #35S, for which we present some I-V curves in Fig. 5.9, was approximately 2 μm long by 2 μm wide. These curves correspond to a large range of fields for a constant temperature of about 3.2 K.

We will focus on the set of structures, circled in Fig. 5.9, which may represent some form of "gap structure" occuring at $V = 2\Delta(T,H)/e$.[72] For this sample these features were absent in zero field (although other samples did show comparable gap structure in zero field), and were also lacking in large fields, for which a low-voltage foot structure became prominent. In the inset of Fig. 5.9 we have plotted the square of the voltage at which these features occur, versus the square of the magnetic field. Taking $H_{c||}(T) = 545$ Oe and fitting to the relation

$$\frac{\Delta^2(T,H)}{\Delta^2(T)} + \frac{H^2}{H_{c||}^2(T)} = 1 \qquad (5.14)$$

we obtain the value $\Delta(T) = 420$ μeV. This compares favorably with the estimate of 402 μeV obtained by

Fig. 5.9 I-V characteristics of short Sn bridge #35S (for T = 3.2 K), showing the development of possible gap structure (indicated by small dashed circles). The values of the magnetic field are: A 600 Oe; B 580; C 560; D 550; E 540; F 530; G 520; H 510; I 500; J 490; K 480; L 470; M 460; N 450; O 440; P 420; Q 400; R 380; S 360; T 330 Oe. The inset shows a straight-line fit for a plot of the square of the voltage V_Δ at which this structure appears vs. H^2 [see Eq. (5.14)].

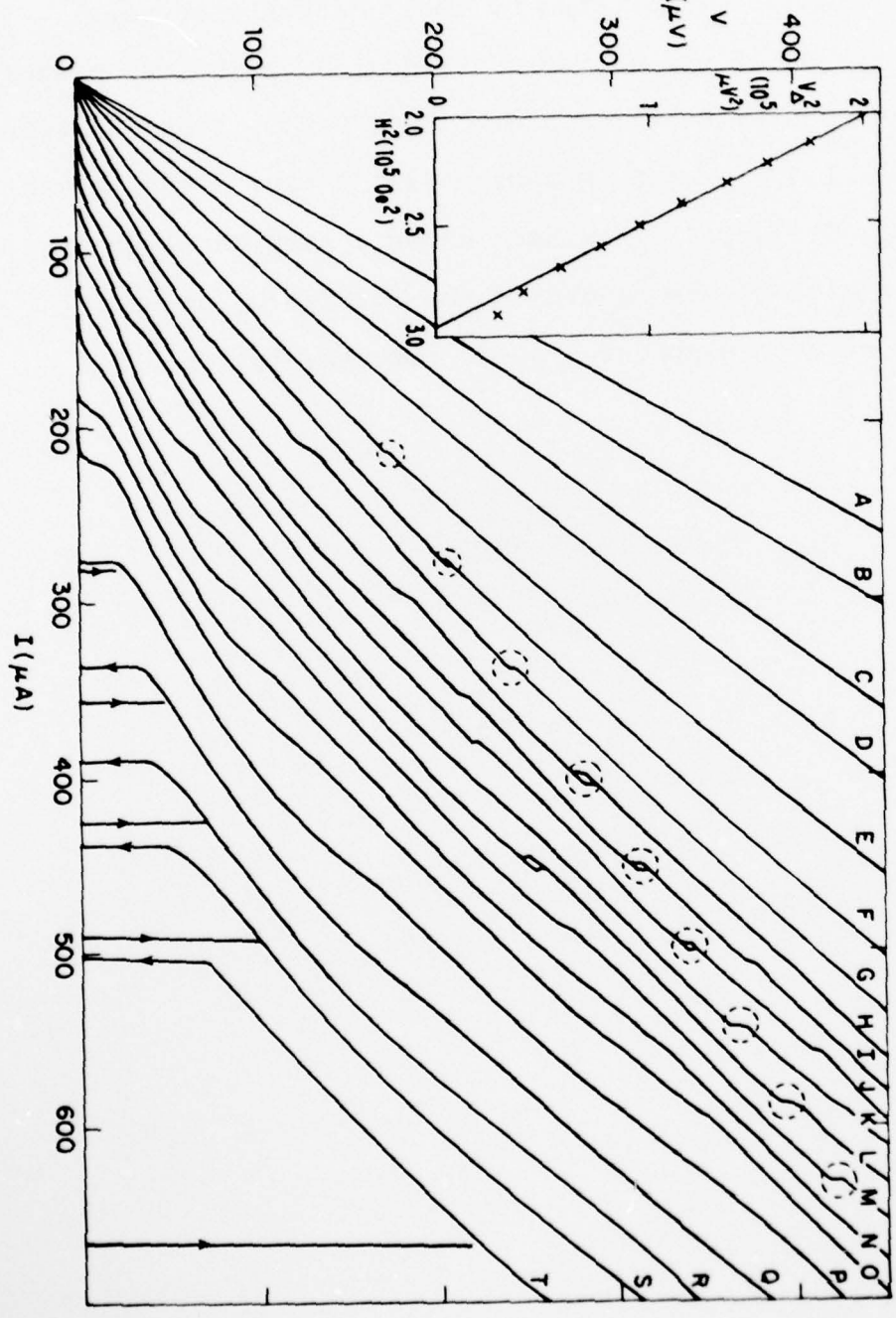

Fig. 5.9

using

$$\Delta(T) = 1.74\ \Delta(0)(1-T/T_c)^{\frac{1}{2}} \qquad (5.15)$$

together with the values T_c = 3.81 K and T = 3.20 K. If these features were in fact due to gap structure, a study of their behavior over a wide range of temperatures might help provide some insight into the origins of this kind of structure in zero field.

The behavior of the small microbridges which we examined tended to differ substantially from sample to sample, a problem that was also present in the low-voltage behavior of long bridges with weak spots. This may be due in part to the difficulty of fabricating reproducible geometries on this small scale with the diamond-knife technology. A change to some sort of microlithographic fabrication therefore seems desirable.

CHAPTER SIX: SUMMARY AND CONCLUSIONS

The seemingly simple problem of the current-induced breakdown of superconductivity in a quasi-one-dimensional filament has turned out to have a great deal of structure and richness, and its investigation has provided major insights into a whole range of related phenomena. As the current through the filament is increased, the voltage increases in a series of steps alternating with plateaus of approximately constant differential resistance. As was demonstrated by Skocpol, Beasley, and Tinkham,[1] this behavior corresponds to the successive onset of localized dissipative units known as phase-slip centers. In the research which we have reported on here, we have continued the earlier work of SBT, extending and confirming their model of PSC's in superconducting filaments, in both its experimental and its theoretical aspects. After reviewing briefly the SBT model and discussing some of the questions which this earlier work left unanswered, we summarize the present work, emphasizing the progress that has been made in the understanding of PSC's. Finally, we conclude with a brief discussion of some of the major implications of our work for future research in the field.

Within the context of the SBT model, a PSC is a localized dynamic nonequilibrium state, which retains its

ability to carry a time-averaged supercurrent while supporting a dissipative normal current. It was assumed that the problem could be separated into the phase-slip process per se, restricted to a core region on the scale of the coherence length ξ, and the diffusion of non-equilibrium quasiparticles, occuring on the larger scale of Λ, the diffusion length corresponding to an appropriate quasiparticle relaxation time (as originally proposed, the normal-state electron-phonon time τ_E). SBT used a particular form for the oscillations in the core, but all that it essential is that the time-averaged supercurrent $\bar{I}_s$ is depressed at the core, so that an interconversion between supercurrent and normal current occurs over the scale of Λ. The time-averaged voltage $\bar{V}$ across the PSC is then proportional to $\bar{I}_n$ at the core, with the proportionality constant being the normal resistance R_n of a length 2Λ of the filament. If $\bar{I}_s$ at the core is a constant fraction of the critical current I_c, then the differential resistance $d\bar{V}/dI$ of the PSC has this constant value R_n, in agreement with the observation of a constant slope in the plateau region of the I-V curves. The voltage profile over the scale of Λ consistent with this picture involves a sudden jump in the condensate potential $\bar{\mu}_s$ at the core, and an exponential decay of the quasiparticle potential $\bar{\mu}_n$ to the

value of $\bar{\mu}_s$ over the length Λ, as was confirmed by Dolan and Jackel[19] with normal and superconducting probes near a PSC.

Notwithstanding a substantial amount of experimental evidence, the SBT model was largely unsupported by theory at the time that it was proposed. The nature of the diffusion length and the corresponding relaxation time were somewhat uncertain, as was the connection between the PSC and other experiments involving non-equilibrium potential differences in superconductos, such as the quasiparticle injection experiment of Clarke.[13] Another question was whether the model really required the strict separation of length scales, inasmuch as some of the strongest experimental support came from tin samples in a range where $\Lambda \approx 3\xi$. SBT left open the issue of time-dependent processes outside the core, dealing only with time averages in the region. They were also unspecific with regard to the shape of the voltage step associated with the onset of the PSC, which varied experimentally from rounded through steep to hysteretic. Although the importance of dissipative heating in producing hysteresis was emphasized by Skocpol et al.[1,46] the possibility remained of some intrinsic hysteresis in the regime very close to T_c. The question of interactions between multiple PSC's was also not explicitly pursued in the

original SBT paper, although Tinkham has since described the dc interactions which follow from the model.[54] Finally, it was unclear whether the SBT picture of PSC's in a superconducting filament could be extended to include the presence of pair-breaking perturbations such as a magnetic field. We have tried to respond to many of these questions in our research, and to clarify the issues for those problems we could not resolve.

In the course of developing the theoretical background for the phase-slip center, we have emphasized the centrality of the concept of charge imbalance (or branch imbalance) to all phenomena involving the existence of a nonequilibrium potential difference in a superconductor. Basically, this is because a charge imbalance is the net excess charge density in the quasiparticles, and to maintain overall neutrality the condensate must respond by shifting its own chemical potential. Charge imbalance can be generated not only by quasiparticle injection, but also by the net influx of normal current, which transports quasiparticle charge. By working within the context of recent generalized two-fluid theories of nonequilibrium superconductors,[24] which are rigorously valid in the limit of small Δ/k_BT, we have obtained equations describing the dynamics of charge imbalance in nonequilibrium superconductors. One consequence of this approach is

the prediction, still experimentally unverified, that a homogeneous charge imbalance will decay to zero exponentially with a relaxation time τ_E, rather than the "branch imbalance relaxation time" τ_{Q^*} which was introduced by Tinkham and Clarke[9] for the dc quasiparticle tunnel injection experiment. These equations are exactly equivalent to those describing electrical signals propagating down a classical transmission line, where the two channels of the line represent the condensate and quasiparticle channels for the flow of current, and the shunt conductance between the two lines represents conversion processes via charge imbalance decay. These equations and the associated transmission line form a unified framework for dealing with the whole gamut of phenomena involving charge imbalance. The charge imbalance waves which propagate down the superconducting filament have a decay length whose low-frequency limit is $\Lambda_{Q^*} = \sqrt{D\tau_{Q^*}}$. This quasiparticle diffusion length thus characterizes the exponential decay of normal current on the superconducting side of a current-carrying normal-superconducting boundary. For high frequencies, these charge imbalance waves correspond to the propagating collective mode observed in superconducting fluctuations by Carlson and Goldman.[23]

We have also used this transmission-line equivalent

to develop a new model for a phase-slip center. The Josephson oscillations connected with the phase-slip process in the core act to generate charge imbalance waves which propagate out in both directions along the filament. Continuing for simplicity the separation of length scales contained in the SBT model, we describe these Josephson oscillations in terms of a supercurrent-phase relation for an ideal Josephson element of negligible extent, located on the condensate channel of our transmission line. The effect of the transmission line on the core is equivalent to shunting the Josephson element with an impedance equal to twice the characteristic impedance of the line. The resulting time-averaged behavior reduces essentially to that of SBT, except that now the length Λ is unambiguously identified with Λ_{Q^*}. The I-V characteristics calculated within the model show a low-voltage onset whose shape depends on the characteristic times in the problem, and a high-voltage asymptote with constant differential resistance proportional to Λ_{Q^*}. The onset becomes hysteretic when the effective ac resistance shunting the Josephson element becomes smaller than the dc resistance. Preliminary experimental evidence on this issue is inconclusive, but suggests qualitative and some rough quantitative agreement in tin microstrips and whiskers. With pairs of closely-spaced PSC's, the model predicts that

the charge imbalance waves emitted by each junction will modulate the voltage driving the other, leading to the possibility of "voltage locking" or synchronization of the Josephson oscillations. Other effects similar to resonance are predicted in situations where discontinuities in the wave properties cause reflections of the charge imbalance waves back onto the Josephson element which had earlier emitted them. All these effects can be treated very conveniently using standard formulas for lumped-element equivalents of finite lengths of the transmission line. Again, these predictions are qualitatively similar to certain effects reported in the literature for closely-spaced microbridges, but more work is required to provide a rigorous test of the model.

Our experimental work on tin microstrips in parallel magnetic fields has provided additional evidence that the basic concepts contained in the SBT model of PSC's remain valid well beyond the context in which they were originally proposed. The qualitative behavior of the I-V curves remains the same, but the characteristic resistance level R_n decreases substantially as the field is increased. The approximation of the separation of length scales is then even poorer than in zero field, but if we extract a quasiparticle relaxation time from R_n in the usual way, we obtain general agreement with a

AD-A078 441 HARVARD UNIV CAMBRIDGE MA DIV OF APPLIED SCIENCES F/G 20/3
NONEQUILIBRIUM PHENOMENA IN SUPERCONDUCTING PHASE-SLIP CENTERS.(U)
OCT 79 A M KADIN N00014-77-C-0085
UNCLASSIFIED TR-15 NL

3 OF 3
AD
A078441

END
DATE
FILMED
1-80
DDC

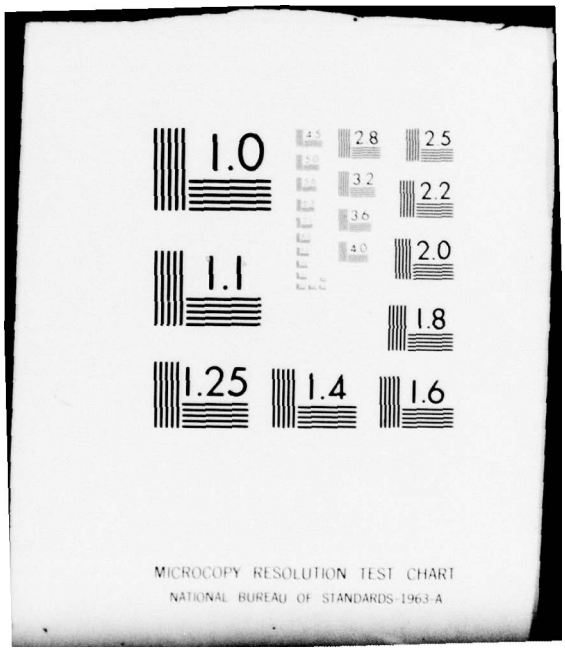
1.0
1.1
1.25
1.4
1.6
1.8
2.0
2.2
2.5
2.8
3.2
3.6
4.0
4.5
MICROCOPY RESOLUTION TEST CHART
NATIONAL BUREAU OF STANDARDS-1963-A

formula derived by Schmid and Schön [12] for the "transverse mode" relaxation time in the presence of pair-breaking (produced by the magnetic field). Since this transverse mode time is effectively a generalized charge imbalance relaxation time, this agreement provides support for our theoretical analysis of PSC's. The clearest agreement with theory was obtained form our samples containing deliberate weak spots which depressed I_c locally, isolating a single PSC and decreasing heat dissipation $\propto I_c^2 R_n$. The value of R_n diverged weakly as $[T_c(H)-T]^{-\frac{1}{2}}$ at the critical temperature of the uniform strip, rather than at that of the weak spot. This helps confirm the contention that the dc properties of PSC's are relatively independent of the dynamics in the core; the key is the quasiparticle relaxation over the larger scale of Λ. This divergence was not apparent in much of the earlier work with uniform strips in zero field, in part because of the effects of heating in enhancing the apparent resistance level away from T_c. We were able to remove these effects for moderate amounts of heating using the local heating model of Skocpol et al.[1,46], and thereby expand the temperature range near $T_c(H)$ where we could accurately infer the relaxation time. The mechanism for the reduction of I_c at the weak spots remains uncertain, although the magnetic field clearly plays an important part.

Our investigations into superconducting phase-slip centers have helped to clarify the relationships between the I-V characteristics and the nonequilibrium phenomena associated with charge imbalance and heating. At the same time, they have introduced a series of new questions, which provide an agenda for future research in the field. The most important of these relate to the ac properties of PSC's, for which experimental evidence for the theoretical model we have developed is largely lacking. Careful measurement of hysteresis close to T_c in a variety of materials may provide an indirect test, although the presence of heating may complicate the interpretation. More clearcut evidence might be obtained by the observation of resonance-related effects in a single PSC and voltage-locking behavior in accordance with the model in closely-spaced microbridges. Also of significant interest is whether our model can be extended to include the effects of magnetic fields and incident microwave radiation on PSC's and microbridges. In conclusion, the study of the I-V characteristics of superconducting filaments has helped to provide insight into a wide range of nonequilibrium phenomena in superconductors, and will likely continue to do so in the future.

APPENDIX ONE: ELECTRONIC TEMPERATURE REGULATION SYSTEM

The main purpose of this appendix is to provide a brief guide to the operation of our home-made electronic temperature regulator, in case there should be a use for it in the future. In my experiments, for those runs in which the sample was located inside a vacuum can, it was used to provide electronic feedback to regulate the temperature of the copper block on which the sample was mounted. It usually worked quite well, although as it turned out it was generally sufficient to run directly in the liquid He bath, without having to worry about whether the vacuum can was actually sealed.

The circuit functioned basically as a simple thermostat system with electronic feedback. The signal from a temperature sensor was amplified, compared with a thermostat setting, and a correction signal was applied to adjust the power delivered to a heater. A schematic of the circuit is shown in Fig. A1.1. In more detail, the thermometer signal was the voltage across a Cryocal doped germanium resistance thermometer (or earlier an Allen-Bradley resistor) with 4.2 K resistance of order 1 kohm and a negative temperature coefficient, biased with a constant current of 10 μA or less. It was mounted on the same copper block as was the sample and also the heater, which consisted of a length of alloy resistance wire

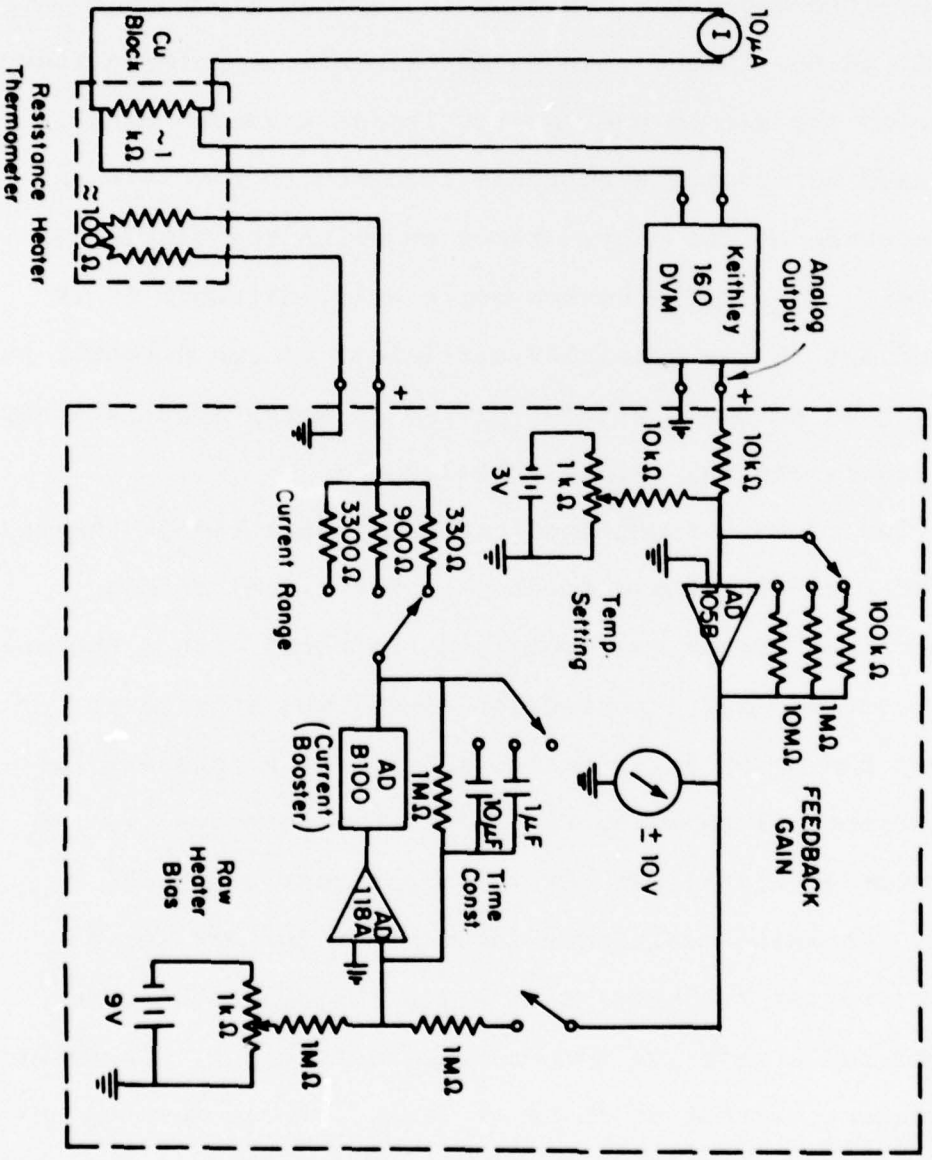

Fig. A1.1 Schematic of temperature control system.

(~100 Ω) wrapped around the block and heat-sunk with GE-7031 varnish. The thermometer voltage was measured with a Keithley model 160 digital voltmeter, and the analog output of the DVM was used to amplify the signal to the 1 volt range (usually by a factor of 100). The difference between this and the thermostat voltage was amplified and added to the raw heater bias voltage, which was then used to supply power for the heater. Because the thermometer had a negative temperature coefficient, the circuit was set up so that an increase in the thermometer voltage caused a proportional increase in the heater current.

The outline of the operating procedure is as follows: First, with the feedback switch open, the bath was pumped down to somewhat below the operating range of temperatures, and the raw heater bias was turned up to yield approximately the desired temperature. The temperature-setting knob was then turned to null the amplified correction signal, and the feedback was then switched in. The feedback would then act to stabilize the temperature at the given value, even while the bath temperature was drifting somewhat. The stability was better than required for these experiments, permitting a drift in the temperature of the copper block of less than about 10 mK per hour. Small adjustments in temperature were made by adjusting the

thermometer setting, and sometimes also the heater bias if the correction voltage got too large. An attempt to make a large change of temperature in this way sometimes led to unstable oscillations. A tendency towards oscillation was sometimes a problem even for a fixed setting, particularly for the larger feedback gains. This may have been due to a time lag in the thermal response of the copper block, causing the heater correction voltage to be out of phase with the temperature. A systematic study of this was not made, but the insertion of a capacitor to slow down the electrical response of the system usually got rid of these oscillations.

Operated in the way described above, the electronic temperature regulation system provided fairly reliable constant temperatures in the range from about 1.5 K to over 4.2 K.

APPENDIX TWO: GENERALIZED RESISTIVELY SHUNTED JUNCTION MODEL

We treat in this appendix the resistively shunted junction (RSJ) model, generalized to allow for a non-sinusoidal supercurrent-phase relation.[50] In particular, we consider an ideal Josephson element which can be described by the supercurrent-phase relation

$$I_s = I_c f(\Delta\theta) \tag{A2.1}$$

where I_c is the critical current and f is some periodic function of the phase difference $\Delta\theta$ across the junction with amplitude one. We will emphasize the classic sinusoidal relation

$$f(\Delta\theta) = \sin(\Delta\theta) \tag{A2.2}$$

and the linear-periodic relation

$$f(\Delta\theta) = \mathrm{mod}(\Delta\theta/2\pi) \tag{A2.3}$$

(mod or modulus is the remainder after the integral part is subtracted off), but unless otherwise noted, the treatment will be valid for a general $f(\Delta\theta)$. As indicated in Fig. A2.1, this junction is shunted by a simple resistance R. This parallel combination is fed with a constant current bias I, and the voltage drop $V = I_n R$ will be a function of time. By the Josephson relation

$$V = \frac{\hbar}{2e}\dot{\Delta\theta} \tag{A2.4}$$

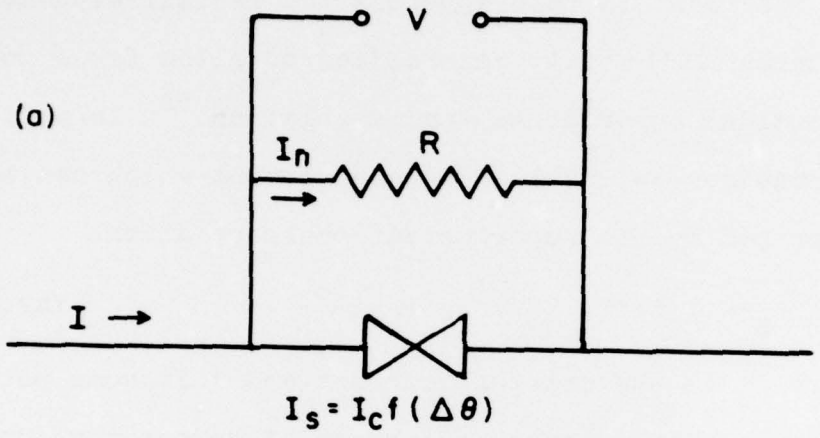

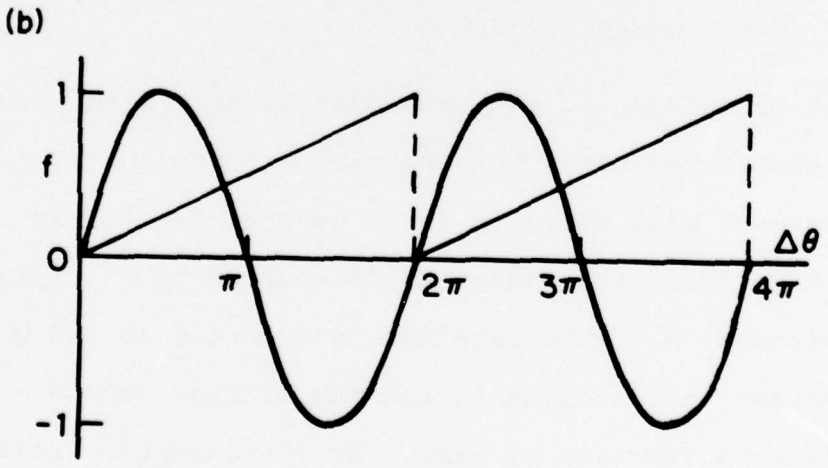

Fig. A2.1 The generalized resistively-shunted junction (GRSJ) model. a) Schematic. b) Two examples of periodic functions $f(\Delta\theta)$ which are permitted in this model for the supercurrent-phase relation [Eqs. (A2.2) and (A2.3)].

we have

$$I = I_s + I_n = I_c f(\Delta\theta) + \frac{\hbar}{2eR}\dot{\Delta\theta} \quad . \qquad \text{(A2.5)}$$

This differential equation can be integrated in the form

$$\int_{\Delta\theta(0)}^{\Delta\theta(t)} \frac{d(\Delta\theta')}{[\frac{I}{I_c} - f(\Delta\theta')]} = \int_0^t \frac{2eI_cR}{\hbar}\,dt' = \frac{2eI_cRt}{\hbar} \quad . \qquad \text{(A2.6)}$$

For the dc I-V relation, we can integrate over an entire period, and using the fact that

$$\Omega \equiv \frac{2\pi}{\tau_J} = \frac{2e\bar{V}}{\hbar} \qquad \text{(A2.7)}$$

(Ω and τ_J are the Josephson angular frequency and period) we obtain

$$\bar{V} = 2\pi I_c R \Big/ \int_0^{2\pi} \frac{d(\Delta\theta)}{[\frac{I}{I_c} - f(\Delta\theta)]} \qquad \text{(A2.8)}$$

For any current-phase relation, this starts out with $\bar{V}=0$ at I_c, rises with vertical slope (taking current as the horizontal axis) and bends over to meet asymptotically the voltage biased line

$$\bar{V} = R(\, I - \langle f \rangle I_c) \qquad \text{(A2.9)}$$

where

$$\langle f \rangle = \frac{1}{2\pi}\int_0^{2\pi} f(\Delta\theta)d(\Delta\theta) \quad . \qquad \text{(A2.10)}$$

Eq. (A2.9) can also be written in the form

$$I = \frac{\bar{V}}{R} + \langle f \rangle I_c \qquad \text{(A2.11)}$$

where the second term, the "excess current", corresponds

to a nonzero constant time-averaged supercurrent for high voltages, provided $\langle f \rangle > 0$. For the particular cases of interest,

$$\begin{cases} \bar{V} = R[I^2 - I_c^2]^{\frac{1}{2}} \\ I = [(\bar{V}/R)^2 + I_c^2]^{\frac{1}{2}} \end{cases}, \quad f(\Delta\theta) = \sin(\Delta\theta) \qquad \text{(A2.12)}$$

$$\begin{cases} \bar{V} = I_c R/\ell n[I/(I-I_c)] \\ I = I_c/[1 - \exp(-I_c R/\bar{V})] \end{cases}, \quad f(\Delta\theta) = \Delta\theta/2\pi. \qquad \text{(A2.13)}$$

These functions are plotted in Figs. A2.2 and A2.3.

The detailed time dependence can also be obtained from Eq. (A2.6). For the two cases,

$$I_s = I_c \sin(\Delta\theta) = I_c \left[\frac{I_c + I\sin\Omega t}{I + I_c \sin\Omega t} \right] \qquad \text{(A2.14)}^{73}$$

$$I_s = I_c \Delta\theta/2\pi = I[1 - \exp(-2eI_c Rt/h)] = I_c \left[\frac{1 - \exp(-(I_c R/\bar{V})(t/\tau_J))}{1 - \exp(-I_c R/\bar{V})} \right], \quad 0 \leq \Delta\theta < 2\pi. \qquad \text{(A2.15)}$$

These are plotted for $I = 1.1\ I_c$ in the insets of Figs. A2.2 and A2.3.

The time-dependent quantities may also be obtained by a Fourier-series method. Although this leaves the solution in the form of an infinite sum, it is more generally applicable to cases where the element shunting

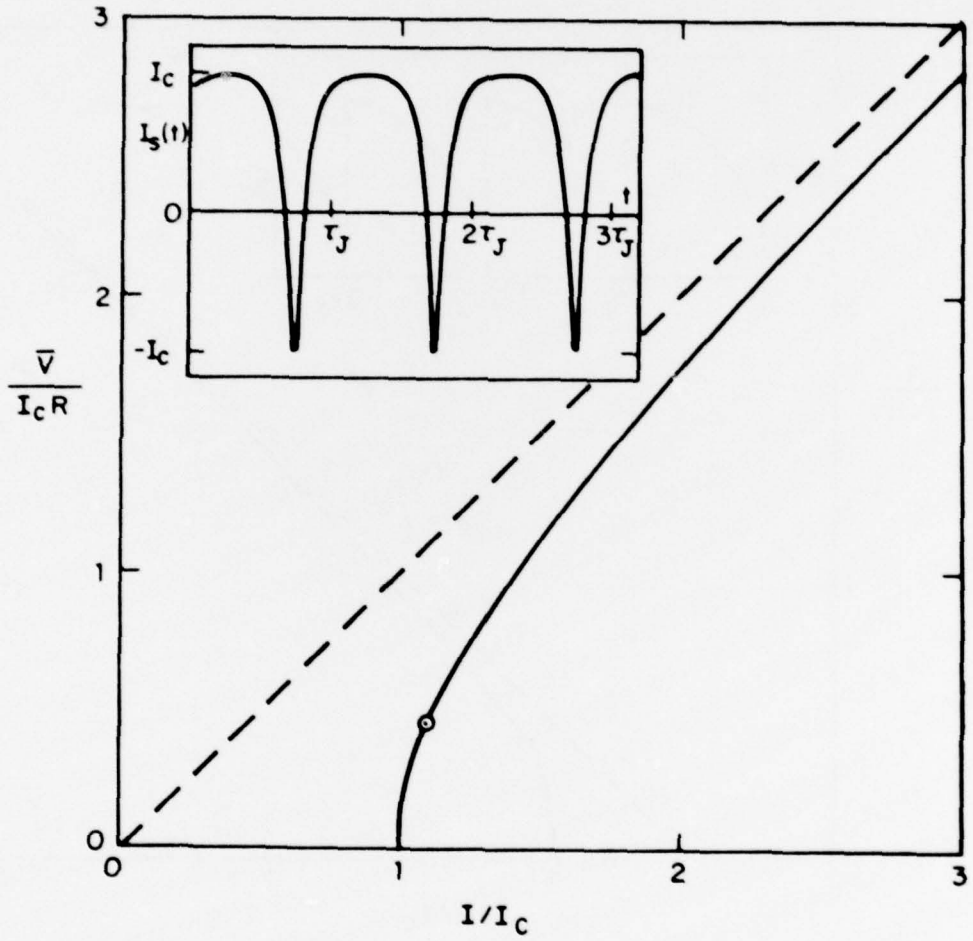

Fig. A2.2 $\bar{V}(I)$ for sinusoidal $f(\Delta\theta)$. The dashed line is the high-voltage asymptote. The inset shows the time dependence of I_s for $I = 1.1\ I_c$, corresponding to the small circle on the $\bar{V}(I)$ curve.

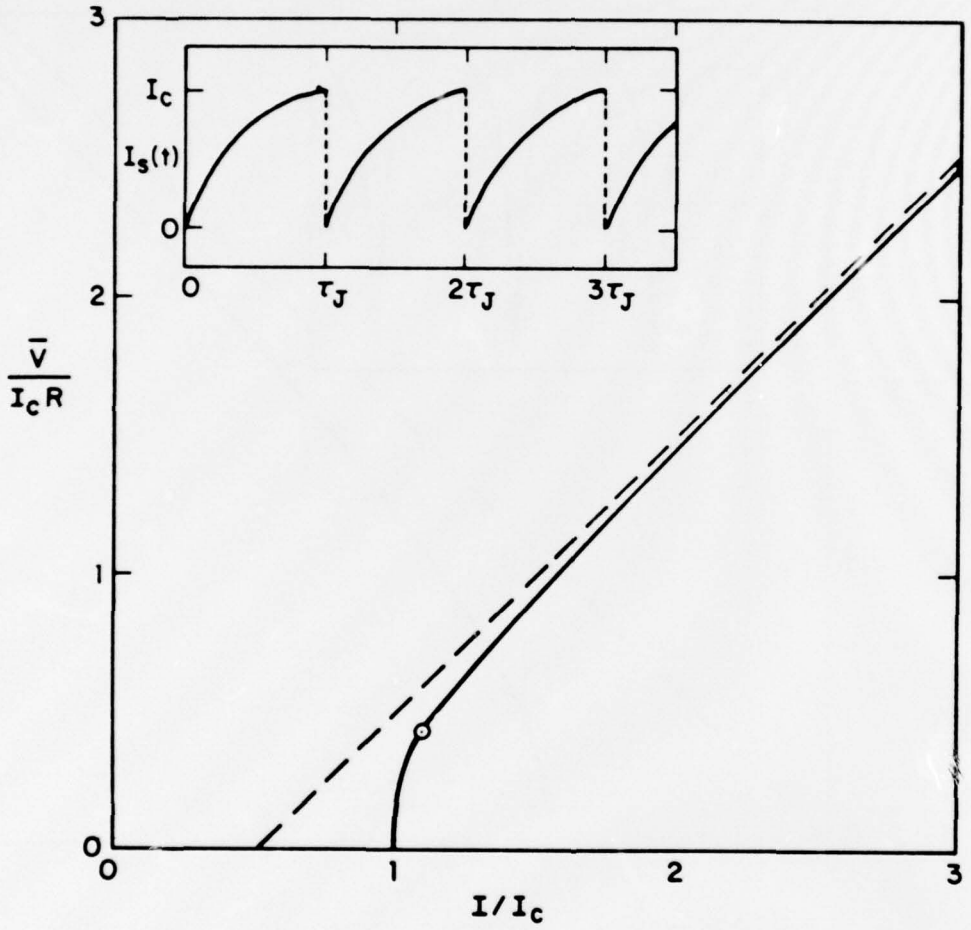

Fig. A2.3 $\bar{V}(I)$ for linear-periodic $f(\Delta\theta)$. The dashed line is the high-voltage asymptote. The inset shows the time dependence of I_s for $I = 1.1\ I_c$, corresponding to the small circle on the $\bar{V}(I)$ curve.

the junction is <u>not</u> a simple resistor (as in Chapter IV). For that reason, we will follow the derivation here for a general shunt impedance $Z_s(\omega)$ [note that the shunt impedance in Chapter IV is denoted by $2Z(\omega)$]. We look for a solution with I_n periodic in time with a fundamental frequency $\Omega = 2e\bar{V}/\hbar$. Expanding in a Fourier series with coefficients c_m, we have

$$I_n(t) = \sum_{m=-\infty}^{\infty} c_m(\Omega)\, e^{im\Omega t} \qquad \text{(A2.16)}$$

where

$$c_o = \bar{I}_n = \bar{V}/Z_s(0) \ , \qquad \text{(A2.17)}$$

and since $I_n = I - I_c f(\Delta\theta)$,

$$c_m = -\frac{\Omega I_c}{2\pi} \int_0^{2\pi/\Omega} dt\, e^{-im\Omega t} f(\Delta\theta(t)), \quad m \neq 0 \ . \qquad \text{(A2.18)}$$

In terms of these coefficients the voltage takes the form

$$V(t) = \frac{\hbar}{2e}\dot{\Delta\theta} = \sum_{m=-\infty}^{\infty} Z_s(m\Omega)\, c_m\, e^{im\Omega t} \qquad \text{(A2.19)}$$

Setting $\Delta\theta(t=0) = 0$ and integrating, we obtain

$$\Delta\theta(t) = \Omega t + \frac{2e}{\hbar} \sum_{m\neq 0} Z_s(m\Omega)\, \frac{c_m}{im\Omega}\, (e^{im\Omega t} - 1). \qquad \text{(A2.20)}$$

Given any relation $f(\Delta\theta)$, Eqs. (A2.18) and (A2.20) provide a formal solution to the problem, which can be evaluated on a computer by iteration (although a solution may not always exist for a complex Z_s). The I-$\bar{V}$ relation can be expressed in the form

$$I = I_n(0) + I_s(0)$$

$$= \sum_{m=-\infty}^{\infty} c_m + I_c[f(\Delta\theta(0^+)) + f(\Delta\theta(0^-))]/2 \qquad (A2.21)$$

where the second term allows for the discontuity of $f(\Delta\theta(t))$ at $t=0$.

If we use the linear-periodic current-phase relation of Eq. (A2.3), an analytic expression for the Fourier coefficients can be obtained. Substituting Eq. (A2.20) into Eq. (A2.18), we obtain

$$c_m = -\frac{\Omega I_c}{4\pi^2}\left[\int_0^{2\pi/\Omega} dt\ \Omega t\ e^{-im\Omega t} + \right.$$

$$\left. + \frac{2e}{\hbar}\sum_{m'\neq 0} Z_s(m'\Omega)\ \frac{c_{m'}}{im'\Omega}\int_0^{2\pi/\Omega} dt\,(e^{im'\Omega t}-1)e^{-im\Omega t}\right]$$

$$= \frac{I_c}{2\pi im} - \frac{I_c}{2\pi im}\frac{2e}{\hbar}\frac{Z_s(m\Omega)}{\Omega}\,c_m\ ,\ m\neq 0\ , \qquad (A2.22)$$

which yields the explicit solution for c_m:

$$c_m = \frac{I_c}{2\pi im}\Big/\left[1 + \frac{I_c}{2\pi im}\frac{Z_s(m\Omega)}{\bar{V}}\right]. \qquad (A2.23)$$

For the resistive shunt, we simply set $Z_s(m\Omega) = R$. Provided that a sufficient number of harmonics are taken, this reproduces the results of Eqs. (A2.13) and (A2.15). The more general form with the shunt impedance is used in Chapter IV.

APPENDIX THREE: FINITE LENGTH AND ARTIFICIAL TRANSMISSION LINES

In this appendix we treat the transmission line of Chapter III for cases involving finite lengths,[74] where the possibility of reflected waves cannot be ignored. We then show how this information can be used to design an artif.cial transmission line, which might serve in analog computations of some of the problems in Chapters IV and V where numerical computations become difficult.

Consider the section of transmission line in Fig. A3.1a of length 2ℓ, between $x = -\ell$ and $x = +\ell$. As in Chapter III, its continuous electrical elements can be characterized by a resistance R per unit length in the upper channel, an inductance L per unit length in the lower channel, and a conductance G and capacitance C per unit length between the two channels. From Kirchoff's laws, the equations governing the evolution of the currents and potentials are

$$\frac{\partial \Phi}{\partial x} = -RI_n + L\dot{I}_s \qquad \text{(A3.1)}$$

$$\frac{\partial I_n}{\partial x} = -G\Phi - C\dot{\Phi} \quad , \qquad \text{(A3.2)}$$

where as before I_n and I_s are the currents in the upper and lower channels respectively and Φ is the potential difference between the two channels. We will be dealing exclusively here with the case of constant total current,

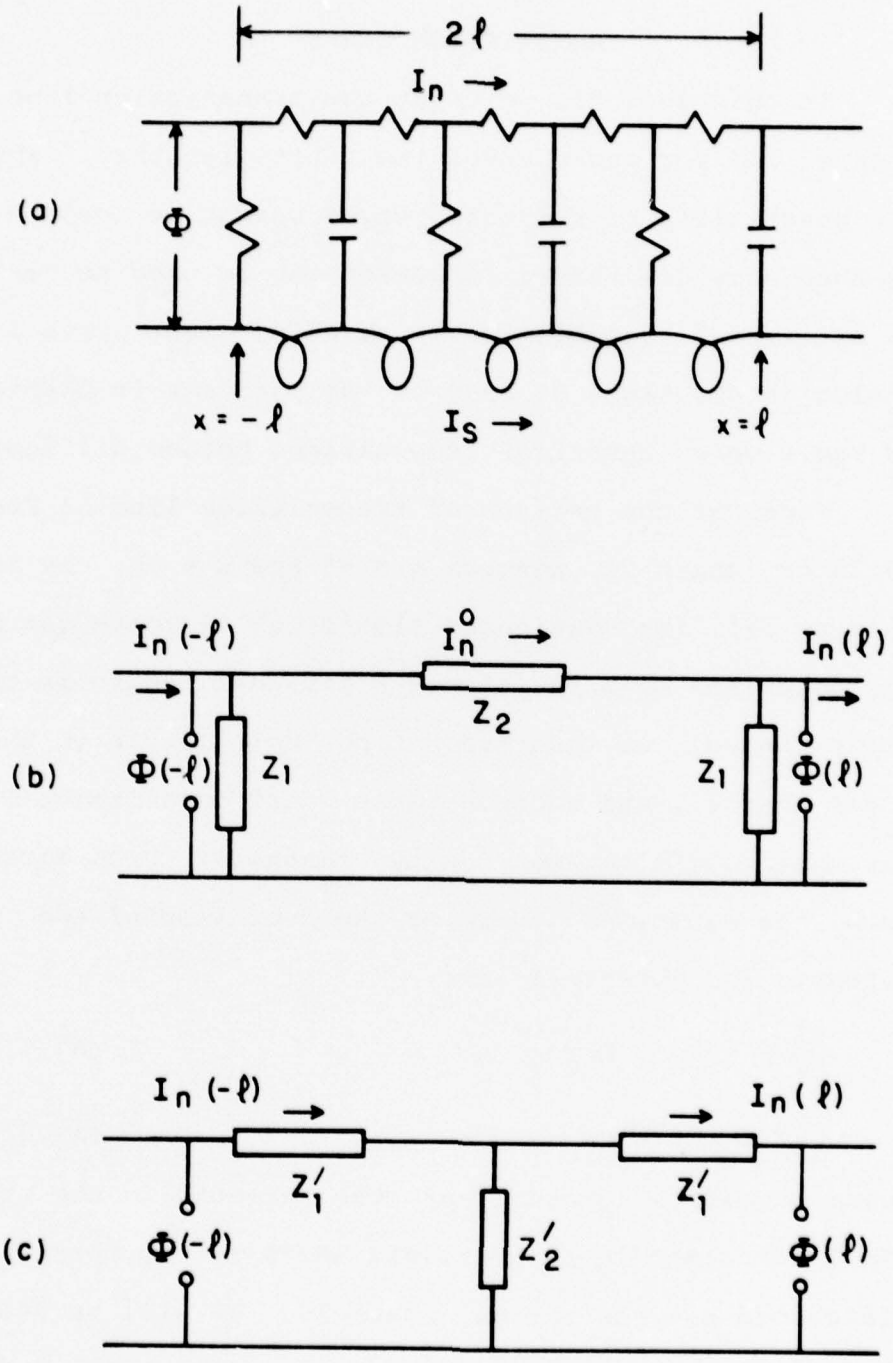

Fig. A3.1 Equivalents for finite length transmission line.
a) Schematic of transmission-line section of length 2ℓ.
b) Pi-section equivalent of (a).
c) Tee-section equivalent of (a).

so that $\dot{I}_s = -\dot{I}_n$ and Eq. (A3.1) can be rewritten

$$\frac{\partial \Phi}{\partial x} = -RI_n - L\dot{I}_n \quad . \tag{A3.3}$$

Under this condition we may also place the inductance in Fig. A3.1a in the upper channel and leave the lower channel as a "common ground"; Eqs. (A3.2) and (A3.3) are still valid. (In the more general case where $\dot{I} \neq 0$, this equivalence and the following treatment do not apply; however, a modified approach can be developed which will allow for time-varying total currents.)

From Eqs. (A3.2) and (A3.3), both Φ and I_n satisfy the equation

$$\frac{\partial^2 f}{\partial x^2} = LC\ddot{f} + (RC+GL)\dot{f} + RGf \tag{A3.4}$$

with dispersion relation

$$ik \equiv K = \sqrt{(R+i\omega L)(G+i\omega C)} \quad . \tag{A3.5}$$

Consider I_n for a particular frequency component:

$$I_n(x,t) = (Ae^{ikx} + Be^{-ikx})e^{i\omega t} \quad . \tag{A3.6}$$

Here A and B are arbitrary constants, and the first term corresponds to a wave propagating to the left, the second term to the right. Since we will be dealing only with a single frequency component, we will for simplicity suppress the time dependence:

$$I_n(x) = Ae^{ikx} + Be^{-ikx} \quad . \tag{A3.7}$$

From Eq. (A3.3) we have

$$\frac{\partial \Phi}{\partial x} = -(R+i\omega L) I_n \qquad \text{(A3.8)}$$

or

$$\Phi = -\frac{R+i\omega L}{K} (Ae^{ikx} - Be^{-ikx})$$

$$= Z_o (-Ae^{ikx} + Be^{-ikx}) \quad , \qquad \text{(A3.9)}$$

where

$$Z_o(\omega) = \sqrt{(R+i\omega L)/(G+i\omega C)} \qquad \text{(A3.10)}$$

is the characteristic impedance of the line. If there is only a wave propagating to the right then $\Phi = Z_o I_n$, while a wave propagating to the left will give $\Phi = -Z_o I_n$. When both are present the more complete relations of Eqs. (A3.7) and (A3.9) are necessary.

The transmission line section of Fig. A3.1a can be treated as a four-terminal linear passive device, or if the inductance is in the upper line, an effective three-terminal device. We can therefore look for a simple equivalent circuit with lumped impedances as in Figs. A3.1b and c, called for obvious reasons the "pi" abd "tee" equivalents. (The two impedances labeled Z_1 must be equal by symmetry, and similarly with Z_1'.) The currents and potentials at the terminals take the form

$$\begin{aligned} I_n(-\ell) &= Ae^{-ik\ell} + Be^{ik\ell} \\ I_n(\ell) &= Ae^{ik\ell} + Be^{-ik\ell} \\ \Phi(-\ell) &= Z_o(-Ae^{-ik\ell} + Be^{ik\ell}) \\ \Phi(\ell) &= Z_o(-Ae^{+ik\ell} + Be^{-ik\ell}) \end{aligned} \qquad \text{(A3.11)}$$

Considering the pi equivalent, we introduce I_n^o as the effective current passing through the impedance Z_2. By Kirchoff's laws, we have three expressions for I_n^o:

$$\begin{aligned} I_n^o &= I_n(-\ell) - \Phi(-\ell)/Z_1 \\ I_n^o &= I_n(\ell) + \Phi(\ell)/Z_1 \\ I_n^o &= [\Phi(-\ell) - \Phi(\ell)]/Z_2 \ . \end{aligned} \tag{A3.12}$$

We can solve these three equations for the three unknowns Z_1, Z_2, and I_n^o:

$$\begin{aligned} Z_1 &= Z_o \coth(K\ell) \\ Z_2 &= 2Z_o \sinh(K\ell)\cosh(K\ell) = Z_o \sinh(2K\ell) \\ I_n^o &= (A+B)/\cosh(K\ell) \end{aligned} \tag{A3.13}$$

The impedances are, as they should be, independent of the amplitudes of the waves. For the tee equivalent, a similar derivation is possible, but it is sufficient to note that the two are connected by the standard "wye-delta" (Y-Δ) transformation:

$$\begin{aligned} Z_1' &= \frac{Z_1 Z_2}{2Z_1+Z_2} = Z_o \tanh(K\ell) \\ Z_2' &= \frac{Z_1^2}{2Z_1+Z_2} = Z_o/\sinh(2K\ell) \end{aligned} \tag{A3.14}$$

In the limit where the length of the transmission line becomes long, the two ends become decoupled with input and output impedances equal to Z_o:

$$Z_1,\ Z_1' \to Z_o \ ; \quad Z_2 \to \infty \ ; \quad Z_2' \to 0 \text{ as } \ell \to \infty. \tag{A3.15}$$

(The hyperbolic functions in the impedances generally have oscillatory parts as well, but in the limit of large ℓ the leading exponential term will dominate the sinusoidal oscillations.) In the other limit of small ℓ, we have

$$\begin{aligned} Z_1 &\to \frac{Z_o}{K\ell} = [(G+i\omega C)\ell]^{-1} \\ Z_2 &\to 2Z_o K\ell = (R+i\omega L)(2\ell) \\ & \qquad\qquad , \ \ell \to 0 \qquad\qquad \text{(A3.16)} \\ Z_1' &\to Z_o K\ell = (R+i\omega L)\ell \\ Z_2' &\to \frac{Z_o}{2K\ell} = [(G+i\omega C)(2\ell)]^{-1} \end{aligned}$$

As one would expect, this reduces the section to the basic elements of the transmission line: for the small length 2ℓ, a series impedance $(R+i\omega L)2\ell$ and a shunt admittance $(G+i\omega C)2\ell$.

The transmission line can of course be constructed of these infinitesimal elements, but it can also be "constructed" of the finite length equivalents connected in series. A semi-infinite line has impedance Z_o, since there are no reflections. If we attach a pi section equivalent to this, as in Fig. A3.2a, we obtain an impedance

$$Z = Z_1 \,||\, [Z_2 + (Z_1 \,||\, Z_o)] = Z_o \qquad \text{(A3.17)}$$

as can be shown by direct calculation (the $||$ and + represent parallel and series connection respectively).

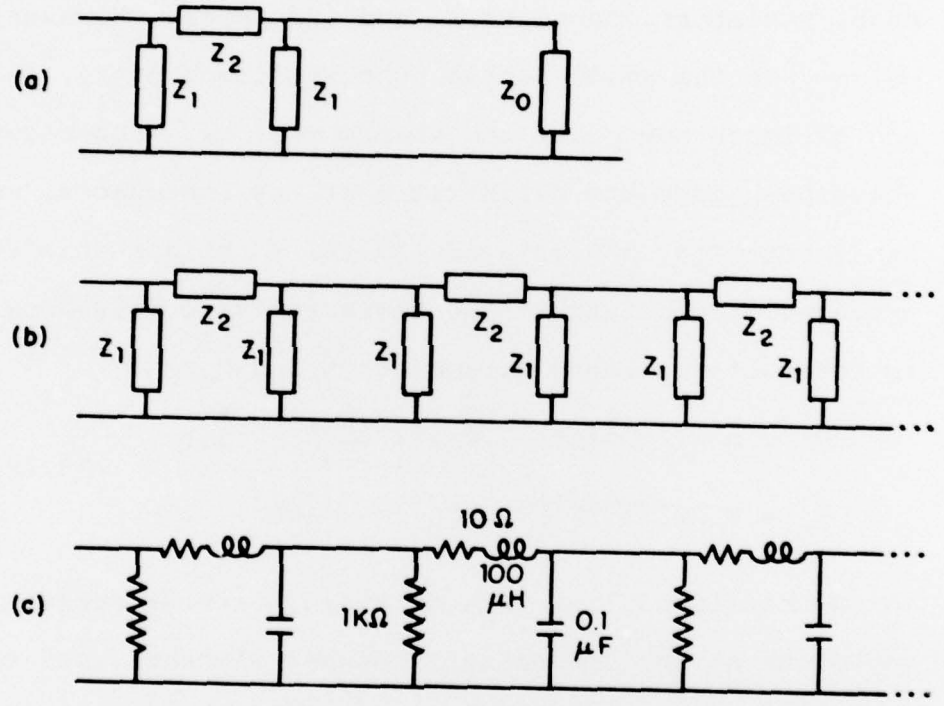

Fig. A3.2 Reconstruction of transmission line from pi-section equivalents. a) Insertion of pi-section does not alter the characteristic impedance of the line. b) Representation of the transmission line as a series of pi-section equivalents. c) An example of a reconstruction via approximate pi-section equivalents, as discussed in the text.

We can therefore attach an additional pi section, or as many as we want, and still have an impedance Z_o. An infinite series of these (Fig.A3.2b) is therefore an equivalent for the entire transmission line.

Unfortunately, for finite lengths these lumped impedances cannot easily be constructed out of the usual resistors, capacitors, and inductors. However, we can use the small length approximations of Eq. (A3.16), and estimate how great the errors will be. Substituting these back into the definitions of the impedances, we can invert Eqs. (A3.13) and (A3.14) to obtain an effective propagation constant K' and characteristic impedance Z_o' in terms of the ideal parameters K and Z_o:

$$K' = \frac{1}{\ell} \sinh^{-1}(K\ell) \approx K\left[1 + \frac{(K\ell)^2}{3} - \ldots\right]$$
$$Z_o' = Z_o/\sqrt{1 + (K\ell)^2} \approx Z_o\left[1 - \frac{(K\ell)^2}{2} + \ldots\right] \qquad \text{(A3.18)}$$

In the non-ideal line thus obtained, partial reflections may occur at the connections between elements, and this causes the deviation from ideality in the line parameters. In the limit where ℓ is much smaller than both the decay length and the wavelength, Eq. (A3.18) indicates that these deviations may be neglected.

To take a particular example, let us measure length in terms of the number of repeated units, and let each unit consist of the following elements, as shown in Fig. A3.2c:

$$R = 10\ \Omega \quad ; \quad G = 1\ m\Omega^{-1}\ (G^{-1} = 1\ k\Omega)$$
$$L = 100\ \mu H\ ;\ C = 0.1\ \mu F \tag{A3.19}$$

The characteristic times of the line are then

$$\frac{L}{R} = 10^{-5}\ \text{sec}\ ;\ \frac{C}{G} = 10^{-4}\ \text{sec}\ , \tag{A3.20}$$

and the low-frequency decay length and high-frequency velocity are

$$k_I^{-1}(0) = 1/\sqrt{RG} = 10\ \text{units}$$
$$v = 1/\sqrt{LC} = 3 \times 10^5\ \text{units/sec} \tag{A3.21}$$

From Eq. (A3.18), since we have $\ell = k_I^{-1}(0)/20$, this analog transmission line should be suitable for wavelengths down to approximately 10 units, with errors of not more than a few percent. It should be possible to construct such a line, couple it to one or more analog Josephson junctions, and use the resulting system to simulate resonance or synchronization effects in phase-slip centers (see Section 5.1).

REFERENCES

1. W.J. Skocpol, M.R. Beasley, and M. Tinkham, J. Low Temp. Phys. 16, 145 (1974).

2. T.M. Klapwijk and J.E. Mooij, Phys. Lett. 57A, 97 (1976).

3. D.W. Jillie, Ph.D. thesis, State University of New York at Stony Brook, 1976 (unpublished).

4. B.G. Boone, C.H. Arrington, L.K. Wang, and B.S. Deaver, IEEE Trans. MAG-13, 735 (1977); W.H.G. Müller and F. Baumann, Thin Solid Film 48, 193 (1978).

5. J. Meyer and G. v. Minnegerode, Phys. Lett. 38A, 529 (1972); J.D. Meyer and R. Tidecks, Sol. State Comm. 18, 305 (1976).

6. See for example A. Schmid, J. Physique 39, C6-1360 (1978); M. Tinkham, "Nonequilibrium Superconductivity", to appear in Festkörper Probleme / Advances in Solid State Physics (1979).

7. V.M. Dmitriev and E.V. Khristenko, Fiz. Nizk. Temp. 4, 821 (1978) [Sov. J. Low Temp. Phys. 4, 387 (1978)]; J.J. Chang and D.J. Scalapino, J. Low Temp. Phys. 29, 477 (1977).

8. A.G. Aronov and B.Z. Spivak, Fiz. Nizk. Temp. 4, 1365 (1978) [Sov. J. Low Temp. Phys. 4, 641 (1978)]; L.N. Smith, J. Low Temp. Phys. 28, 519 (1977).

9. M. Tinkham and J. Clarke, Phys. Rev. Lett. 28, 1366 (1972); M. Tinkham, Phys. Rev. B6, 1747 (1972).

10. J. R. Waldram, Proc. R. Soc. Lond. A345, 231 (1975).

11. W.J. Skocpol, A.M. Kadin, and M. Tinkham, J. Physique, 39, C6-1421 (1978).

12. A. Schmid and G. Schön, J. Low Temp. Phys. 20, 207 (1975).

13. J. Clarke, Phys. Rev. Lett. 28, 1363 (1972); J. Clarke and J.L. Paterson, J. Low Temp. Phys. 15, 491 (1974).

14. J. Clarke, U. Eckern, A. Schmid, G. Schön, and M. Tinkham, to appear in Phys. Rev. B., 1979.

15. A.B. Pippard, J.G. Shepherd, and D.A. Tindall, Proc. Roy. Soc. A324, 17 (1971).

16. M.L. Yu and J.E. Mercereau, Phys. Rev. B12, 4909 (1976); Phys. Rev. Lett. 28, 1117 (1972).

17. S.N. Artemenko and A.F. Volkov, Phys. Lett. 55A,113 (1976); S.N. Artemenko, A.F. Volkov, and A.V. Zaitsev, J. Low Temp. Phys. 30, 487 (1978).

18. T.Y. Hsiang and J. Clarke, Bull. Am. Phys. Soc. 24, 329 (1979); to appear in Phys. Rev. B., 1979.

19. G.J. Dolan and L.D. Jackel, Phys. Rev. Lett. 39, 1628 (1977).

20. M. Tinkham, Introduction to Superconductivity, McGraw-Hill, 1975, Section 8.2; K. Maki, "Gapless Superconductivity", Chapter 18 in Superconductivity, ed. R.D. Parks, Marcel Dekker, Inc., 1969.

21. A.M. Kadin, W.J. Skocpol, and M. Tinkham, J. Low Temp. Phys. 33, 481 (1978).

22. A. Schmid and G. Schön, Phys. Rev. Lett. 34, 941 (1975); S.N. Artemenko and A.F. Volkov, Zh. Eksp. Teor. Fiz. 69, 1764 (1975) [Sov. Phys. JETP 42, 896 (1976)]; O. Entin-Wohlman and R. Orbach, Ann. Phys. (N.Y.) 116, 35 (1978).

23. R.V. Carlson and A.M. Goldman, Phys. Rev. Lett. 34, 11 (1975); J. Low Temp. Phys. 25, 67 (1976).

24. C.J. Pethick and H. Smith, Ann. Phys. (N.Y.) 119, 133 (1979).

25. A.M. Kadin, L.N. Smith, and W.J. Skocpol, submitted to J. Low Temp. Phys. (1979).

26. W.J. Skocpol, Ph.D. Thesis, Harvard University (1974); available as Technical Report #8, Division of Engineering and Applied Physics, Harvard Univ. (1974).

27. M. Octavio, Ph.D. Thesis, Harvard University (1977); available as Technical Report #13, Division of Applied Sciences, Harvard University (1978).

28. B. Abeles, R.W. Cohen, and G.W. Cullen, Phys. Rev. Lett. 17, 632 (1966); R.P. Pettit and J. Silcox, Phys. Rev. B13, 2865 (1976).

29. M. Tinkham, Introduction to Superconductivity, McGraw-Hill, 1975, p. 113.

30. R.P. Huebener and H.L. Watson, Phys. Rev. B9, 3725 (1974); D.E. Chimenti, H.L. Watson, and R.P. Huebener, J. Low Temp. Phys. 23, 303 (1976); M.C.L. Orlowski, W. Buck, and R.P. Huebener, J. Low Temp. Phys. 27, 159 (1977).

31. K.K. Likharev, Rev. Mod. Phys. 51, 101 (1979), Chapter III.

32. M. Tinkham, Introduction to Superconductivity, McGraw-Hill, 1975, p. 80.

33. M. Tinkham, Introduction to Superconductivity, McGraw-Hill, 1975, Section 4-6.

34. J.M. Blakely and H. Mykura, Acta Met. 9, 23 (1961); R.T. King and W.W. Mullins, Acta Met. 10, 601 (1962).

35. M. Tinkham, Introduction to Superconductivity, McGraw-Hill, 1975, Section 4-10.1.

36. J. Clarke and J.L. Paterson, J. Low Temp. Phys. 15, 491 (1974).

37. S.N. Artemenko, A.F. Volkov, and A.V. Zaitsev, J. Low Temp. Phys. 30, 487 (1978).

38. A.L. Shelankov, Fiz. Tverd. Tela 19, 3256 (1977) [Sov. Phys. Solid State 19, 1903 (1977)].

39. O. Entin-Wohlman and R. Orbach, Phys. Rev. B19, 4510 (1979).

40. S.B. Kaplan, C.C. Chi, D.N. Langenberg, J.J. Chang, S. Jafarey, and D.J. Scalapino, Phys. Rev. B14, 4854 (1976).

41. C.C. Chi and John Clarke, Phys. Rev. B19, 4495 (1979).

42. John Clarke and Albert Schmid, private communication, (1978).

43. M. Tinkham, Introduction to Superconductivity, McGraw-Hill, 1975, Section 2-9.

44. A. Schmid, private communication (1976); G. Schön, private communication (1978).

45. T.R. Lemberger and J. Clarke, Bull. Am. Phys. Soc. 24, 328 (1979); T.R. Lemberger, private communication (1979).

46. W.J. Skocpol, M.R. Beasley, and M. Tinkham, J. Appl. Phys. 45, 4054 (1974).

47. V.G. Volotskaya, L.E. Musienko, I.M. Dmitrenko, and Yu.V. Kalekin, Fiz. Nizk. Temp. 2, 500 (1976) [Sov. J. Low Temp. Phys. 2, 248 (1976)]; V.A. Shklovskii, Fiz. Tverd. Tela 17, 3076 (1975) [Sov. Phys. Solid State 17, 2040 (1975)]; V.A. Kashchei, Fiz. Tverd. Tela 19, 1600 (1977) [Sov. Phys. Solid State 19, 934 (1977)].

48. G. Rickayzen, "The Theory of Bardeen, Cooper, and Schrieffer," Chapter 2 in Superconductivity, ed. R. Parks, Marcel Dekker, Inc., 1969, p. 105.

49. A. Rothwarf and B.N. Taylor, Phys. Rev. Lett. 19, 27 (1967); L.N. Smith and J.M. Mochel, Phys. Rev. Lett. 35, 1597 (1975).

50. L.D. Jackel, W.H. Henkels, J.M. Warlamont, and R.A. Buhrman, Appl. Phys. Lett. 29, 214 (1976).

51. A.M. Kadin and W.J. Skocpol, unpublished data.

52. M. Tinkham, Introduction to Superconductivity, McGraw-Hill, 1975, Section 4-4.

53. J.D. Meyer and R. Tidecks, Sol. State Comm. 24, 643 (1977).

54. M. Tinkham, J. Low Temp. Phys. 35, 147 (1979).

55. A.G. Aronov and V.L. Gurevich, Fiz. Tverd. Tela 16, 2656 (1974) [Sov. Phys. Solid State 16, 1722 (1975)].

56. V.P. Galaiko, Zh. Eksp. Teor. Fiz. 68, 223 (1975) [Sov. Phys. JETP 41, 108 (1975)].

57. S.N. Artemenko, A.F. Volkov, and A.V. Zaitsev, ZhETF Pis. Red. 27, 122 (1978) [JETP Lett. 27, 113 (1978)].

58. O.D. Cheishvili, Fiz. Nizk. Temp. 3, 736 (1977) [Sov. J. Low Temp. Phys. 3, 357 (1977)].

59. W. Thomson (Lord Kelvin), Proc. Roy. Soc., May 1855.

60. V.P. Galaiko, J. Low Temp. Phys. 26, 483 (1977).

61. L. Kramer and A. Baratoff, Phys. Rev. Lett. 38, 518 (1977); L. Kramer and R.J. Watts-Tobin, Phys. Rev. Lett. 40, 1041 (1978).

62. K.H. Gundlach and J. Kadlec, J. Low Temp. Phys. 26, 603 (1977).

63. J. Bok and C. Guthmann, J. Physique Lett. 39, L-187 (1978); S.K. Decker and D.W. Palmer, J. Appl. Phys. 48, 2043 (1977).

64. R. Tidecks and J.D. Meyer, Z. Physik B32, 363 (1979).

65. D.W. Jillie, J.E. Lukens, and Y.H. Kao, IEEE Trans. Mag-13, 578 (1977); Phys. Rev. Lett. 38, 915 (1977).

66. D.W. Palmer and J.E. Mercereau, Phys. Lett. 61A, 135 (1977).

67. P.E. Lindelof and J. Bindslev Hansen, J. Low Temp. Phys. 29, 369 (1977).

68. J.A. Mydosh and H. Meissner, Phys. Rev. 140, A 1568 (1965).

69. M. Tinkham, private communication (1979).

70. N.Ya. Fogel', A.A. Moshenskii, A.M. Glukhov, and I.M. Dmitrenko, Pis'ma Zh. Eksp. Teor. Fiz. 22, 450 (1975) [JETP Lett. 22, 217 (1975)].

71. M. Octavio, W.J. Skocpol, and M. Tinkham, Phys. Rev. B17, 159 (1978).

72. See e.g. W.J. Skocpol, in AIP Conf. Proc. No. 44, Future Trends in Superconductive Electronics, 1978, p. 335; also ref. 27.

73. A.H. Silver and J.E. Zimmerman, in Applied Superconductivity, ed. V.L. Newhouse, Academic Press, 1975, p. 19.

74. See e.g. E. Mallet, Telegraphy and Telephony, Chapman and Hall Ltd., 1929, p. 185; W.C. Johnson, Transmission Lines and Networks, McGraw-Hill, 1950, p. 119.

ACKNOWLEDGEMENTS

I would like to thank Prof M. Tinkham for providing guidance and a wealth of valuable suggestions during the course of this work, and Prof. W.J. Skocpol for getting me started on the project and providing close and continuing support throughout the research. I would also like to thank the other members of the Harvard superconductivity group, past and present, who have helped me through the inevitable problems associated with the work. In particular, the many long discussions with Dr. L.N. Smith have been indispensible in the development of various aspects of this work. Financial support was provided in part through the auspices of the National Science Foundation and the Office of Naval Research.

DISTRIBUTION LIST FOR ONR ELECTRONIC AND SOLID STATE SCIENCES

Director
Advanced Research Projects Agency
Attn: Technical Library
1400 Wilson Boulevard
Arlington, Virginia 22209

Office of Naval Research
Electronics Program Office (Code 427)
800 North Quincy Street
Arlington, Virginia 22217

Office of Naval Research
Code 105
800 North Quincy Street
Arlington, Virginia 22217

Director
Naval Research Laboratory
4555 Overlook Avenue, S.W.
Washington, D.C. 20375
Attn: Technical Library (6 cys)
Code 5200 (1 copy)
5210 (1 copy)
5270 (1 copy)
6400 (1 copy)

Office of the Director of Defense
Research and Engineering
Office of the Assistant Director
Electronics & Physical Sciences
The Pentagon, Room 3D1079
Washington, DC 20301

Defense Documentation Center (12 cys)
Cameron Station
Alexandria, Virginia 22314

Commanding Officer
Office of Naval Research Branch Office
536 South Clark Street
Chicago, Illinois 60605

San Francisco Area Office
Office of Naval Research
50 Fell Street
San Francisco, California 94102

Commanding Officer
Office of Naval Research Branch Office
1030 East Green Street
Pasadena, California 91101

Commanding Officer
Office of Naval Research Branch Office
495 Summer Street
Boston, Massachusetts 02210

New York Area Office
Office of Naval Research
115 Broadway 5th Floor
New York, New York 10003

ODDR&E Advisory Group on Electron Devices
201 Varick Street
New York, New York 10014

Naval Air Development Center
Attn: Technical Library
Johnsville
Warminster, Pennsylvania 18974

Naval Weapons Center
China Lake, California 93555
Attn: Technical Library (1 copy)
Code 6010 (1 copy)

Naval Research Laboratory
Underwater Sound Reference Division
Technical Library
P.O. Box 8337
Orlando, Florida 32806

Navy Underwater Sound Laboratory
Technical Library
Fort Trumbull
New London, Connecticut 06320

Commandant, Marine Corps
Scientific Advisor (Code AX)
Washington, D.C. 20380

Naval Ordnance Station
Technical Library
Indian Head, Maryland 20640

Naval Postgraduate School
Monterey, California 93940
Attn: Technical Library (1 copy)
Elect. Engin. Depart. (1 copy)

Naval Missile Center
Technical Library (Code 5632.2)
Point Mugu, California 93010

Naval Electronics Laboratory Center
San Diego, California
Attn: Technical Library (1 copy)
Code 2300 (1 copy)
2600 (1 copy)
4800 (1 copy)

Naval Undersea Center
Technical Library
San Diego, California 92132

Naval Weapons Laboratory
Technical Library
Dahlgren, Virginia 22448

Naval Ship Research and Development Center
Central Library (Codes L42 and L43)
Washington, D.C. 20007

Naval Surface Weapons Center
White Oak Laboratory
Silver Spring, Maryland 20910
Attn: Technical Library (1 copy)
Code 200 (1 copy)
212 (1 copy)

Deputy Chief of Naval Operations
(Development)
Technical Analysis and Advisory Group
(Code NOP-077D)
Washington, D.C. 20350

Commander
Naval Air Systems Command
Washington, D.C.
ATTN: Code 310 (1 copy)
360 (1 copy)

Commander
Naval Electronics Systems Command
Washington, D.C. 20360
Attn: Code 304 (1 copy)
310 (1 copy)

Commander
Naval Sea Systems Command
Washington, D.C. 20360

Naval Surface Weapons Center
Attn: Library
Dahlgren, Virginia 22448

Air Force Office of Scientific Research
Attn: Electronic and Solid State
Sciences Division
Department of the Air Force
Washington, D.C. 20333

Air Force Weapon Laboratory
Technical Library
Kirtland Air Force Base
Albuquerque, New Mexico 87117

Air Force Avionics Laboratory
Air Force Systems Command
Technical Library
Wright-Patterson Air Force Base
Dayton, Ohio 45433

Air Force Cambridge Research Laboratory
L.G. Hanscom Field
Technical Library
Cambridge, Massachusetts 02138

Harry Diamond Laboratories
Technical Library
Connecticut Avenue at Van Ness, N.W.
Washington, D.C. 20438

U.S. Army Research Office
Box CM, Duke Station
Durham, North Carolina 27706

Director
U.S. Army Engineering Research
and Development Laboratories
Fort Belvoir, Virginia 22060
Attn: Technical Documents Center

Director National Bureau of Standards
Attn: Technical Library
Washington, D.C. 20234

Naval Research Laboratory
4555 Overlook Avenue, S.W.
Washington, D.C. 20375
Attn: Code 5300 (1 copy)
7100 (1 copy)
7900 (1 copy)

Naval Electronics Laboratory Center
San Diego, California 92152
Attn: Code 2100 (1 copy)
2200 (1 copy)

C.C. Klick
Superintendent
Materials Sciences Division
Naval Research Laboratory
4555 Overlook Avenue, S.W.
Washington, D.C. 20375

Naval Research Laboratory
4555 Oberlook Avenue, S.W.
Washington, D.C. 20375
Attn: Code 5220 (1 copy)
5230 (1 copy)
5250 (1 copy)
5260 (1 copy)
5270 (1 copy)
5500 (1 copy)

Naval Electronics Laboratory Center
San Diego, California 92152
Attn: Code 2500 (1 copy)
4000 (1 copy)

Office of Naval Research (2 cys)
800 N. Quincy Street
Arlington, Virginia 22217
Attn: Code 430 (2 copies)

Naval Research Laboratory
4555 Overlook Avenue, S.W.
Washington, D.C. 20375
Attn: Code 5400

Naval Electronics Laboratory Center
San Diego, California 92152
Attn: Code 3000 (1 copy)
5000 (1 copy)
5600 (1 copy)

Air Force Office of Scientific Research
Mathematical and Information Sciences
Directorate
1400 Wilson Blvd.
Washington, D.C. 20333

ARMY MISSILE DISTRIBUTION LIST

Director
National Security Agency
ATTN: Dr. T. J. Smith
Fort George G. Meade, MD 20755

Defense Documentation Center
ATTN: DDC-DDA (Mrs. V. Caponio)
Cameron Station
Alexandria, VA 22314

Asst. Sec
Office of Director of Defense
Research and Engineering
The Pentagon
Washington, DC 20315

Defense Advanced Research
Projects Agency
ATTN: (Dr. S. Reynolds)
1400 Wilson Boulevard
Arlington, VA 22209

Commander
HQ Army Air Defense School
ATTN: ATSAD-P-CSD
Fort Bliss, TX 79916

Commander
US Army Armament R&D Command
ATTN: DRDAR-SD
Dover, NJ 07801

Commander
US Army Ballistic Research Lab.
ATTN: DRDAR-BAD
Aberdeen Proving Ground
Aberdeen, MD 21005

Commander
US Army Combat and General
Staff College
ATTN: Acquisitions, Lib. Div.
Fort Leavenworth, KS 66027

Commander
US Army Communication Command
ATTN: CC-OPS-PE
Fort Huachuca, AZ 85613

Commander
US Army Materials and Mechanics
Research Center
ATTN: Chief, Materials Sciences
Division
Watertown, MA 02172

Commander
US Army Material Development
and Readiness Command
ATTN: Technical Library, Rm.7S 35
5001 Eisenhower Avenue
Alexandria, VA 22333

Commander
US Army Missile R&D Command
ATTN: Chief, Document Section
Redstone Arsenal, AL 35809

Commander
US Army Satellite Communications
Agency
Fort Monmouth, NJ 07703

Commander
US Army Security Agency
ATTN: IAMD-T
Arlington Hall Station
Arlington, VA 22212

Project Manager
ARTADS
EAT Building
West Long Branch, NJ 07764

Commander/Director
Atmospheric Sciences Lab. (ECOM)
ATTN: DRSEL-SL-DD
White Sands Missile Range, NM 88002

Commander
US Army Electronics Command
ATTN: DRSEL-SL-O (Dr. E.E. Bennett)
Fort Monmouth, NJ 07703

Director
USA-TRC
ATTN: TT-AD (Mrs. Driller)
Fort Monmouth, NJ 07703

Commander
US Army Electronics Command
ATTN: DRSEL-CT-L (Dr. E. Bauer)
Fort Monmouth, NJ 07703

Director
Electronic Warfare Lab. (ECOM)
ATTN: DRSEL-EL-DT
White Sands Missile Range, NM 88002

Executive Secretary, TSC/JSEP
US Army Research Office
P.O. Box 12211
Research Triangle Park, NC 27709

Commander
Frankford Arsenal
Deputy Director,
Fire-Control Laboratory
Philadelphia, PA 19137

Project Manager
Ballistic Missile Defense Program Office
ATTN: DACS-BMP (Mr. J. Allen)
1300 Wilson Blvd.
Arlington, VA 22209

Commander
Harry Diamond Laboratories
ATTN: MD, John E. Rosenberg
2800 Powder Mill Road
Adelphi, MD 20783

NSWC (Code-WR2-A)
Washington, DC 20350

Commander
US Army Electronics Command
Fort Monmouth, NJ 07703
ATTN: DRSEL-TL-E (Dr. J.A. Asbo)
DRSEL-TL-ID (Dr. S. Shoemaker)
DRSEL-SL-T (Dr. A. Bailey)
DRSEL-SL-E (Dr. E. Liebler)
DRSEL-TL-MM (Dr. H. Ligetz)
DRSEL-SS-C (Dr. W.S. Bodtke)
DRSEL-SL-S (Dr. D.C. Pennell
DRSEL-SL-SD-1 (Dr. F. Schwering)
DRSEL-TL-I (Dr. C.E. Thornton)

COL Robert Shaw
Senior Planning&Radiation Representative
US Army Standardization Group, Canada
Canadian Force Headquarters
Ottawa, Ontario, Canada K1A 0K2

Director
Night Vision Laboratory
ATTN: DRSEL-NV-D
Fort Belvoir, VA 22060

Commander
Picatinny Arsenal
ATTN: SMUPA-TS-T-S
Dover, NJ 07801

Dr. Sidney Ross
Technical Director
SARFA-TD
Frankford Arsenal
Philadelphia, PA 19137

US Army Research Office (Repo)
ATTN: Library
P.O. Box 12211
Research Triangle Park, NC 27709

Director
Division of Neuropsychiatry
Walter Reed Army Institute of
Research
Washington, DC 20012

Commander
White Sands Missile Range
ATTN: STEWS-ID-R
White Sands Missile Range, NM 88002

Mr. Robert Barrett
RADC/EPP
Hanscom AFB, MA 01731

Dr. Carl E. Baum
AFWL (ES)
Kirtland AFB, NM 87117

Dr. E. Champagne
AFAL/DH
Wright-Patterson AFB, OH 45433

Dr. R. P. Dolan
RADC/EPP
Hanscom AFB, MA 01731

Mr. W. Edwards
AFAL/TB
Wright-Patterson AFB, OH 45433

Professor R.E. Fontana
Head, Dept. of Electrical Eng.
AFIT/ENE
Wright-Patterson AFB, OH 45433

Dr. Alan Garscadden
AFAPL/POD
Wright-Patterson AFB, OH 45433

USAF European Office of Aerospace
Research
ATTN: Major J. Gorrell
Box 14, FPO, New York 09510

LTC Richard J. Gowen
Dept. of Electrical Engineering
USAF Academy, CO 80840

Mr. Harvey Hasselman (SOCA)
Hans Air Development Center
Griffiss AFB, NY 13441

Dr. G. Kneezenberg
Air Force Member, TAC
Air Force Office of Scientific
Research
(AFSC) AFSC/NE
Bolling Air Force Base, DC 20332

Dr. L. Krevitz
Air Force Member, TAC
Air Force Office of Scientific
Research
(AFSC) AFSC/NE
Bolling Air Force Base, DC 20332

Dr. R. D. Larson
AFAL/DHR
Wright-Patterson AFB, OH 45433

Dr. Richard D. Mack
RADC/EPSR
Hanscom AFB, MA 01731

Mr. John Mottmuth (ECTT)
HQ USAF (AFSC)
Hanscom AFB, MA 01731

Dr. Richard Picard
RADC/EPSR
Hanscom AFB, MA 01731

Dr. J. Rylee
Chief Scientist
AFAL/CA
Wright-Patterson AFB, OH 45433

Dr. Allen Schell
RADC/EPSR
Hanscom AFB, MA 01731

Mr. R.E. Webb, Jr. (ECP)
Rome Air Development Center
Griffiss AFB, NY 13441

LTC G. Ingalls
Air Force Office of Scientific
Research
(AFSC) AFOSR/NP
Bolling Air Force Base, DC 20332

LTC G. McKenzie
Air Force Office of Scientific
Research
(AFSC) AFOSR/NA
Bolling Air Force Base, DC 20332

Mr. R. E. Aligeier
Naval Surface Weapons Center
Code WR-303
White Oak
Silver Spring, MD 20910

Naval Weapons Center
ATTN: Code 5515 - R.F. Bissah
China Lake, CA 93555

Dr. R. L. Bland
Technical Director
Naval Undersea Center
San Diego, CA 92152

Naval Research Laboratory
4555 Overlook Avenue, SW
Washington, DC 20375
ATTN: Code 5300 - A. Brodzinsky
Code 7701 - J. D. Brown
Code 5210 - J. E. Dorsey
Code 5400/5410 - J.R. Davis
Code 5510 - R. L. Faust
Code 2627 - Mrs. D. Folen

Naval Ocean Systems Center
ATTN: Code 75 - W.J. Dejka
271 Catalina Boulevard
San Diego, CA 92152

Naval Weapons Center
ATTN: Code 601 - F.C. Essig
China Lake, CA 93555

Dr. Robert R. Fossum
Dean of Research
Naval Postgraduate School
Monterey, CA 93940

Dr. G. G. Gould
Technical Director
Naval Coastal Systems Lab.
Panama City, FL 32401

Naval Ocean Systems Center
ATTN: Code 7303 - V.E. Hildebrand
271 Catalina Boulevard
San Diego, CA 92152

Naval Ocean Systems Center
ATTN: Code 753 - P.H. Johnson
217 Catalina Boulevard
San Diego, CA 92152

Donald E. Kirk
Professor and Chairman
Electronic Engineer, EP-304
Naval Postgraduate School
Monterey, CA 93940

Naval Air Development Center
ATTN: Code 01 - Dr. B. E. Lobb
Johnsville
Warminster, PA 18974

Naval Research Laboratory
ATTN: Code 5370 - B.D. McCombe
4555 Overlook Avenue, SW
Washington, DC 20375

Capt. R.B. Mooney
Naval Sea Systems Command
SC 01
2531 Jefferson Davis Hwy
Arlington, VA 20362

Dr. R. J. Moeller
Naval Air Systems Command
Code 310
JP #1
1411 Jefferson Davis Hwy
Arlington, VA 20360

Dr. J.D. Mills, Jr.
Naval Surface Weapons Center
Electronics Systems Department
Code DF
Dahlgren, VA 22448

Naval Ocean Systems Center
ATTN: Code 702 - R.T. Morisaki
271 Catalina Boulevard
San Diego, CA 92152

Naval Air Development Center
ATTN: Technical Library
Johnsville
Warminster, PA 18974

Naval Ocean Systems Center
ATTN: Technical Library
271 Catalina Boulevard
San Diego, CA 92152

Naval Research Laboratory
Underwater Sound Reference Division
Technical Library
P.O. Box 8337
Orlando, FL 32806

Naval Surface Weapons Center
ATTN: Technical Library
Code DX-21
Dahlgren, VA 22448

Naval Surface Weapons Center
ATTN: Technical Library
Building 1-330, Code WX-40
White Oak
Silver Spring, MD 20910

Naval Training Equipment Center
ATTN: Technical Library
Orlando, FL 32813

Naval Undersea Center
ATTN: Technical Library
San Diego, CA 92132

Naval Underwater Systems Center
ATTN: Technical Library
Newport, RI 02840

Office of Naval Research
Electronic & Solid State Sciences
Program (Code 427)
800 North Quincy Street
Arlington, VA 2217

Office of Naval Research
Mathematics Program (Code 432)
800 North Quincy Street
Arlington, VA 22217

Office of Naval Research
Naval Systems Division
Code 230/221
800 North Quincy Street
Arlington, VA 22217

Director
Office of Naval Research
New York Area Office
715 Broadway, 5th Floor
New York, NY 10003

Office of Naval Research
San Francisco Area Office
One Hallidie Plaza - Suite 601
San Francisco, CA 94102

Director
Office of Naval Research Branch
Office
495 Summer Street
Boston, MA 02210

Director
Office of Naval Research Branch
Office
536 South Clark Street
Chicago, IL 60605

Director
Office of Naval Research Branch
Office
1030 East Green Street
Pasadena, CA 91101

Mr. H. E. Riedl
Naval Surface Weapons Center
Code WR-34
White Oak Laboratory
Silver Spring, MD 20910

Naval Air Development Center
ATTN: Code 202 - T. J. Shapple
Johnsville
Warminster, PA 18974

Naval Research Laboratory
ATTN: Code 5403-J. E. Shore
4555 Overlook Avenue, SW
Washington, DC 20375

A. L. Slafkosky
Scientific Advisor
Headquarters Marine Corps
HC-RD-1
Arlington Annex
Washington, DC 20380

Harris R. Stone
Office of Research, Development,
Test and Evaluation
OSD-097
The Pentagon, Room 3D760
Washington, DC 20350

Mr. L. Ramsey
Naval Electronics Systems Command
Code 3042, HC #1
2511 Jefferson Davis Hwy.
Arlington, VA 20360

David W. Taylor
Naval Ship Research and
Development Center
Code 521.1
Bethesda, MD 20084

Naval Research Laboratory
ATTN: Code 6109-Dr. R. Tuttle
4555 Overlook Avenue, SW
Washington, DC 20375

Lt.Cdr. John Turner
USNAVY 0343
CP #5, Room 1044
2211 Jefferson Davis Hwy.
Arlington, VA 20360

Naval Ocean Systems Center
ATTN: Code 706-H.D. Vieder
271 Catalina Boulevard
San Diego, CA 92152

Dr. W. A. Von Winkle
Associate Technical Director
for Technology
Naval Underwater Systems Center
New London, CT 06320

Dr. Gernot M. R. Winkler
Director, Time Service
US Naval Observatory
Massachusetts Avenue at
34th Street, NW
Washington, DC 20390

Dr. Edward W. Ziegl
Deputy Director
Division of Materials Research
National Science Foundation
1800 G Street
Washington, DC 20550

Mr. J. C. French
National Bureau of Standards
Electronics Technology Division
Washington, DC 20234

Dr. Jay Harris
Program Director
Devices and Waves Program
National Science Foundation
1800 G Street
Washington, DC 20550

Los Alamos Scientific Laboratory
ATTN: Reports Library
P.O. Box 1663
Los Alamos, NM 87544

Dr. Edna Mitchell
Program Director
Solid-State Physics
Division of Materials Research
National Science Foundation
1800 G Street
Washington, DC 20550

Mr. F. C. Schwenk, RD-T
National Aeronautics and Space
Administration
Washington, DC 20546

H. Rene Shaisten
Deputy Director Institute for
Computer Sciences and Technology
National Bureau of Standards
Washington, DC 20234

Director
Columbia Radiation Laboratory
Columbia University
538 West 120th Street
New York, NY 10027

Director
Coordinated Science Laboratory
University of Illinois
Urbana, IL 61801

Director of Laboratories
Division of Applied Sciences
Harvard University
Pierce Hall
Cambridge, MA 02138

Director
Electronics Research Center
The University of Texas
Engineering-Science Bldg. 112
Austin, TX 78712

Director
Electronics Research Laboratory
University of California
Berkeley, CA 94720

Director
Electronics Sciences Laboratory
University of Southern California
Los Angeles, CA 90007

Director
Microwave Research Institute
Polytechnic Institute of New York
333 Jay Street
Brooklyn, NY 11201

Director
Research Laboratory of Electronics
Massachusetts Institute of
Technology
Cambridge, MA 02139

Director
Stanford Electronics Laboratory
Stanford University
Stanford, CA 94305

Stanford Ginzton Laboratory
Stanford University
Stanford, CA 94305

Officer in Charge
Carderock Laboratory
Code 18-C.H. Dietsche
David Taylor Naval Ship Research
and Development Center
Bethesda, MD 20084

Dr. Ray F. Potter
3664 Talbot Street
San Diego, CA 92106